

Exploring Novel Modalities for Optical Diffraction Tomography

Présentée le 21 septembre 2023

Faculté des sciences et techniques de l'ingénieur
Laboratoire d'optique
Programme doctoral en photonique

pour l'obtention du grade de Docteur ès Sciences

par

Amirhossein SABA SHIRVAN

Acceptée sur proposition du jury

Prof. M. Unser, président du jury
Prof. D. Psaltis, directeur de thèse
Dr P. Ferraro, rapporteur
Dr A. Goy, rapporteur
Prof. C. Moser, rapporteur

To my family...

Acknowledgements

I would like to take this opportunity to extend my gratitude to all my colleagues and friends who contributed to the completion of my Ph.D. thesis.

First and foremost, thanks to Professor Demetri Psaltis. I am very grateful for having had him as my thesis director. It was a great opportunity to be a member of the Optics Laboratory, discuss with him, and learn from him. I would like to thank him for his support and advice throughout my research at EPFL. Demetri has contributed significantly in making my scientific character during my doctoral studies and I appreciate it cordially.

I would like to thank the present and past members of the Optics Laboratory. Special thanks to Joowon, and Carlo who helped me with several projects for my Ph.D. I want to especially thank Giulia, Eirini, Evi, and Pooria whose friendship helped me to have a better Ph.D. journey in the Optics Laboratory. I should also thank other colleagues in the lab: Ahmed, Elizabeth, Ye, Mohammad, Ilker, Ulas, Navid, Leo, Marilisa, Steven, Kyriakos, and Abhijit.

Also, having many friends in Lausanne made my life much more interesting during the last four years. I should thank them all for their friendship and support: Babak Rahmani, Alireza Mohammadshahi, Farnaz Eslami, Aida Mousavifar, Reza Banaei, Farzad Pourkamali, Reza Ebrahimi, Yasmin Ghadyani, Hossein Tabatabaei, Raman Gaderi, Salar Rahimi, Shayan Khalooei, Ali Momeni, Fatemeh Moradi and many others who made Ph.D. life more pleasant.

Last but not least, I would like to thank my family: my sisters Anna and Aylar, and endless love to my mother and father who whatever I have in my life is because of them. Mamnoon.

Lausanne, April 2023

Amirhossein Saba

Abstract

In the past decade, optical diffraction tomography has gained a lot of attention for its ability to create label-free three-dimensional (3D) images of the refractive index distribution of biological samples using scattered fields measured through holography from multiple angles. Although many experimental and computational methods have been conducted to produce decent 3D refractive index tomograms, some theoretical aspects of this technique have not been studied thoroughly, limiting its use to imaging the linear refractive index of a single or a few isotropic cells in the homogeneous background.

In the techniques proposed so far, the intensity and phase of the scattered field are exploited to reconstruct a 3D sample. However, polarization, as an important feature of light, is not discussed in optical diffraction tomography in order to image anisotropic samples. Nevertheless, many biological samples, especially those with fibrous structures, such as skin or muscle tissues have intrinsic or form birefringence. As a result, polarization-sensitive optical diffraction tomography can provide a 3D reconstruction of novel modalities showing interesting features in the sample which can not be observed in the scalar refractive index distribution.

Similarly, samples containing nonlinear optical susceptibility can generate light in other frequencies such as harmonic generation. The nonlinear optical susceptibility can reveal features that are not observable in the linear refractive index distribution. For biological examples, fibrous proteins such as myosin or collagen possess second-order nonlinear optical susceptibility and can show second-harmonic or sum frequency generation. However, the generalization of the optical diffraction tomography approaches to nonlinear processes is not studied yet. A similar approach to optical diffraction tomography can be presented by inversion of the nonlinear wave equations governing the frequency mixing processes and reconstructing the 3D distribution of the nonlinear susceptibility using 2D complex images of the generated frequencies.

In this thesis, I generalize conventional optical diffraction tomography to polarization-sensitive and nonlinear media. The proposed methods in this thesis provide novel modalities for optical diffraction tomography which can be used for 3D imaging of anisotropic and nonlinear samples. I present numerical and experimental results for various examples to investigate the viability of the proposed modalities. Another aspect of this thesis is to present an iterative solution for optical diffraction tomography based on a forward model which is as accurate

as full-wave electromagnetics simulation and can include different scenarios, such as depolarization, anisotropy, and nonlinearity. As full-wave solutions cannot be easily used in the gradient-based iterative optimization approaches for optical diffraction tomography, a physics-informed neural network is presented and used as the forward model in an iterative reconstruction of optical diffraction tomography.

The methods that are studied in this thesis have a significant impact on optical diffraction tomography and 3D imaging. Through an in-depth theoretical, numerical, and experimental analysis, this research aims to investigate the possibilities of utilizing these techniques in the development of label-free 3D imaging modalities.

Keywords: optical diffraction tomography, three-dimensional imaging, optical scattering, inverse scattering, polarization-sensitive imaging, nonlinear imaging, iterative reconstruction, physics-informed deep learning.

Résumé

Au cours de la dernière décennie, la tomographie par diffraction optique a attiré beaucoup d'attention pour sa capacité à créer des images tridimensionnelles (3D) sans marquage de la distribution de l'indice de réfraction d'échantillons biologiques à l'aide de champs dispersés mesurés par holographie sous plusieurs angles. Bien que de nombreuses méthodes expérimentales et informatiques aient été menées pour produire des tomogrammes d'indice de réfraction 3D décents, certains aspects théoriques de cette technique n'ont pas été étudiés à fond, limitant son utilisation à l'imagerie de l'indice de réfraction linéaire d'une seule ou de quelques cellules isotropes dans l'espace libre.

Dans les techniques proposées jusqu'à présent, l'intensité et la phase du champ diffusé sont exploitées pour reconstruire un échantillon 3D. Cependant, la polarisation, en tant que caractéristique importante de la lumière, n'est pas discutée dans la tomographie par diffraction optique afin d'imager des échantillons anisotropes. Néanmoins, de nombreux échantillons biologiques, en particulier ceux avec des structures fibreuses, telles que la peau ou les tissus musculaires, ont une biréfringence intrinsèque ou de forme. En conséquence, la tomographie par diffraction optique sensible à la polarisation peut fournir une reconstruction 3D de nouvelles modalités montrant des caractéristiques intéressantes dans l'échantillon qui ne peuvent pas être observées dans la distribution scalaire de l'indice de réfraction.

De même, les échantillons contenant une susceptibilité optique non linéaire peuvent générer de la lumière dans d'autres fréquences telles que la génération d'harmoniques. La susceptibilité optique non linéaire peut révéler des caractéristiques qui ne sont pas observables dans la distribution linéaire de l'indice de réfraction. Pour des exemples biologiques, les protéines fibreuses telles que la myosine ou le collagène possèdent une susceptibilité optique non linéaire de second ordre et peuvent montrer une génération de fréquence de seconde harmonique ou de somme. Cependant, la généralisation des approches de tomographie par diffraction optique aux processus non linéaires n'est pas encore étudiée. Une approche similaire à la tomographie par diffraction optique peut être présentée par inversion des équations d'onde non linéaires régissant les processus de mélange de fréquences et reconstruisant la distribution 3D de la susceptibilité non linéaire à l'aide d'images complexes 2D des fréquences générées.

Dans cette thèse, je généralise la tomographie par diffraction optique conventionnelle aux milieux sensibles à la polarisation et non linéaires. Les méthodes proposées dans cette thèse

fournissent de nouvelles modalités de tomographie par diffraction optique qui peuvent être utilisées pour l'imagerie 3D d'échantillons anisotropes et non linéaires. Je présente des résultats numériques et expérimentaux pour divers exemples afin d'étudier la viabilité des modalités proposées. Un autre aspect de cette thèse est de présenter une solution itérative pour la tomographie par diffraction optique basée sur un modèle direct précis qui est aussi précis que la simulation électromagnétique pleine onde et peut inclure différents scénarios, tels que la dépolarisation, l'anisotropie et la non-linéarité. Comme les solutions pleine onde ne peuvent pas être facilement utilisées dans les approches d'optimisation itérative basées sur le gradient pour la tomographie par diffraction optique, un réseau neuronal informé par la physique est présenté et utilisé comme modèle avant dans une reconstruction itérative de la tomographie par diffraction optique.

Les méthodes étudiées dans cette thèse ont un impact significatif sur la tomographie par diffraction optique et l'imagerie 3D. Grâce à une analyse théorique, numérique et expérimentale approfondie, cette recherche vise à étudier les possibilités d'utilisation de ces techniques dans le développement de modalités d'imagerie 3D et sans marquage.

Mots clés : tomographie par diffraction optique, imagerie tridimensionnelle, diffusion optique, diffusion inverse, imagerie sensible à la polarisation, imagerie non linéaire, reconstruction itérative, apprentissage profond basé sur la physique.

Contents

Acknowledgements	i
Abstract (English/Français)	iii
List of figures	xi
List of tables	xvii
1 Introduction	1
1.1 Optical Diffraction Tomography: a 3D imaging technique	1
1.2 New modalities for ODT	4
1.3 Organization of the thesis	6
2 Theoretical background	9
2.1 Introduction	9
2.2 Optical scattering in inhomogeneous media	9
2.3 From 2D QPI to 3D ODT	12
2.3.1 Optical projection tomography: ray-optics approximation	13
2.3.2 Fourier diffraction theorem using Born approximation	13
2.3.3 Fourier diffraction theorem using Rytov approximation	15
2.3.4 Iterative approaches for ODT	16
2.4 Polarization of light and birefringence	17
2.5 Optical nonlinearity	19
3 Polarization-sensitive ODT	25
3.1 Introduction	25
3.2 Methodology	26
3.2.1 Theory	26
3.2.2 Approximation of the 3×3 scattering potential tensor with a 2×2 tensor .	30
3.2.3 Relationship between reconstructions performed in different polarization states	33
3.2.4 Experimental setup	34
3.3 Results and discussion	36
3.3.1 Numerical Phantom	36
3.3.2 Experiment	37
	vii

3.3.3	Coordinate-invariant polarization-sensitive contrast metrics	39
3.4	Conclusion	41
3.5	Follow-up works	41
4	Second-harmonic ODT	43
4.1	Introduction	43
4.2	Mathematical formalism	44
4.3	Results	47
4.3.1	3D $\chi^{(2)}$ reconstruction based on synthetic data	47
4.3.2	Explanation of the experimental setup	49
4.3.3	Experimental results on muscle tissue	50
4.4	Discussion	52
4.5	Conclusion and future work	54
5	Iterative ODT using physics-informed deep learning	57
5.1	Introduction	57
5.2	Methodology	59
5.2.1	Forward Model: MaxwellNet	59
5.2.2	Optical diffraction tomography using MaxwellNet	61
5.3	Results and Discussion	63
5.3.1	MaxwellNet results	63
5.3.2	Tomographic reconstruction results	66
5.4	Nonlinear MaxwellNet	70
5.5	Conclusion	70
6	Conclusion and future work	73
6.1	Summary of the results	73
6.2	Future work	75
A	Appendix: Polarization-sensitive ODT	77
A.1	Light Propagation in anisotropic inhomogeneous media and vectorial inverse scattering	77
A.2	Vectorial Beam Propagation method	81
A.3	Effect of a tilted polarizer	84
A.4	Numerical Results	84
A.5	Denoising and Iterative reconstruction	85
A.6	Muscle tissue Experiment	87
B	Appendix: Second-harmonic ODT	91
B.1	Wave propagation in nonlinear inhomogeneous media	91
B.2	Fourier diffraction theorem for SHG	92
B.3	Fourier diffraction theorem with corrected-field Born approximation	94
B.4	Muscle tissue experiment	94

C Appendix: Iterative ODT using physics-informed deep learning	97
C.1 Calculation of Physics-informed Loss	97
C.2 Training and Fine-tuning of MaxwellNet	98
C.3 Experimental Setup for ODT	99
Bibliography	109
Curriculum Vitae	111

List of Figures

1.1	Quantitative phase imaging of a $30\mu\text{m}$ liver tissue using off-axis digital holography. (a) The hologram with a zoomed-in inset presents interference fringes more clearly. (b) Fourier transform of the hologram showing the +1 and -1 orders. (c) The reconstructed phase profile. The phase profile is unwrapped.	3
2.1	ODT using Fourier diffraction theorem for a biological cancer cell, MDA-MB-231. (a) Schematic of ODT. (b) 2D QPI Phase images for two projections were measured holographically with a wavelength of 633nm. (c) Filling the Fourier domain of the scattering potential using Ewald's spheres of the measured projections using Rytov approximation. (d) 3D rendering of the reconstructed refractive index distribution.	14
2.2	3D ODT reconstruction for a digital phantom using different methods. The 3D refractive index reconstruction is shown in 3 different YX , XZ , and YZ planes indicated in the last row with dashed lines. Each row shows the ODT reconstruction using Born approximation, Rytov approximation, iterative reconstruction using TV regularize, and the ground-truth image, respectively.	15
2.3	Wide-field SH generation from Barium Titanate nano-particles illuminated with a polarized 280 femtosecond light source.	23
3.1	YX profiles of the conventional Rytov ODT reconstructions. On the top, we have the reconstruction of the corn starch kernel and multiple scattered fields were measured in the X-polarization when the illumination beam was (a) $+45^\circ$, and (b) -45° -polarized. (c) The difference between the two reconstructions of corn starch. Then, we have the reconstruction for an isotropic polystyrene bead when the illumination beam was (d) $+45^\circ$, and (e) -45° -polarized. (f) The difference between the two reconstructions of the polystyrene bead. All the colorbars show the refractive index and are unitless.	27
3.2	(a) Rotational Matrix described in Eq. 3.5, for polarization conversion of an oblique illumination. (b) Definition of the coordinate system.	29

- 3.3 (a) Schematic of the polarization-sensitive holography setup has been used to get vectorial scattered fields for different illumination angles. (b) Cross-polarized light can be measured from a corn starch granule when illuminated with a Y-polarized light. (c) Illumination pattern in the k-space: Circles are the desired pattern, and crosses are the experimental pattern which is measured using Fourier analysis of the holograms. 31
- 3.4 (a) Values of $f_{11}(\theta, \varphi)$, $f_{12}(\theta, \varphi)$, $f_{21}(\theta, \varphi)$, and $f_{22}(\theta, \varphi)$ for 90 projections with a conical pattern. (b) Calculated V_{xy}^{appro} , (c) V_{xy}^{true} , and (d) their difference regarding Eq. 3.13. (e) Histogram diagram of the true scattering potential values, and (f) the difference regarding Eq. 3.13. 33
- 3.5 Complex Jones matrix calculated for a birefringent digital phantom with an illumination angle of $\theta = 25^\circ$ and $\phi = 0^\circ$. The synthetic measurements were generated using the V-BPM. In order to visualize the complex values, brightness shows the amplitude and color-code shows the phase of each Jones matrix component. 35
- 3.6 Reconstruction of the digital birefringent phantom using the Rytov approximation. The first and second rows show YX, YZ, and XZ profiles of the ground-truth, and reconstruction of n_{xx} , respectively. The third and fourth rows show the same profiles for n_{yx} . Full tensor ground truth and reconstructions are presented in section 4 of Appendix A. The colorbars show the refractive index contrast and are unitless. 37
- 3.7 YX, XZ, and YZ profiles of the 3D RI tensor reconstruction of corn starch granule. The colorbars show the refractive index contrast and are unitless. 38
- 3.8 YX profiles of the 3D reconstructions of the RI tensor components, n_{xx} and n_{xy} , for a 20 μ m thick muscle tissue in three different depths. The inset shows a 2.5X magnified section of n_{xy} YX profile which clarifies the sarcomere structure with A-bands and I-bands in one muscle fiber. The colorbars show the refractive index contrast and are unitless. 39
- 3.9 A comparison between the YX profiles of the 3D reconstructions of (a) n_{xy} and (b) phase retardation for corn starch granule. (c) A 3D rotating rendering of the phase retardation. 40
- 4.1 3D reconstruction of second-order susceptibility tensor using synthetic data. The 6 elements of the second-order susceptibility tensor achieved using Eq. 4.3 are presented in (a) $\chi_{11}^{(2)}$, (b) $\chi_{12}^{(2)}$, (c) $\chi_{16}^{(2)}$, (d) $\chi_{21}^{(2)}$, (e) $\chi_{22}^{(2)}$, and (f) $\chi_{26}^{(2)}$, respectively. Each figure presents the 3D reconstruction in YX, YZ, and XZ planes. 47
- 4.2 TV-based iterative reconstruction of second-order susceptibility tensor using synthetic data. The 6 elements of the second-order susceptibility tensor achieved using Eq. 4.5 are presented in (a) $\chi_{11}^{(2)}$, (b) $\chi_{12}^{(2)}$, (c) $\chi_{16}^{(2)}$, (d) $\chi_{21}^{(2)}$, (e) $\chi_{22}^{(2)}$, and (f) $\chi_{26}^{(2)}$, respectively. 48

4.3	(a) Experimental setup for multi-angle SH-holography. (b) Fourier transform of the SH hologram from muscle fiber. (c-d) Holographic extraction of the amplitude and phase of the SH-generated field from the muscle fiber as the sample illuminated with a tilted fundamental Gaussian wave. The amplitude values are normalized and the phase map is shown in the color code of (d) as the brightness is modulated with the amplitude. (e) The 1D profile of the amplitude (blue) and phase (orange) of the SH-generated field along the dashed line is shown in (c). We can see the periodic amplitude and phase variation, amplitude dips between myosin crystals, and $\pm\pi$ jumps in phase. (f) Structure of the muscle tissue sarcomere.	51
4.4	SH Tomographic reconstruction. (a) 2D YX profile of the 3D reconstruction of $\chi^{(2)}$ distribution in three different Z planes. The values are normalized to the [-1,1] range. (b) 2D YX profile the 3D refractive index reconstruction in three different Z planes.	52
4.5	(a) 3D rendering of the $\chi^{(2)}$ reconstruction using SH-ODT. (b) 3D rendering of the refractive index reconstruction using linear ODT.	53
5.1	Schematic description of MaxwellNet, with U-Net architecture, and its application for tomographic reconstruction. The input is a refractive index distribution and the output is the envelope of the scattered field. The output is modulated by the fast-oscillating term $e^{jk_0 n_0 z}$ to compute the physics-informed loss for tuning the weights. To perform tomographic reconstruction, we employ MaxwellNet to minimize a data-driven loss that quantifies the disparity between measured and predicted projections. The addition of a regularization term can improve the reconstruction.	60
5.2	Results of MaxwellNet and its comparison with COMSOL. (a,b) Two test cases from the digital phantom dataset and the prediction of the real and imaginary of the envelope of the scattered fields using MaxwellNet, COMSOL, and their difference. (c) Scattered field predictions from the network trained in (a,b) for the case of an experimentally measured RI of HCT-116 cancer cell and comparison with COMSOL. The difference between the two is no longer negligible. (d) Comparison between MaxwellNet and COMSOL after fine-tuning the former for a set of HCT-116 cells. MaxwellNet predictions reproduce much more accurate results after fine-tuning.	64
5.3	Results of MaxwellNet3D and its comparison with COMSOL. The RI distribution is shown in (a). The real part of the envelope of the scattered field calculated by MaxwellNet3D is shown in (b), calculated by COMSOL in (c), and their difference in (d). The imaginary part of the envelope of the scattered field calculated by MaxwellNet3D, COMSOL, and their difference are presented in (e-g), respectively.	65

5.4	Tomographic reconstruction of RI using MaxwellNet. (a) The RI reconstruction was achieved by Rytov, MaxwellNet, and the ground-truth. (b) 1D RI profile at $z = 0$ (plane of best focus), for Rytov (green), MaxwellNet (blue), and the ground-truth (orange).	67
5.5	Tomographic RI reconstruction of 3D sample using MaxwellNet. The RI reconstruction is achieved by Rytov, MaxwellNet, Learning tomography, and the ground-truth in different rows at YX, YZ, and XZ planes in the center of the sample.	68
5.6	Tomographic RI reconstruction of a polystyrene micro-sphere immersed in water. The projections are measured with off-axis holography for different angles. The RI reconstruction achieved by Rytov, MaxwellNet, and Learning tomography are presented at YX, YZ, and XZ planes in the center of the sample.	69
A.1	Comparison of the scattered vectorial fields for the birefringent digital phantom based on the vectorial single scattering and V-BPM. Four rows represent the components of the Jones matrix. First and second columns show the imaginary part of Jones components based on the single scattering and V-BPM model, respectively. Third and fourth columns show the real parts of them, and the last column shows the absolute value of the difference between the single scattering model and V-BPM.	80
A.2	Error of the single scattering forward model with respect to V-BPM for different digital phantoms as the degree of birefringence increases.	82
A.3	Verification of V-BPM using FEM: calculated $ E_y / E_x^{in} $ by FEM (COMSOL) for (a) normal incidence and (b) oblique incidence with $\theta = 25^\circ$ and using V-BPM for (c) normal and (d) oblique incidence with $\theta = 25^\circ$	83
A.4	The off-diagonal component of the Jones matrix of an ideal polarized as it is illuminated with a tilted beam as we scan φ	84
A.5	The Jones matrix of the digital phantom calculated with the V-BPM for 3 different projections. Same data for 180 projections are used to reconstruct the 3D phantom.	85
A.6	Polarization-sensitive reconstruction of the digital phantom using the Rytov approximation. For each component of the tensor, we show the ground-truth and the reconstruction in YX, YZ, and XZ planes. Dashed lines show the lines that we show the profile of the index along them.	86
A.7	Eigen-value characterization of the refractive index tensor of the digital phantom: (a) Profile of the 3D Slow-axis direction at $z = 0\mu\text{m}$ for the ground-truth, (b) Profile of the 3D Slow-axis direction at $z = 0\mu\text{m}$ for the 3D reconstruction, (c) Profile of the 3D Birefringence ($\mu_n^1 - \mu_n^2$) of the ground-truth, (d) Profile of the 3D Birefringence ($\mu_n^1 - \mu_n^2$) of the 3D reconstruction.	87
A.8	Iterative reconstruction of the digital phantom: 1st row: ground-truth, 2nd row: direct iterative reconstructions, 3rd row: iterative reconstruction using TV regularization.	88
A.9	The cross-polarized light amplitude $ U_{xy}^s ^2$ which is measured for the muscle tissue.	88

A.10	The phase of the scattered field. (a) for U_{xy}^s and (b) for U_{xa}^s . The background phase is random due to the zero intensity in the cross-polarized light. By contrast, in (b) the background phase can be easily calibrated and unwrapped.	89
B.1	(a) Bright-field microscopy of the muscle fiber tissue using green light. (b) Wide-field SH image of the muscle fiber in the same region.	95
C.1	Training and fine-tuning of MaxwellNet. (a) Training (blue) and validation (orange) loss of MaxwellNet for Digital cell phantoms dataset. (b) Fine-tuning the pretrained MaxwellNet for a dataset of HCT-116 cells for 1000 epochs. (c) Examples of the HCT-116 dataset.	98
C.2	Experimental setup for multiple illumination angle off-axis holography. HW: Half-wave plate, P: Polarizer, BS: Beam splitter, L: Lens, Obj: microscope objective, M: Mirror.	99



List of Tables

5.1 MaxwellNet computation time comparison	66
--	----

1 Introduction

1.1 Optical Diffraction Tomography: a 3D imaging technique

Optical imaging is a powerful tool that uses visible light to study a wide range of biological and non-biological phenomena, from the structure of cells and tissues to the dynamics of molecular interactions. It has been used to study a variety of topics including cell division [1], neuron imaging [2], drug delivery systems [3], cancer detection [4], and tissue engineering [5], to name a few. The development of new optical imaging techniques has enabled researchers to gain insight into complex biological phenomena at the molecular level with minimal invasiveness, high resolution, and high repeatability.

In an optical imaging system, the illumination part specifies how the sample is illuminated with white light or a coherent laser source, and the measurement part and the interaction of light with the sample specify the characteristics of the image and the contrast mechanism to form that image. The final optical image is formed on the camera or human eye and these last components in the optical imaging setups are normally only able to measure and quantify the intensity of the light. This is the main reason that the introduction of contrast mechanisms gets important in an optical imaging system.

The transmittance of a thin 2-dimensional (2D) phase-only object can be expressed with a phase term as $\exp\{j\phi(x, y)\}$. When the sample is illuminated with U_i , the intensity of the total field which will be detected on the camera is $\|U_t\|^2 = \|\exp\{2j\phi(x, y)\} \times U_i\|^2 = \|U_i\|^2$. As a result, the intensity of the image can only show features that are visible in the absorption of the sample, and not the phase or the real part of the refractive index. In order to introduce a contrast mechanism to detect features in the sample, there are two general methods: (i) Fluorescence microscopy which uses fluorescent dyes or proteins to label specific molecules or structures within a sample. These dyes get excited in a specific wavelength and emit light in a slightly different wavelength, allowing us to visualize features of interest in the sample with high contrast in the intensity image. (ii) A phase measurement system that allows the use of the refractive index of the sample as a contrast agent in the image. Fluorescence microscopy requires labeling the sample with fluorophores, a high intensity to have enough fluorescence

emission, and it suffers from photobleaching and environmental sensitivity, especially for live imaging [6], [7]. Therefore, label-free imaging modalities based on phase measurements that utilize the refractive index of the sample as the contrast agent are very useful in the study of biological samples.

For an approximately 2D thin transparent object, the accumulated phase of the total field with respect to the background will be $\phi(x, y) = k_0 L (n(x, y) - n_0)$, in which $k_0 = 2\pi/\lambda$ is the vacuum wavenumber, λ is the illumination wavelength, n_0 is the refractive index of the background, L is the thickness of the thin object, and $n(x, y)$ is the refractive index of the inhomogeneous object. Therefore, a measurement of the phase distribution can provide us with information about the refractive index contrast of the sample. As mentioned earlier, the camera or the human eye as the detector in the imaging system is only able to measure the intensity of light and the phase distribution should be transformed to the intensity, in order to be measured. There are two main methods for this transformation: applying a phase mask to the scattered light, and digital holography. In the earlier mechanism, which was originally proposed by Zernike phase mask [8], a phase mask will add a $\pi/2$ phase to the illumination field while keeping the phase of the scattered field $U_s = U_t - U_i$. As a result, the detected intensity will be $\|e^{j\pi/2}U_i + (e^{j\phi(x,y)} - 1)U_i\|^2 \approx [1 + 2\phi(x, y)] \|U_i\|^2$.

Zernike's approach for phase contrast imaging provides an approximated and qualitative phase measurement. However, in order to measure the amplitude and phase of the optical image simultaneously and accurately, an interference-based technique, such as holography, should be used. The principle of holography, which was originally invented by Gabor [9], is based on the interference pattern of a signal and reference optical beams. We can write the complex signal beam whose amplitude and phase are of interest as $S(x, y)$, and the complex reference beam as $R(x, y)$. The measured intensity pattern will be,

$$I(x, y) = \|S(x, y) + R(x, y)\|^2 = \|S(x, y)\|^2 + \|R(x, y)\|^2 + S(x, y)R^*(x, y) + S^*(x, y)R(x, y) \quad (1.1)$$

if we consider the off-axis configuration in which the reference beam is a tilted plane wave of $R(x, y) = 1e^{j(k_x^R x + k_y^R y)}$, and the signal beam has the phase of $\phi(x, y)$, the measured intensity pattern is,

$$I(x, y) = \|S(x, y) + R(x, y)\|^2 = 1 + \|S(x, y)\|^2 + \|S(x, y)\| \cos(\phi(x, y) - k_x^R x - k_y^R y) \quad (1.2)$$

The phase and amplitude of the signal beam can be retrieved from such a hologram using Fourier domain holography. An example hologram of liver tissue is shown in Fig. 1(a) which is measured with the setup that I will discuss in section 3. We can see the +1 and -1 orders in the Fourier transform of the hologram, which are generated because of the interference with the off-axis reference beam. By filtering the +1 order, shifting it to the center of the Fourier domain, and taking the inverse Fourier transformation, one can reconstruct the complex signal beam, $S(x, y)$, and its corresponding phase and amplitude. The Fourier transform of the hologram of the liver tissue and the unwrapped reconstructed phase are presented in Fig. 1(b-

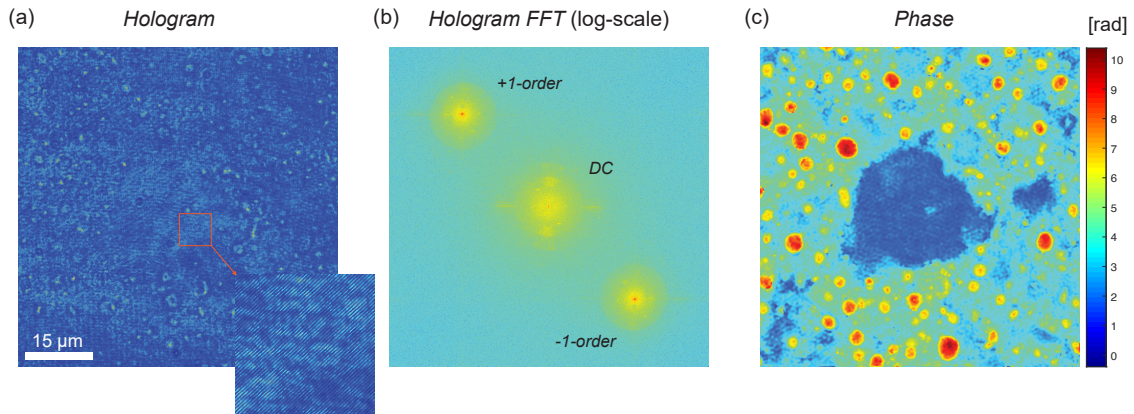


Figure 1.1: Quantitative phase imaging of a $30\mu\text{m}$ liver tissue using off-axis digital holography. (a) The hologram with a zoomed-in inset presents interference fringes more clearly. (b) Fourier transform of the hologram showing the +1 and -1 orders. (c) The reconstructed phase profile. The phase profile is unwrapped.

c). We can see that off-axis holography can provide useful morphological information about the biological sample of interest by reconstructing a 2D phase profile of light in a label-free mechanism.

For a thin 2D sample, the phase profile will be proportional to the refractive index contrast of the sample with respect to the background medium. However, a single phase profile cannot provide complete and quantitative information about the refractive index distribution of a three-dimensional (3D) sample which should be represented as $n(x, y, z)$. Developing 3D imaging modalities was always of interest to present more structural information about biological and non-biological samples. Three main categories of 3D optical imaging include confocal microscopy [10], light-sheet microscopy [11], and optical coherence tomography (OCT) [12]. The first two approaches usually use Fluorescence labeling as the contrast mechanism and can provide a reasonable resolution for biological applications. OCT, which suffers from a low resolution, reconstructs the tomograms of the sample by light scattering due to the inhomogeneous refractive index distribution using a low-coherence interferometry technique. As a result, label-free high-resolution techniques are desirable for 3D optical imaging.

Optical diffraction tomography (ODT) is a useful technique to incorporate digital holography and quantitative phase imaging into a 3D microscopy modality. In ODT, the sample is illuminated from multiple angles and phase and amplitude measurements are collected holographically for each illumination angle. We call these 2D images different projections. Then, a reconstruction algorithm is used to combine the 2D projections into a 3D tomogram of the refractive index distribution of the sample. The first idea of ODT was proposed by Emil Wolf in 1969 [13] by establishing the Fourier diffraction theorem using the Born approximation. Subsequently, ODT has undergone intensive research in terms of experimental and algorithmic viewpoints [14]–[16]. For example, Wolf's method was used with the Rytov approximation

to improve reconstructions [17]. Experimental aspects such as illumination rotation [18], [19], sample rotation [20], and wavelength scanning [21] have been thoroughly investigated. Phase-contrast tomography of cells inside the microfluidic channels is also presented [22], [23].

We can consider ODT as an inverse scattering problem. In ODT, we use the 2D scattered field projections from the 3D object and reconstruct the 3D refractive index of the inhomogeneous object. In the forward scattering problem, the known 3D object is illuminated from different angles and we can calculate 2D projections with an approximative analytical model or full-wave simulation. The forward model from the refractive index distribution to the 2D projections is nonlinear due to the multiple scattering [24]. If we approximatively linearize the forward model, an inversion is possible to reconstruct the 3D refractive index distribution (as the input of the forward model) from 2D projections (as the output of the forward model). The linearization can be achieved using first-order Born or Rytov approximations [13], [25] and can provide a direct reconstruction scheme for ODT. I explain the theory of these direct approaches in chapter 2. The approximated direct reconstruction can suffer from low axial resolution, due to the missing frequencies known as the missing-cone problem [26], and multiple scattering. Alternatively, if a more accurate 3D ODT reconstruction with a nonlinear forward model is of interest, an iterative reconstruction approach should be used [27]–[29]. These iterative approaches are based on three steps: a nonlinear forward model which calculates the 2D projections for an estimate of the refractive index distribution, a loss function based on the difference between the calculated projections and the measurements, and a prior knowledge about the sample, and minimization of this loss function iteratively to improve the estimation of the 3D refractive index distribution. All of these recent studies on ODT provide useful reconstruction methods for various biological and non-biological applications.

1.2 New modalities for ODT

All of the recent studies on ODT concentrate on developing experimental or computational methods that require simpler experimental setups, use fewer illumination angles, or improve the 3D reconstruction of the refractive index distribution. However, all of the previously studied ODT approaches were based on a scalar formalism for light scattering. The Helmholtz equation which governs the light scattering in inhomogeneous media is originally a vectorial formalism. For a sample with scalar refractive index distribution of $n(r)$, we can write the Helmholtz equation as $\nabla \times \nabla \times U_t(r) - k_0^2 n^2(r) U_t(r) = 0$ which can be rewritten as $\nabla^2 U_t(r) + k_0^2 n^2(r) U_t(r) = -\nabla [U_t \cdot \nabla \log(n^2(r))]$. The gradient of the refractive index on the right side of this equation can be considered a vectorial source term that can change or create different vectorial components of the field. On the other hand, there are many biological and non-biological samples that are anisotropic, meaning that the polarization of light is important in the interaction of light with such samples. The refractive index of these samples cannot be represented with a scalar value, should be formulated with a tensor, $\vec{n}(r)$, and a vectorial Helmholtz equation is required to describe light scattering from these samples. This issue

limits the use of scalar ODT techniques for such birefringent samples but also it can provide the possibility to utilize polarization-sensitive ODT to uncover features that are not visible in the scalar refractive index distribution.

A vectorial formalism for the Fourier diffraction theorem and ODT can reconstruct the 3D distribution of different components of the refractive index tensor. These components can be considered new modalities for ODT and provide new information that is not visible in the scalar refractive index reconstruction. Additionally, an eigenvalue decomposition of the reconstructed refractive index tensor can provide new contrast agents for ODT such as 3D phase retardation and 3D slow-axis/fast-axis orientation. For such purpose, polarization-sensitive holographic measurements are required to retrieve the phase and amplitude of different components of the electric field vector for each illumination angle and a vectorial formalism for Fourier diffraction theorem can map these multi-angle polarization-sensitive holographic measurements to the refractive index tensor. This is what we aim for in chapter 3 of this thesis.

On the other hand, the previous studies on ODT were based on the linear optical interaction of the illumination with the sample. To be clearer, even though that optical scattering is nonlinear with respect to the refractive index distribution due to the multiple scattering, it can be considered linear with respect to the illumination field, when considering low-intensity illumination. However, in the high-intensity illumination regime, the interaction of light with the sample can become nonlinear, leading to many phenomena such as second harmonic generation, sum frequency generation, self-focusing, and spectral broadening. This is the basis of the field of Nonlinear Optics [30] which was historically observed in 1961 shortly after the construction of the laser [31]. The linear refractive index which is correlated with the first-order susceptibility distribution, $\chi^{(1)}$, is not a sufficient distribution to describe the light interaction in the case of optical nonlinearity. In these scenarios, the electric polarizability should be represented with a nonlinear series of the electric field,

$$P = \epsilon_0 \chi^{(1)} E + \epsilon_0 \chi^{(2)} E^2 + \epsilon_0 \chi^{(3)} E^3 + \dots \quad (1.3)$$

where ϵ_0 is the vacuum permittivity. The higher-order susceptibility terms can reveal new information in the material which cannot be seen in the first-order susceptibility, or equivalently refractive index distribution. The existence of these higher-order susceptibility terms in the material leads to frequency mixing phenomena such as harmonic generation. These higher-order susceptibility terms or higher-order harmonics generated by them can be considered new modalities for optical imaging and microscopy [32]. This is the idea of nonlinear ODT that I studied in this thesis for second-order susceptibility. We can generalize quantitative phase imaging to nonlinear optical harmonic generation to measure the phase and amplitude of the generated harmonic signal. If we have a single-frequency pump signal and a second-order material, we can observe second-harmonic generation (SHG) from the sample which can be measured holographically. Then, the generalization of ODT to the nonlinear regime will be collecting multi-angle harmonic holography images and reconstructing the 3D distribution of

the nonlinear susceptibility. The 3D tomographic reconstruction of nonlinear susceptibility can provide morphological information about the sample which is not visible in the linear refractive index.

1.3 Organization of the thesis

As mentioned in the previous subsection, the main idea of this thesis is to investigate novel modalities for ODT, and further analyze how we can use the same techniques and approaches of conventional ODT to other modalities such as birefringence and optical nonlinear susceptibilities.

In Chapter 2, I present an overview of the theoretical framework that serves as the foundation for the remainder of the thesis. A description of the optical scattering in inhomogeneous media is presented starting from Maxwell's equations to the time-independent Helmholtz equation. Then, I present solutions for the forward optical scattering problem based on the Helmholtz equation. I discuss a recursive solution for optical scattering, beam propagation method, and Lippmann-Schwinger solution. Afterward, I discuss direct approaches for 3D reconstruction of the refractive index based on ray-optics approximation, first-order Born approximation, and first-order Rytov approximation. Additionally, a brief discussion about the iterative methods for ODT will be discussed and lastly, I will provide the theoretical basis necessary to study polarization-sensitive inhomogeneous media and nonlinear optical interaction.

In chapter 3, I present polarization-sensitive ODT for 3D tomographic reconstruction of the refractive index tensor of a birefringent sample using multi-angle polarization-sensitive holographic images. Methodology and theoretical formalism as well as the experimental setup will be explained, and then synthetic and experimental results will be presented. To validate our theoretical framework, we present synthetic results for a digital birefringent phantom whose refractive index tensor is known. Additionally, we present experimental results to demonstrate the viability of this new modality for ODT. Finally, we discuss coordinate-invariant contrast agents for polarization-sensitive ODT.

In chapter 4, we report the tomographic reconstruction of the three-dimensional second-order susceptibility tensor using two-dimensional measurements of the second-harmonic- (SH-) generated fields at the double frequency for different illumination angles and polarization states. The method is inspired by conventional linear optical diffraction tomography (ODT) and is generalized for the nonlinear second-harmonic scenario. The SH-generated complex fields are measured using a harmonic holography setup. As a group of centro-asymmetric features is required for the sample to have second-order susceptibility and generate SH light, the SH tomographic reconstruction can provide a background-free imaging technique showing features of interest that possess asymmetry at the molecular level. We present synthetic and experimental results for barium-titanate nano-particles and muscle tissue fibers to show the viability of our theoretical formalism and 3D reconstruction methods. Our results demonstrate a new modality for ODT which can be potentially used to acquire morphological information

for biological optical imaging. The second-order susceptibility distribution can be considered a nonlinear modality for ODT.

In chapter 5, we discuss an iterative approach for ODT using a physics-informed neural network as the forward model for tomographic reconstructions of biological samples. We demonstrate that we can accurately predict the scattered field by training this network with the Helmholtz equation as a physical loss. It will be shown that a pre-trained network can be fine-tuned for different samples and used for solving the scattering problem much faster than other numerical solutions. We evaluate our methodology with numerical and experimental results. Our physics-informed neural networks can be generalized for any forward and inverse scattering problem.

In Chapter 6, I will summarize the thesis, provide a conclusion, and discuss the future work that can be conducted based on the material of this thesis.

2 Theoretical background

2.1 Introduction

An inhomogeneous isotropic sample can be represented with refractive index distribution, $n(r) = \sqrt{\epsilon_r}$, and the light interacting with the sample is an electromagnetic wave which can be described with the electric field $E(r, t)$. Maxwell's equations can describe the interaction of light with the sample. In this chapter, I present an overview of the required theoretical background for light scattering and inverse scattering from inhomogeneous samples. Starting from Maxwell's equations I will reach the frequency domain wave equation to describe light interaction with the sample. Then, I will discuss direct and iterative approaches for the inverse scattering problem. At the end of this chapter, the theoretical background for polarization-sensitive light scattering and nonlinear optical harmonic generation will be presented.

2.2 Optical scattering in inhomogeneous media

The propagation of the electromagnetic wave $E(r, t)$ in an inhomogeneous non-magnetic media can be formulated using a wave equation derived from Maxwell's formalism [33],

$$\nabla \times \nabla \times E(r, t) + \frac{1}{c^2} \frac{\partial^2 E(r, t)}{\partial t^2} = -\mu_0 \frac{\partial^2 P(r, t)}{\partial t^2} \quad (2.1)$$

where c is the speed of light, μ_0 is the vacuum permeability, and $P(r, t) = \epsilon_0 (\epsilon_r(r, t) - 1) E(r, t)$ is the polarizability of the medium with the relative permittivity of $\epsilon_r(r) = n^2(r)$ in the linear and scalar optics regime. Considering the monochromatic and coherent light with the frequency of ω , and also a time-invariant medium with $\frac{\partial \epsilon_r(r, t)}{\partial t} = 0$, the time dependence of the electric field can be assumed as $e^{-j\omega t}$. For this case, we can simplify Eq. 2.1 in the frequency domain as,

$$\nabla \times \nabla \times E(r, \omega) - k_0^2 n^2(r) E(r, \omega) = 0 \quad (2.2)$$

where $k_0 = \omega/c = 2\pi/\lambda$ is the free space wave number, and λ is the wavelength. According to the relationship $\nabla \times \nabla \times E = \nabla(\nabla \cdot E) - \nabla^2 E$ and the fact that $\nabla \cdot (\epsilon_r E) = 0$, we can rewrite Eq. 2.2 as,

$$\nabla^2 E(r, \omega) + k_0^2 n^2(r) E(r, \omega) + 2\nabla [E(r, \omega) \cdot \nabla \ln(n(r))] = 0 \quad (2.3)$$

if we assume that $n(r)$ is varying slowly with respect to the spatial domain r , we can neglect the third term in Eq. 2.3. As a result, different components of the electric field vector will be decoupled from each other and we can consider a scalar field $U(r)$ instead of the electric field vector. We can rewrite Eq. 2.3 by defining the scattering potential $V(r) = k_0^2/4\pi (n^2(r) - n_0^2)$ as,

$$\nabla^2 U(r) + k_0^2 n_0^2(r) U(r) = -4\pi V(r) U(r) \quad (2.4)$$

We can decompose the total scalar field to the scattered and incident fields as $U(r) = U_i(r) + U_s(r)$. As the background medium, n_0 is homogeneous, we have $\nabla^2 U_i(r) + k_0^2 n_0^2(r) U_i(r) = 0$ and we can rewrite Eq. 2.4 as follows,

$$(\nabla^2 + k_0^2 n_0^2(r)) U_s(r) = -4\pi V(r) U(r) \quad (2.5)$$

In order to present an integral form, we can consider the Green's function of Eq. 2.5 as the solution of its left side to a *delta* function source,

$$G(r, r') = \frac{e^{jk_0 n_0 |r-r'|}}{|r-r'|} \quad (2.6)$$

which is valid in the case of the Sommerfeld boundary condition. Using this Green's function, the integral form of Eq. 2.5 will be,

$$U_s(r) = \int_{\mathcal{D}'} G(r, r') V(r') U(r') dr' \quad (2.7)$$

The integration is in the computational domain of \mathcal{D}' , however since $V(r')$ is zero elsewhere of the scatterer, it will be automatically integrated with the region of the non-zero scattering potential. The nonlinearity of optical scattering with respect to the scattering potential $V(r)$ is clear in Eq. 2.7 as we have $U(r') = U_s(r') + U_i(r')$ on the right side. It should be noted that this is just an integral form, and not a solution, for the optical scattering problem since $U_s(r)$ exists on both sides of Eq. 2.7 and we cannot simply find it using this equation. In order to solve this integral equation we need to propose approximative or semi-numerical solutions. Hereby, I discuss 4 different solutions for Eq. 2.7.

The simplest way to solve Eq. 2.7 for the optical scattering problem is to use first-order Born approximation and linearize this equation for weakly scattering objects. According to the first-order Born approximation, we can neglect the scattered field in comparison with the incident field, $U_s(r) \ll U_i(r)$, on the right side of Eq. 2.7. Using this approximation, the

scattered field can be easily computed by taking the following integral,

$$U_s(r) = \int_{\mathcal{D}'} G(r, r') V(r') U_i(r') dr' \quad (2.8)$$

This solution is valid only for weakly scattering objects with a very low refractive index contrast and small size [34]. We can propose a better recursive solution for Eq. 2.7. To do so, we can have a perturbative expansion of the scattered field as $U_s = \sum_q U_s^{(q)} = U_s^{(0)} + U_s^{(1)} + U_s^{(2)} + \dots$ in which $U_s^{(0)} = 0$, $U_s^{(1)} = \int_{\mathcal{D}'} G(r, r') V(r') U_i(r') dr'$, and

$$U_s^{(q)}(r) = \int_{\mathcal{D}'} G(r, r') V(r') U_s^{(q-1)}(r') dr' \quad \text{for } q > 2 \quad (2.9)$$

This recursive solution can provide a more accurate solution for optical scattering, especially if the scattered field is not negligible in comparison with the incident field. However, considering a large number for the order of the perturbation series will increase the computation time and complexity of this forward solution. Additionally, there is no clear way to know how many orders are required to get an accurate solution and if the scattered field orders are not degrading with an increase in q , convergence can not be guaranteed.

Another solution to Eq. 2.7 is using Lippmann–Schwinger equation [35]. We can write Eq. 2.7 in an operator notation,

$$\vec{U}_s = \tilde{\mathcal{G}} \tilde{V} \vec{U} \quad (2.10)$$

where considering N voxels in the computational domain \mathcal{D} , we have $\vec{U}_s \in \mathbb{C}^N$, and $\vec{U} \in \mathbb{C}^N$, $\tilde{\mathcal{G}} \in \mathbb{C}^{N \times N}$, and $\tilde{V} \in \mathbb{R}^{N \times N}$. Based on the definition of the scattered field, $\vec{U}_s = \vec{U} - \vec{U}_i$, we can rewrite Eq. 2.10 as $[\mathbb{I} - \tilde{\mathcal{G}} \tilde{V}] \vec{U} = \vec{U}_i$ with $\mathbb{I} \in \mathbb{R}^{N \times N}$ being the identity matrix, which leads to

$$\vec{U} = [\mathbb{I} - \tilde{\mathcal{G}} \tilde{V}]^{-1} \vec{U}_i \quad (2.11)$$

Looking more carefully at Eq. 2.10, the $\tilde{\mathcal{G}}$ operator is responsible for free propagation in the homogeneous background media, and the \tilde{V} operator is responsible for the light scattering from the scattering potential. Although this solution is computationally heavy as it requires a matrix inversion in a domain bigger than the actual computational domain, it can provide more accurate solutions than the first-order Born approximation in the case of multiple scattering [35].

The Beam Propagation Method (BPM) is the final technique to be discussed for resolving scalar optical scattering. BPM is a semi-analytical split-step solution for light scattering and propagation in inhomogeneous media which is based on two approximations: neglecting the reflection, and slowly-varying envelope approximation. The idea of BPM is to replace the scalar field $U(r)$ in Eq. 2.4 with $A(r) e^{jk_0 n_0 z}$ and approximate $V(r) \approx k_0^2 n_0 / 2\pi \delta n(r)$ for small

$\delta n(r) = n(r) - n_0$. As a result, we can write,

$$\begin{aligned} \frac{\partial^2 (A(r)e^{jk_0 n_0 z})}{\partial z^2} + \nabla_t^2 A(r)e^{jk_0 n_0 z} + k_0^2 n_0^2 A(r)e^{jk_0 n_0 z} + 2k_0^2 n_0 \delta n(r) A(r)e^{jk_0 n_0 z} \\ = \left[\nabla_t^2 + \frac{\partial^2}{\partial z^2} + 2jk_0 n_0 \frac{\partial}{\partial z} + 2k_0^2 n_0 \delta n(r) \right] A(r)e^{jk_0 n_0 z} = 0 \end{aligned} \quad (2.12)$$

where ∇_t^2 is the Laplacian in the transverse direction. We can remove the $\partial^2/\partial z^2$ term if we assume the slowly varying envelope approximation. In this case, the envelope of the field $A(r)$ can be found using the following simplified differential equation,

$$\frac{\partial A(r)}{\partial z} = \left(\frac{j\nabla_t^2}{2k_0 n_0} + jk_0 \delta n(r) \right) A(r) \quad (2.13)$$

we can write Eq. 2.13 in the operator form as,

$$\frac{\partial A(r)}{\partial z} = \tilde{D}A(r) + \tilde{P}A(r) \quad (2.14)$$

$\tilde{D} = j\nabla_t^2/2k_0 n_0$ is the diffraction operator which is responsible for the propagation of the beam in the homogeneous n_0 medium, and $\tilde{P} = jk_0 \delta n(r)$ is the phase modulation term which is responsible for the accumulated phase due to the refractive index contrast of $\delta n(r)$. The solution of Eq. 2.14 is,

$$A(x, y, z + dz) = e^{(\tilde{D} + \tilde{P})dz} A(x, y, z) \approx e^{\tilde{P}dz} e^{\tilde{D}dz} A(x, y, z) \quad (2.15)$$

The approximation is due to the fact that $\exp((\tilde{D} + \tilde{P})dz) \neq \exp(\tilde{D}dz) \times \exp(\tilde{P}dz)$ as the operators \tilde{D} and \tilde{P} do not commute. However, for small step size dz we can have this approximation [36]. Eq. 2.15 can be represented in a clear form by writing the diffraction operator in the Fourier domain,

$$A(x, y, z + dz) = e^{jk_0 \delta n(r) dz} \mathcal{F}_{2D}^{-1} \left\{ e^{-j \frac{k_x^2 + k_y^2}{2k_0 n_0} dz} \times \mathcal{F}_{2D} \{ A(x, y, z) \} \right\} \quad (2.16)$$

where \mathcal{F}_{2D} represents the 2D Fourier transform in the x , and y directions, and k_x , and k_y are the Fourier spatial frequencies. Eq. 2.16 is the paraxial BPM solution for the optical scattering in inhomogeneous media. BPM can be computationally implemented by splitting the computational domain \mathcal{D} into multiple slices in the z direction and use Eq. 2.16 to calculate the envelope of the field at each slice based on the envelope in the previous slice. BPM can provide more accurate solutions in comparison with Born approximation [27], [36].

2.3 From 2D QPI to 3D ODT

In the previous section, we discussed different solutions for forward optical scattering from inhomogeneous media. The solutions of section 2.2 can calculate 2D complex scattered light

as a 3D inhomogeneous sample is illuminated. In this section, we discuss the inverse problem known as optical tomography to find the 3D object from 2D quantitative phase images (QPI). We can formulate the optical tomography problem as follows: The unknown 3D object with the scattering potential distribution $V(x, y, z)$ is illuminated with a plane wave U_i^l from different angles. The index l defines the projection. The total complex field is measured on a 2D plane for this projection, $U^l = U_s^l + U_i^l$. The tomography problem is to use the complex projections $U^l(x', y', z' = z_0)$ measured on the 2D imaging plane of $z' = z_0$ for multiple illumination angles of $l = 1, 2, \dots, L$ and reconstruct the 3D distribution of the scattering potential $V(x, y, z)$. A schematic of this process can be found in Fig. 2.1. In the rest of this section, we will discuss different approximations and methods for tomographic reconstruction.

2.3.1 Optical projection tomography: ray-optics approximation

The first approximation I discuss for optical tomography is ray optics. In the ray-optics regime, we assume that the wavelength of the object is much shorter than the correlation size of the inhomogeneity variations in the object. We can represent this approximation by neglecting the diffraction operator in BPM and considering only the phase modulation operator. By defining the phase of the measured 2D projection, $\phi(x', y')$ as $U(r') = U_i e^{j\phi(r')}$, Eq. 2.16 can be written as,

$$\phi(x', y', z' = z_0) = k_0 \int_{\mathcal{Q}'} \delta n(x', y', z') dz' \quad (2.17)$$

Eq. 2.17 shows that the accumulated phase is a line integral of the refractive index contrast along the projection direction. This line integral is referred to as the Radon transform [37]. As a result, the accumulated phase is proportional to the Radon transform of the refractive index contrast. At this step, we can use inverse Radon transform based on filtered back projection to reconstruct the 3D refractive index contrast, $\delta n(r)$ with 2D phase profiles achieved by illuminating the sample from multiple different angles [14], [15].

2.3.2 Fourier diffraction theorem using Born approximation

In order to invert the forward scattering problem with diffraction, we use linearization based on the first-order Born approximation in Eq. 2.8. This equation represents a linear integral relationship between the scattering potential, $V(r)$, and the scattered field. To invert this equation, we can write the Green's function as,

$$G(r, r') = \frac{e^{jk_0 n_0 |r-r'|}}{|r-r'|} = \frac{j}{2\pi} \iint_{-\infty}^{\infty} \frac{1}{k_z} e^{j[k_x(x-x') + k_y(y-y') + k_z(z-z')]} dk_x dk_y \quad (2.18)$$

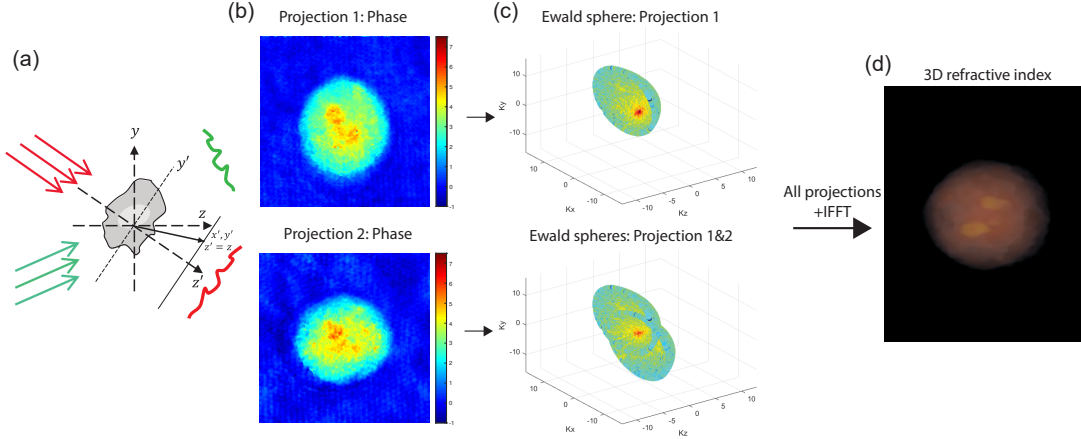


Figure 2.1: ODT using Fourier diffraction theorem for a biological cancer cell, MDA-MB-231. (a) Schematic of ODT. (b) 2D QPI Phase images for two projections were measured holographically with a wavelength of 633nm. (c) Filling the Fourier domain of the scattering potential using Ewald's spheres of the measured projections using Rytov approximation. (d) 3D rendering of the reconstructed refractive index distribution.

in which k_x , k_y , and k_z are the spatial frequencies satisfying $k_z = \sqrt{k_0^2 n_0^2 - k_x^2 - k_y^2}$. By putting Eq. 2.18 into Eq. 2.8 and taking a 2D Fourier transform from both sides, we can reach,

$$\frac{k_z}{2j\pi} e^{-jk_z z_0} \iint_{-\infty}^{\infty} U_s(x, y) e^{-j[k_x x + k_y y]} dx dy = \int_{\mathcal{D}'} V(r') e^{-j\vec{k} \cdot \vec{r}'} U_i(r') dr' \quad (2.19)$$

This equation relates the 2D Fourier transform of the scattered field projection to some spatial frequency components of the 3D Fourier transform of the scattering potential. For a plane wave illumination, $U_i(r) = e^{j\vec{k}^{in} \cdot \vec{r}}$, we will have,

$$\tilde{V}(k_x - k_x^{in}, k_y - k_y^{in}, k_z - k_z^{in}) = \frac{k_z e^{-jk_z z_0}}{2j\pi} \mathcal{F}_{2D}\{U_s\}(k_x, k_y) \quad (2.20)$$

Eq. 2.20 is known as Fourier Diffraction Theorem or Wolf's transform which was proposed by Emil Wolf in 1969 [13]. According to Eq. 2.20, the 2D Fourier transform of the complex scattered field which is measured at z_0 as the sample is illuminated with an angle defined by the illumination wave vector \vec{k}^{in} can be mapped on the surface of a hemisphere, referred to as the Ewald's sphere on the 3D Fourier domain of the scattering potential. The Ewald's sphere is centered at $-\vec{k}^{in}$ and satisfies the relation of $k_x^2 + k_y^2 + k_z^2 = (k_0 n_0)^2$. This process is shown in Fig. 1.1 for 2 illumination angles. Using the Fourier Diffraction Theorem, the 3D scattering potential can be found within the first-order Born approximation. One example is shown in the first row of Fig. 2.2. In this example, a digital phantom with the maximum refractive index contrast of $\delta n(r)_{\max} = 0.07$ is illuminated with 180 projections in a circular pattern with a maximum angle of $\theta = 35^\circ$, and the scattered fields are calculated using BPM. The synthetic projections are used for the Fourier diffraction theorem using first-order Born

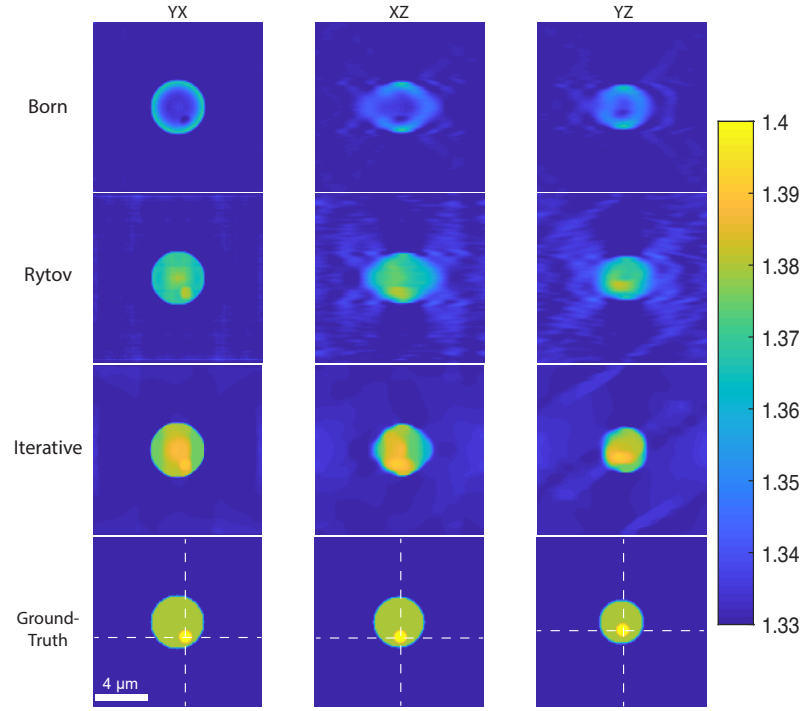


Figure 2.2: 3D ODT reconstruction for a digital phantom using different methods. The 3D refractive index reconstruction is shown in 3 different YX , XZ , and YZ planes indicated in the last row with dashed lines. Each row shows the ODT reconstruction using Born approximation, Rytov approximation, iterative reconstruction using TV regularize, and the ground-truth image, respectively.

approximation and we can compare the reconstruction with the ground truth in the last row. Due to the limited range of validity of Born approximation, the quality of ODT based on this approximation is compromised.

2.3.3 Fourier diffraction theorem using Rytov approximation

In 1981, Devaney presented the Fourier diffraction theorem based on the Rytov approximation [25]. In this regard, we define the complex phase, $\phi(r)$, of the total field as $U(r) = e^{\phi(r)}U_i(r)$ and put it in Eq. 2.4,

$$\begin{aligned}
 \nabla^2 [U_i(r)e^{\phi(r)}] + k_0^2 n_0^2(r)U_i(r)e^{\phi(r)} &= -4\pi V(r)U_i(r)e^{\phi(r)} \\
 \Rightarrow e^{\phi(r)}\nabla^2 U_i(r) + e^{\phi(r)}U_i(r) [\nabla^2 \phi(r) + (\nabla \phi)^2] \\
 + k_0^2 n_0^2 e^{\phi(r)}U_i(r) + 2e^{\phi(r)}\nabla \phi(r) \cdot \nabla U_i(r) \\
 = e^{\phi(r)}\nabla^2 [U_i(r)\phi(r)] + e^{\phi(r)}k_0^2 n_0^2 [U_i(r)\phi(r)] \\
 + e^{\phi(r)}U_i(r)\nabla \phi(r) \cdot \nabla \phi(r) &= -4\pi V(r)U_i(r)e^{\phi(r)} \quad (2.21)
 \end{aligned}$$

By clearing up Eq. 2.21 we can end up to,

$$\Rightarrow (\nabla^2 + k_0^2 n_0^2(r)) [U_i(r)\phi(r)] = -4\pi U_i(r)V(r) - U_i(r)\nabla\phi(r) \cdot \nabla\phi(r) \quad (2.22)$$

By reforming the wave equation to Eq. 2.22, we can use the Rytov approximation. According to the first-order Rytov approximation, we neglect the second term on the right side of Eq. 2.22. In another word, the first-order Rytov approximation assumes that the gradient of the phase, $\nabla\phi(r)$ is negligible with respect to the scattering potential, $V(r)$. Considering this approximation, we will have a similar form to Eq. 2.5 and can represent an integral solution to the optical scattering problem using Green's function,

$$U_i(r)\phi(r) = \int_{\mathcal{D}'} G(r, r') V(r') U_i(r') dr' \quad (2.23)$$

Eq. 2.23 is very similar to Eq. 2.8 which was achieved using the first-order Born approximation, with the only difference that we should use $U_i(r)\log[U(r)/U_i(r)]$ instead of the $U_s(r)$ on the left side of the equation. As a result, the Fourier diffraction theorem which was presented in Eq. 2.20 can be applied to have a 3D reconstruction of scattering potential. Therefore, we presented the Fourier diffraction theorem using the first-order Rytov approximation,

$$\tilde{V}(k_x - k_x^{in}, k_y - k_y^{in}, k_z - k_z^{in}) = \frac{k_z e^{-jk_z z_0}}{2j\pi} \mathcal{F}_{2D} \{U_i \log[U/U_i]\}(k_x, k_y) \quad (2.24)$$

ODT using the Fourier diffraction theorem based on the first-order Rytov approximation can present better reconstructions in comparison with Born approximation. For the example of the digital phantom with BPM-based synthetic projections, we reconstructed the 3D refractive index using the Fourier diffraction theorem based on the first-order Rytov approximation and it is shown in the second row of Fig. 2.2. In comparison with the ground truth refractive index distribution, we can see that the Rytov approximation provides a much more accurate reconstruction than the first-order Born approximation. A comparison of the Fourier diffraction theorem based on the Born and Rytov approximations and also the range of their validity is studied in [34].

2.3.4 Iterative approaches for ODT

The application of the Fourier diffraction theorem in ODT is hindered by two primary issues. Firstly, the forward scattering problem is linearized through either the Born or Rytov approximations in order to be invertible. Consequently, 3D ODT reconstructions will be inaccurate for objects with strong or multiple scattering. Secondly, the limited number of projections and/or the limited numerical aperture of the imaging optics restricts our access to all of the spatial frequencies of the 3D object. These missing spatial frequencies will cause inaccuracies or artifacts in the 3D ODT reconstruction such as underestimation of the refractive index or elongation along the optical axis [26], [38]. In order to solve these two issues iterative approaches for ODT were proposed. The basis of these iterative approaches is on using a

forward model for optical scattering, \mathcal{M} to calculate the projections and compare them with the measurements, and also on using priors about the 3D refractive index distribution. Accordingly, the 3D scattering potential can be found iteratively by minimization of an error function consisting of a data term and a prior regularization term,

$$\hat{V}(r) = \arg \min_V \left\{ \frac{1}{L} \sum_{l=1}^L \left\| \mathcal{M} \{V(r), U_i^l(r)\} - U^l \right\|_2^2 + \tau \mathcal{R}(V(r)) \right\} \quad (2.25)$$

where L is the number of projections, U^l is the measured total field for the illumination angle of l , $\mathcal{M} \{V(r), U_i^l(r)\}$ is the calculated projection for the illumination l for the current estimate of the scattering potential, τ is the regularizer parameter, and $\mathcal{R}(v(r))$ is the regularizer to be applied during the iterative solution based on the prior knowledge for the sample. Two examples of such priors can be non-negativity and smoothness of the sample which can be implemented with a Total-variation regularizer function [26]. What was presented in Eq. 2.25 is a general form for the iterative approaches for ODT. Different research studies presented iterative solutions for ODT based on different forms of the forward model \mathcal{M} . In [26], the forward model is a linear optical scattering based on the first-order Rytov approximation, Eq. 2.23. In [27], [36], the forward model is based on BPM which was presented in Eq. 2.16. I will also present an iterative solution for ODT based on a physics-informed neural network as the forward model \mathcal{M} in chapter 6.

We compared the improvement in 3D ODT reconstruction with the Fourier diffraction theorem by reconstructing our digital phantom iteratively using a linear forward model based on Eq. 2.23 and a Total-variation regularizer. The FISTA algorithm was employed for the iterative optimization, as outlined in [26], and it was found that the reconstructed refractive index was much closer to the ground truth than before. We can see the results in the third row of Fig. 2.2. Comparing the Rytov reconstruction and the iterative reconstruction reveals two improvements. Firstly, the elongation and underestimation of the reconstructed refractive index are drastically improved. Secondly, Total-variation regularization enabled a smoother result for the 3D refractive index.

2.4 Polarization of light and birefringence

The light which is propagating in a medium has several properties: amplitude or intensity, color or wavelength, phase, and polarization. As discussed in section 2.2, the electric and magnetic fields representing the light are vectors and the study of the polarization state of light will define what is the direction of these field vectors and how they are evolving over time and space. Based on Maxwell's equations, we know that $\nabla \cdot (\mu \vec{H}) = 0$, and $\nabla \cdot (\epsilon_r \vec{E}) = 0$. These two equations imply that a planar light that is propagating in a uniform medium should have the electric and magnetic fields perpendicular to the wave vector direction, $\vec{k} \cdot \vec{E} = \vec{k} \cdot \vec{H} = 0$. As a result, the polarization state of such a wave is in the plane perpendicular to the wave vector. We can define two arbitrary orthogonal vectors defining this transverse plane as \hat{u} , and

\hat{v} . Any arbitrary polarization state can be defined by decomposing the electric field in these two vectors,

$$\vec{E} = E_u e^{jk \cdot r} \hat{u} + E_v e^{j(k \cdot r + \varphi_{uv})} \hat{v} \quad (2.26)$$

Four different scenarios can be considered for the polarization state of light. If φ_{uv} is zero or $\pm 2m\pi$, the two orthogonal vectors will be *in phase* and the polarization of light is linear. If φ_{uv} is $\pm\pi/2 \pm 2m\pi$, and $E_u = E_v$, the light is circularly polarized. If $E_u \neq E_v$ or $\varphi_{uv} \neq m\pi/2$, the polarization state of the light is elliptical. The last scenario is an unpolarized light which consists of a randomly and rapidly varying succession of different polarization states. However, it should be mentioned that a perfectly monochromatic wave is always polarized since the time dependence of the wave is ωt and the relative phase φ_{uv} should be constant.

Once the polarization has been defined, we can study Maxwell's equations to observe how the polarization of light is changed in the scattering process and the light interaction with materials. In optical scattering from inhomogeneous scalars samples whose permittivity and refractive index are scalar distributions, the light propagation follows Eq. 2.3. The depolarization term $2\nabla [E(r, \omega) \cdot \nabla \ln(n(r))]$ on the right side of this equation will couple different components of the field vector and leads to the polarization change as the light is propagating in an inhomogeneous media in which $\nabla n(r) \neq 0$. Another way to consider depolarization is that in the light scattering process, the scattered light can be decomposed into different plane waves in the Fourier domain [39], and the polarization vector of each of them should be perpendicular to its \vec{k} vector. As a result, the scattered field with multiple spatial frequencies cannot preserve the polarization state of the illumination beam. In other words, the depolarization term in Eq. 2.3 will guarantee that the divergence of the electric displacement field is zero.

Another way leading to polarization coupling and polarization sensitivity in the interaction of light with the sample is the *anisotropy* or *birefringence* of the sample. In some structures, the speed of the light, and as a result, the refractive index and the permittivity depend on the polarization state of the electric field, and should be represented with a tensor in Eq. 2.2. The refractive index tensor of an inhomogeneous sample in an arbitrary coordinate is,

$$\bar{\bar{n}}(r) = \begin{pmatrix} n_{xx}(r) & n_{xy}(r) & n_{xz}(r) \\ n_{yx}(r) & n_{yy}(r) & n_{yz}(r) \\ n_{zx}(r) & n_{zy}(r) & n_{zz}(r) \end{pmatrix} \quad (2.27)$$

For homogeneous crystals, the refractive index tensor does not vary spatially and can be diagonalized using a spatially-invariant unitary matrix $\bar{\bar{n}} = \bar{\bar{C}}^{-1} \bar{\bar{n}}_D \bar{\bar{C}}$. The $\bar{\bar{C}}$ matrix defines the crystalline orientation and the diagonal $\bar{\bar{n}}_D$ matrix has the refractive index values of the sample for each eigen polarization state. The crystalline orientation provides important information about the molecular structure of the material [40]. However, for an inhomogeneous sample, the crystalline coordinate can also vary spatially and there is not a universal $\bar{\bar{C}}$ matrix that diagonalizes the refractive index tensor.

To describe the polarization of light and its alteration when passing through a polarization-sensitive structure, two mathematical frameworks are available: the Stokes–Mueller formalism and the Jones formalism [41]. In these formalisms, the polarization state of the light is described with a vector and the system is defined with a matrix that maps the polarization vector before the structure to the polarization vector after the structure. In the Stokes–Mueller formalism, the polarization state of the light is described with a 4×1 Stokes vector, S , whose components show the total intensity of light, the intensity of the linearly polarized light, the intensity of the $\pm 45^\circ$ polarized light, and the intensity of the circularly polarized light, respectively. A 4×4 Mueller matrix of a sample, M , will map the input Stokes vector to the output Stokes vector, $S^{out} = MS^{in}$. The Mueller matrix is a real-valued matrix and is particularly of interest for incoherent or unpolarized light where the phase of the light cannot be measured. Alternatively, Jones formalism can be used for the examples that the phase of the light is important. Jones formalism is based on the complex Jones vector which represents the electric field vector. This Jones vector is,

$$\vec{E} = \begin{pmatrix} E_x \\ E_y \\ E_z \end{pmatrix}, \quad \vec{E}^{out} = \vec{J} \vec{E}^{in} \quad (2.28)$$

and the polarization-sensitive media is defined with the Jones matrix \vec{J} . The elements of the Jones vectors and Jones matrix are complex and include phase information. It is important to note that Jones vectors and Jones matrices can be a function of the spatial coordinate, r , for inhomogeneous samples. For homogeneous samples, the polarization vector is perpendicular to the propagation direction and only two components are needed to describe it, which is why Jones vectors are traditionally represented with only two components [40]. However, when studying the polarization of light in inhomogeneous anisotropic media, three components are required to describe the Jones formalism.

The 2D QPI images acquired by illuminating the sample with a plane wave can be generalized to anisotropic samples using Jones formalism. This mathematical framework allows us to represent each component of the Jones matrix with a 2D complex QPI, and measure the birefringent inhomogeneous sample using a polarization-sensitive off-axis holography setup. As a result, we can extrapolate QPI and holography to anisotropic samples, which is the main focus of chapter 3 in our study of polarization-sensitive ODT.

2.5 Optical nonlinearity

I discussed the interaction of light with the sample based on Maxwell's equations in Eq. 2.1. For high intensities of light and strong fields, the constitutive equation, defining the relationship of the polarizability of the medium, $P(r, t)$ with the electric field, $E(r, t)$ is not linear anymore. In this case, in addition to the linear permittivity, ϵ_r , nonlinear and higher order susceptibilities

are required to write the electric field constitutive equation,

$$P(r, t) = \epsilon_0 (\epsilon_r - 1) E(r, t) + \epsilon_0 \chi^{(2)} E^2(r, t) + \epsilon_0 \chi^{(3)} E^3(r, t) + \dots \quad (2.29)$$

where $\chi^{(2)}$, and $\chi^{(3)}$ are the second-order and third-order nonlinear susceptibilities. The nonlinear interaction of light with such materials can introduce interesting phenomena such as harmonic generation, frequency mixing, self-phase modulation, and self-focusing [30].

At the molecular level, the nonlinear polarizability can be explained by extending the Lorentz model for the atoms to anharmonic oscillators [30]. The origin of nonlinearity in this classical model is the form of the restoring force exerted on the electrons. In the Lorentz model, the restoring force is linear with respect to the coordinate of the electron, and as a result, the atom can be modeled as a harmonic oscillator. However, if the potential energy function of the medium is not parabolic, the restoring force can be written in the form of a Taylor series with nonlinear coefficients of the electron coordinate.

There are several important properties of nonlinear susceptibilities. A very important property is the vanishing of the second-order susceptibility, $\chi^{(2)}$, for centrosymmetric materials. For a centrosymmetric material, we have the same structure if we flip the coordinate system around the symmetry plane. In this case, if we have the electric field of E and polarizability of P in the initial coordinate system, we will have the electric field and polarizability of $-E$ and $-P$ in the flipped coordinate system. Additionally, the $\chi^{(2)}$ remains unchanged as the structure is symmetric. Therefore, we will have $P = \epsilon_0 \chi^{(2)} E^2$ in the initial coordinate system and $-P = \epsilon_0 \chi^{(2)} (-E)^2$ for the flipped coordinate systems. These two equations imply that $\chi^{(2)} = -\chi^{(2)}$ which is possible if and only if $\chi^{(2)} = 0$. Most of the materials are centrosymmetric and the vanishing of the second-order susceptibility in these materials is a very useful property for background-free microscopy. Based on this property, if an inhomogeneous sample is illuminated with a high-intensity coherent light, only non-centrosymmetric features will generate second-order phenomena and can be easily distinguished from the rest of the sample. Another important property of the nonlinear susceptibilities is Miler's rule [42] which can provide an estimate of the order of magnitude of the nonlinear susceptibilities. According to Miler's rule, the order of magnitude of the nonlinear susceptibility is proportional to the nonlinear susceptibility of the lower order with a coefficient known as Miller's coefficient. As a result, the nonlinear susceptibilities get orders of magnitude weaker as the order increases. Respectively, higher optical intensity is required to achieve higher-order nonlinear phenomena.

We can study the second-order nonlinear polarizability in the presence of a monochromatic field. For the sake of simplicity, we first consider a scalar formalism and a single polarized input light,

$$P^{(2)} = \epsilon_0 \chi^{(2)} (E(t))^2 = \epsilon_0 \chi^{(2)} \left(E e^{j\omega t} + \text{c.c.} \right)^2 = \epsilon_0 \chi^{(2)} |E|^2 + \epsilon_0 \chi^{(2)} \left(E^2 e^{2j\omega t} + \text{c.c.} \right) \quad (2.30)$$

The c.c. is the complex conjugate term. Eq. 2.30 shows that by illuminating a second-order nonlinear medium we can generate a D.C. polarizability, $\epsilon_0 \chi^{(2)} |E|^2$, which is responsible for

a phenomenon known as optical rectification, and polarizability at the double frequency, 2ω which is responsible for the generation of light at double frequency, known as second-harmonic generation (SHG). SHG and utilizing it for ODT is the main topic of chapter 4. If we illuminate the second-order material with two beams at frequencies ω_1 and ω_2 , we can even generate more frequencies,

$$P^{(2)} = \epsilon_0 \chi^{(2)} (E_1(t) + E_2(t))^2 = \epsilon_0 \chi^{(2)} \left(E_1 e^{j\omega_1 t} + E_2 e^{j\omega_2 t} + \text{c.c.} \right)^2 = \epsilon_0 \chi^{(2)} \left(|E_1|^2 + |E_2|^2 + E_1^2 e^{2j\omega_1 t} + E_2^2 e^{2j\omega_2 t} + 2E_1 E_2 e^{j(\omega_1 + \omega_2)t} + 2E_1 E_2^* e^{j(\omega_1 - \omega_2)t} + \text{c.c.} \right) \quad (2.31)$$

in which E_1 and E_2 are the amplitudes of two beams at frequencies ω_1 and ω_2 , respectively. Eq. 2.31 shows that illuminating the second-order nonlinear medium with two frequencies can generate nonlinear polarizability at $P(2\omega_1)$, and $P(2\omega_2)$ as harmonic generations, $P(\omega_1 + \omega_2)$ as sum frequency generation, and $P(\omega_1 - \omega_2)$ as difference frequency generation. If we consider a third-order nonlinear medium, we can generate third-order polarizabilities at triple frequencies, known as third-harmonic generation (THG), and four-wave mixing phenomena.

After introducing the nonlinear polarizability, we can discuss the optical wave propagation in nonlinear media using the nonlinear Helmholtz equation. In Eq. 2.1 we have the general form of the space- and time-varying wave equation in the presence of the electric polarizability, $P(r, t)$. We showed that if we assume a non-centrosymmetric second-order media (neglecting the higher-order terms) is illuminated with a monochromatic wave at frequency ω , optical rectification, and SHG can be achieved. As a result, we should be able to write the electric field in such a media as $E(r, t) = E_0(r) + E_F(r)e^{j\omega t} + E_{SH}(r)e^{2j\omega t} + \text{c.c.}$ with $E_0(r)$ showing D.C. field, E_F showing the field at the fundamental frequency ω , and E_{SH} showing the field at the SH frequency, 2ω . As a result, we can write Eq. 2.1 in the frequency domain at two fundamental and SH frequencies,

$$\begin{aligned} \nabla \times \nabla \times E_F(r, \omega) - \frac{\omega^2}{c^2} E_F(r, \omega) &= + \frac{\omega^2}{c^2} \chi^{(1)}(r) E_F(r, \omega) + \frac{2\omega^2}{c^2} \chi^{(2)}(r) E_F^*(r, \omega) E_{SH}(r, 2\omega) \\ \nabla \times \nabla \times E_{SH}(r, 2\omega) - \frac{4\omega^2}{c^2} E_{SH}(r, 2\omega) &= + \frac{4\omega^2}{c^2} \chi^{(1)}(r) E_{SH}(r, 2\omega) + \frac{4\omega^2}{c^2} \chi^{(2)}(r) E_F^2(r, \omega) \end{aligned} \quad (2.32)$$

Eq. 2.32 presents the wave propagation in second-order media considering monochromatic fundamental and SH waves. This equation is the second-order Helmholtz equation including two coupled equations governing the propagation of $E_F(r, \omega)$ and $E_{SH}(r, 2\omega)$ that can be solved using a numerical technique such as finite element method (FEM), or BPM. Providing solutions for a set of coupled equations can simply get complicated. A simple approximation to decouple the equations of Eq. 2.32 is based on neglecting the depletion of the fundamental field, $E_F(r, \omega)$. This approximation is valid when $|E_{SH}| \ll |E_F|$ and we can neglect the last term of the right side of the Helmholtz equation governing the propagation of the fundamental

field, i.e. $\frac{2\omega^2}{c^2} \chi^{(2)}(r) E_F^*(r, \omega) E_{SH}(r, 2\omega)$. In fact, this is a valid approximation in most of the cases as $\chi^{(2)}$ of the materials is very small and the SH field is orders of magnitude smaller than the fundamental field. Using the undepleted fundamental approximation and also neglecting the depolarization term we can write,

$$\begin{aligned} \nabla^2 E_F(r, \omega) + k_0^2 n^2(r, \omega) E_F(r, \omega) &= 0 \\ \nabla^2 E_{SH}(r, 2\omega) + 4k_0^2 n^2(r, 2\omega) E_{SH}(r, 2\omega) &= -4k_0^2 \chi^{(2)}(r) E_F^2(r, \omega) \end{aligned} \quad (2.33)$$

where k_0 is the free-space wave number at the fundamental frequency. Eqs. 2.33 solve the SH generation and scattering from an inhomogeneous $\chi^{(2)}$ material. Undepleted pump approximation easily decoupled two equations from each other. In this regard, first, the Helmholtz equation for the fundamental field, $E_F(r, \omega)$, can be solved and when the fundamental field is known, it can be replaced in the second equation to find the SH field, $E_{SH}(r, 2\omega)$.

Eqs. 2.33 present the SH generation and scattering in a scalar formalism. In reality, all of the second-order materials are anisotropic and their $\chi^{(2)}$ can not be represented with a scalar distribution. We mentioned in section 2.3 that the general form for the linear refractive index tensor of anisotropic materials is a 3×3 matrices. For the second-order susceptibility, a higher rank tensor is required as two fields are contributed to the second-order polarizability. For SHG, we can rewrite Eq. 2.30 for anisotropic materials as,

$$P_i(r, 2\omega) = \epsilon_0 \sum_j \sum_k \chi_{ijk}^{(2)}(r) E_j(r, \omega) E_k(r, \omega) \quad (2.34)$$

where $i, j, k \in \{x, y, z\}$ are indices corresponding to each element of the field and polarizability vectors. Eq. 2.34 shows the polarizability for the SH process. Considering Kleinman's symmetry condition applies that $\chi_{ijk}^{(2)} = \chi_{ikj}^{(2)}$ if $j \neq k$. This symmetry helps to have a contracted notation to represent $\chi^{(2)}$ with a 3×6 matrix,

$$\begin{pmatrix} P_x(2\omega) \\ P_y(2\omega) \\ P_z(2\omega) \end{pmatrix} = \epsilon_0 \begin{pmatrix} \chi_{11}^{(2)} & \chi_{12}^{(2)} & \chi_{13}^{(2)} & \chi_{14}^{(2)} & \chi_{15}^{(2)} & \chi_{16}^{(2)} \\ \chi_{21}^{(2)} & \chi_{22}^{(2)} & \chi_{23}^{(2)} & \chi_{24}^{(2)} & \chi_{25}^{(2)} & \chi_{26}^{(2)} \\ \chi_{31}^{(2)} & \chi_{32}^{(2)} & \chi_{33}^{(2)} & \chi_{34}^{(2)} & \chi_{35}^{(2)} & \chi_{36}^{(2)} \end{pmatrix} \begin{pmatrix} E_x(\omega)^2 \\ E_y(\omega)^2 \\ E_z(\omega)^2 \\ 2E_y(\omega)E_z(\omega) \\ 2E_x(\omega)E_z(\omega) \\ 2E_x(\omega)E_y(\omega) \end{pmatrix} \quad (2.35)$$

Eq. 2.35 is the general form for the nonlinear polarizability in the SHG process which shows that there are 18 elements in the $\chi^{(2)}$ tensor contributed to the SHG. The 18 elements of the second-order susceptibility tensor can be reduced in the presence of spatial symmetry in the material's crystalline structure. Eq. 2.35 is written in an arbitrary coordinate system. However, many of the elements of the $\chi^{(2)}$ tensor can be zero in a special crystalline coordinate system thanks to the spatial symmetries. The study of the symmetry groups in crystals and their effect on the nonlinear optical susceptibility tensor was an important research topic in the earliest days of nonlinear optics as it can provide useful information on an efficient

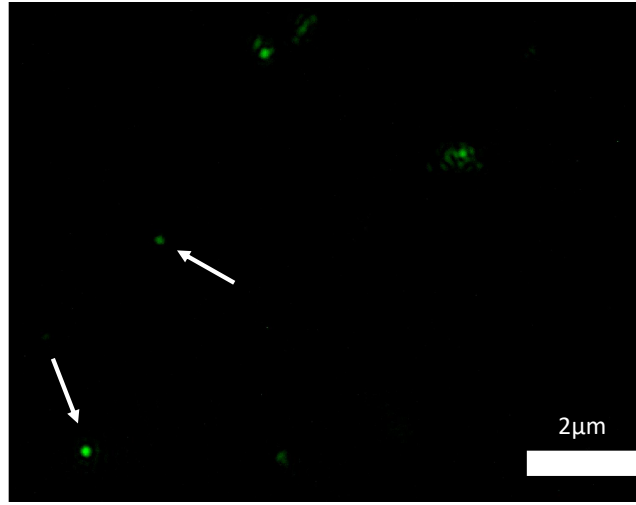


Figure 2.3: Wide-field SH generation from Barium Titanate nano-particles illuminated with a polarized 280 femtosecond light source.

nonlinear frequency conversion process [43]. For example, Barium Titanate, BaTiO_3 , which is a Tetragonal crystal with the point group of $4mm$ has a second-order susceptibility tensor in the form of,

$$\epsilon_0 \bar{\chi}^{(2)} = \begin{pmatrix} 0 & 0 & 0 & 0 & d_{15} & 0 \\ 0 & 0 & 0 & d_{15} & 0 & 0 \\ d_{31} & d_{31} & d_{33} & 0 & 0 & 0 \end{pmatrix} \quad (2.36)$$

The spatial symmetry information about the second-order susceptibility tensor provides useful prior knowledge in order to efficiently generate SH, and also for SH imaging applications. We wrote the nonlinear polarizability in Eq. 2.35 for the SHG process. Third-order nonlinear processes should be described in a general form with a fourth-rank tensor $\chi_{ijkl}^{(3)}$ as there are 4 waves participating in the nonlinear process. Consequently, if more waves are included in the process, more components of the nonlinear susceptibility tensor will be affected by spatial symmetries, potentially causing some of them to become zero.

Fig. 2.3 represents the wide-field SH emission of Barium Titanate nano-particles with a diameter of 200nm. The imaging system is based on the experimental setup presented in chapter 4 where the particles are imaged with a 0.85-numerical aperture objective and the fundamental beam is filtered with a series of three filters providing an optical density of 19 at the fundamental wavelength, 1030nm. The illumination beam and the detection signal are X-polarized, and as it is clear from the particles indicated with arrows, the SH signal can change depending on the crystalline orientation of the nano-particles.

In summary, we presented a general theoretical background on nonlinear optical processes such as SHG and how the nonlinear susceptibility tensor of the material contributes to these

processes. We specifically discussed the SHG, the second-order polarizability $\chi^{(2)}$ tensor for SHG, and wave propagation and the Helmholtz equation for this process. SHG can be used as a background-free process for ODT. The idea of SH-ODT is to collect complex SHG fields as the sample is illuminated with different angles and reconstruct the 3D $\chi^{(2)}$ distribution. This can be achieved by inversion of Eqs. 2.33 and will be discussed in detail in chapter 4.

3 Polarization-sensitive ODT

This work has been published in the following paper:

- A. Saba, J. Lim, AB. Ayoub, EE. Antoine, and D. Psaltis (2021). "Polarization-sensitive optical diffraction tomography". *Optica*, 8(3), 402-408.

A. Saba carried out the theory of polarization-sensitive ODT, algorithm implementation, BPM simulations, building experimental setup, and getting numerical and experimental results.

3.1 Introduction

Polarization microscopy [44] is an imaging technique that exploits the birefringence contrast of the samples and has been extensively used in the pathology and diagnosis of some diseases, such as squamous cell carcinoma [45]. Over the course of many years, there has been extensive research and development in this microscopy [46]. Polarization microscopy modality has been applied to the study of a variety of biological samples containing fibrous structures, such as collagen, muscle tissue, tendon, retina nerve, fibroblast, and starch, where birefringence can be observed. Nonlinear microscopy methods such as CARS [47] and second harmonic microscopy [48] have also been studied from the polarization-sensitive viewpoint.

Several studies have explored polarization-sensitive holography for birefringent samples in the context of quantitative two-dimensional (2D) polarization imaging [49]–[54]. The Oldenbourg group has developed the LC-polariscope method [55], [56] presenting 2D images of birefringence distribution. Regarding 3D imaging techniques, polarization-sensitive optical coherence tomography has been thoroughly investigated for imaging birefringent samples [57]–[59]. Confocal fluorescence polarization microscopy has also been reported [60] and the LC-polariscope has been used together with a multi-focus grating to provide 2D birefringence images in different focal planes [61]. Despite the variety of existing methods for polarization microscopy, none of them provide a quantitative reconstruction of birefringence in 3D. As of now, a quantitative, label-free, and three-dimensional imaging method for polarization

microscopy has yet to be developed.

Optical diffraction tomography (ODT), on the other hand, is a quantitative, label-free, and 3D imaging method which reconstructs the distribution of the refractive index (RI) values of a sample using multiple-angle-measured scattered fields [13]. Previous studies on ODT reconstruction have been constrained by the scalar Helmholtz equation, which limits its application to isotropic samples. While the scalar refractive index (RI) distribution provides significant morphological and biological insights into a sample, it fails to capture the RI tensor for birefringent samples. To address this limitation, this chapter investigates polarization-sensitive ODT techniques for birefringent samples and their ability to reconstruct the 3D distribution of the RI tensor. The Jones formalism [62] is used throughout this chapter. The Jones matrix of the sample has been measured holographically for multiple illumination angles. We then derive the tensorized version of Wolf's method and use it for direct tomographic reconstructions. Synthetic data are generated using the vectorial beam propagation method (V-BPM) and they are used to guide the experiments in polarization-sensitive ODT. Lastly, we will explore a 3D polarization-based contrast metric that will be presented as a map of the sample highlighting its inherent birefringence distribution.

3.2 Methodology

3.2.1 Theory

Fig. 3.1 highlights the importance of considering polarization for ODT. We applied conventional ODT reconstruction using the Rytov approximation for a corn starch granule which is a birefringent sample [63]. In two experiments, the illumination beam had $+45^\circ$ and -45° linear polarization states with respect to the X-axis in the XY coordinate. We measured the X-polarized light of the scattered light using a conical scan at 180 equally spaced illumination angles with a 30° angle with respect to the Z-axis. In Fig. 3.1(a-c), we show the YX profiles of the 3D reconstructions for the two different illumination cases ($+45^\circ$ and -45° linear polarizations) followed by the difference between them. This figure clearly demonstrates the importance of considering polarization in ODT. The Y components of the two incident polarizations are both coupled to the measured X polarization only for an anisotropic sample such as the corn kernel used in this experiment. The opposite sign of the Y components in the incident light are responsible for the difference between the reconstructions in Fig. 3.1 (a) and (b). On the other hand, when the sample is isotropic, there is no light coupling between the X and Y polarizations. As a result, independently of the sign of the Y-polarized light in the $+45^\circ$ and -45° states, the reconstructions will be same. This has been shown in Fig. 3.1(d-f) for a $4.5\mu\text{m}$ diameter polystyrene bead which is immersed in silicon oil.

The Jones vectors and Jones matrix can be used to illustrate the connection between the input and output field vectors, $\vec{E}^{out} = \vec{J}\vec{E}^{in}$, in which \vec{E}^{out} and \vec{E}^{in} are the fields after and before the sample (Jones vectors) and the linear transformation between two vectors is represented

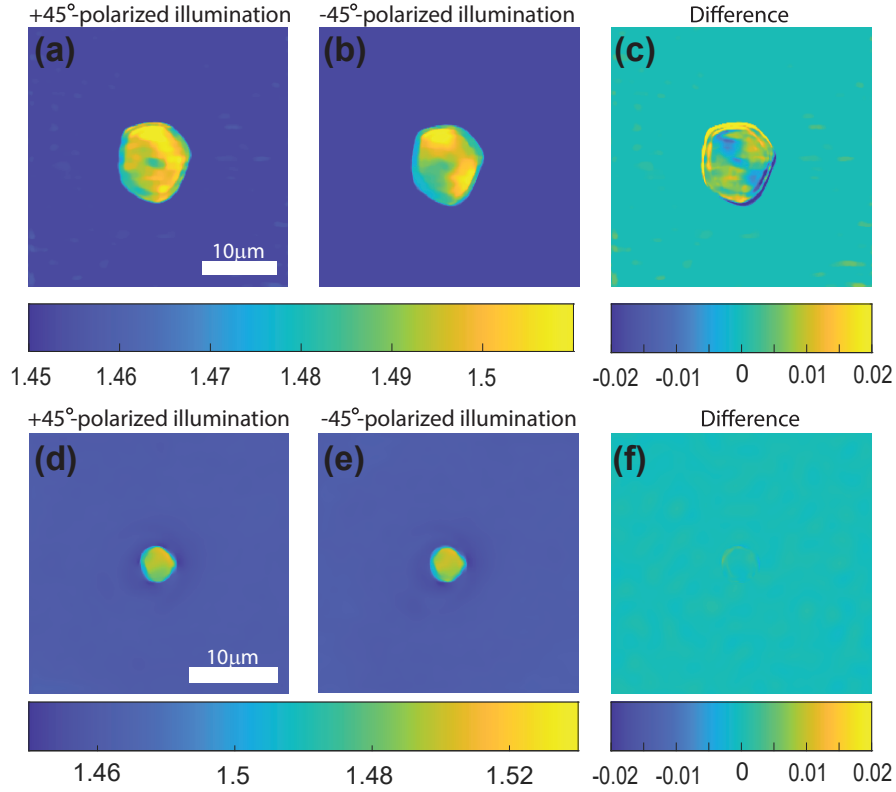


Figure 3.1: YX profiles of the conventional Rytov ODT reconstructions. On the top, we have the reconstruction of the corn starch kernel and multiple scattered fields were measured in the X-polarization when the illumination beam was (a) $+45^\circ$, and (b) -45° -polarized. (c) The difference between the two reconstructions of corn starch. Then, we have the reconstruction for an isotropic polystyrene bead when the illumination beam was (d) $+45^\circ$, and (e) -45° -polarized. (f) The difference between the two reconstructions of the polystyrene bead. All the colorbars show the refractive index and are unitless.

by the Jones matrix, \bar{J} . The Jones formalism represents a relationship between the complex fields and its components are also complex values. As a result, holography or iterative phase retrieval methods are necessary to reconstruct the complex scattered fields.

We formulate the vectorized version of the Helmholtz equation to investigate how light interacts with the sample. Additionally, we introduce the "scattering potential tensor" as a quantity that extends the scalar scattering potential and serves as a contrast metric for creating the 3D image of the birefringent sample. The integral solution of the vectorial Helmholtz equation can be obtained under the Born approximation (see section 1 of Appendix A). We consider a case that the sample is illuminated with the illumination beam vector \vec{E}^{illum} and consider the corresponding holographically recorded scattered field vector \vec{E}^s ,

$$\vec{E}^s(r) = \int \bar{G}(r, r') \times \bar{V}(r') \times \vec{E}^{illum}(r') d^3 r' \quad (3.1)$$

where $\bar{\bar{G}}$ is the Green's function (tensor) and $\bar{\bar{V}} = n_0 k_0^2 \delta \bar{\bar{n}} / 2\pi$ is the scattering potential (tensor) which is defined in terms of the quantity $\delta \bar{\bar{n}}$ which we refer to as the RI tensor. The RI tensor is defined in Appendix A and it is discussed further in section 3. Since the sample is assumed to be immersed in a liquid, the background is isotropic and homogeneous. Therefore, Green's function is a diagonal tensor, with the diagonal elements of the scalar case.

The RI tensor, and correspondingly the scattering potential tensor, and Jones matrix, are, in general, 3×3 tensors. As a result, we need three independent polarization states for $\bar{\bar{E}}^{illum}$ to reconstruct the full 3×3 Jones matrix for each projection. However, since the polarization state of the incident light is perpendicular to its wave vector, we can only have two independent polarization states for each illumination angle. Therefore, we calculate the scattering potential using 2×2 tensors by neglecting the Z component. The validity of this approximation and the resulting error is discussed in subsection 3.2.2.

Now, each element of the scattering potential tensor can be calculated with Wolf's method, considering that $E^{illum}(r') = \bar{\bar{E}}^{illum} \times e^{j\vec{k}^{in} \cdot r'}$:

$$\bar{\bar{V}}(k_x - k_x^{in}, k_y - k_y^{in}, k_z - k_z^{in}) = \frac{k_z}{2\pi j} \mathcal{F}_{2D} \left\{ \begin{pmatrix} E_{x1}^s & E_{x2}^s \\ E_{y1}^s & E_{y2}^s \end{pmatrix} \begin{pmatrix} \bar{\bar{E}}_{x1}^{illum} & \bar{\bar{E}}_{x2}^{illum} \\ \bar{\bar{E}}_{y1}^{illum} & \bar{\bar{E}}_{y2}^{illum} \end{pmatrix}^{-1} \right\} (k_x, k_y) \quad (3.2)$$

Eq. 3.2 is derived in Appendix A. After taking the 2D Fourier transform from the scattered fields, we shift them in the Fourier domain based on \vec{k}^{in} , and then fill the Fourier domain of the scattering potential by adding the spectra for all the incident angles. At the end, we take the inverse 3D Fourier transform to reconstruct the scattering potential tensor in the spatial domain. All of these operators are linear and can be considered equivalent to the Wolf transform [13] operating on each of 4 elements of the tensor independently using the Born approximation (see also section 1 of Appendix A). Alternatively, the Rytov approximation can be used, where we consider $\bar{\bar{E}}^t$ as $\overline{[e^\varphi]} \times \bar{\bar{E}}^{illum}$. In this case, we will have,

$$\begin{pmatrix} E_{xx}^s & E_{xy}^s \\ E_{yx}^s & E_{yy}^s \end{pmatrix} = \overline{[e^\varphi]} - \mathbb{1} \times \begin{pmatrix} E_{x1}^{illum} & E_{x2}^{illum} \\ E_{y1}^{illum} & E_{y2}^{illum} \end{pmatrix} \quad (3.3)$$

which leads to

$$\bar{\bar{\varphi}} = \text{logm} \left(\mathbb{1} + \begin{pmatrix} E_{x1}^s & E_{x2}^s \\ E_{y1}^s & E_{y2}^s \end{pmatrix} \begin{pmatrix} E_{x1}^{illum} & E_{x2}^{illum} \\ E_{y1}^{illum} & E_{y2}^{illum} \end{pmatrix}^{-1} \right) \quad (3.4)$$

logm is the matrix logarithm and $\bar{\bar{\varphi}}$ is the complex phase tensor which its imaginary part should be unwrapped [64]. Same as the scalar case, Rytov approximation is based on the first order Taylor expansion, where $\bar{\bar{E}}^s / \bar{\bar{E}}^{illum} \approx \text{logm} \left(\mathbb{1} + \bar{\bar{E}}^s / \bar{\bar{E}}^{illum} \right)$. The reconstructed scattering potential $\bar{\bar{V}}$ can be found by applying the Wolf transform, separately on each of the components of $\bar{\bar{\varphi}} e^{j\vec{k}^{in} \cdot r}$.

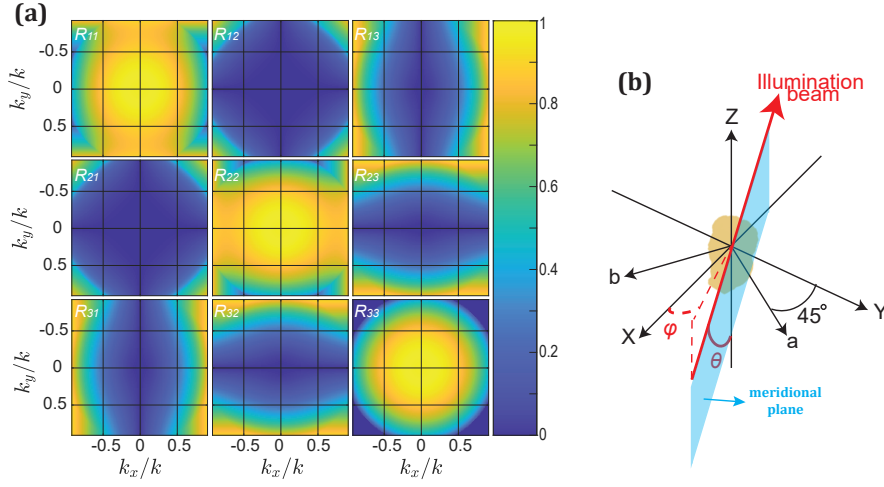


Figure 3.2: (a) Rotational Matrix described in Eq. 3.5, for polarization conversion of an oblique illumination. (b) Definition of the coordinate system.

The formulation described above is based on the scattered E^s and illumination E^{illum} fields immediately before and after the sample. However, in ODT, we illuminate the sample with different projections, from different angles (experimentally implemented using a galvomirror, as explained in the next subsection). As a result, with fixed input polarization of light in a fixed coordinate frame (here, XYZ experiment coordinates) changing the illumination angle changes the polarization of the illumination field. In this situation, by tilting the beam, the polarization of light will remain unchanged in the meridional plane (the plane containing the ray, and the optical axis, here z), and can be expressed in the XYZ Cartesian coordinate, using a rotational matrix [65]:

$$\begin{pmatrix} E_x^{illum} \\ E_y^{illum} \\ E_z^{illum} \end{pmatrix} = \overline{\overline{R}} \times \begin{pmatrix} E_x^{in} \\ E_y^{in} \\ E_z^{in} \end{pmatrix} \quad (3.5a)$$

$$\overline{\overline{R}} = \begin{pmatrix} \sin^2 \phi (1 - \cos \theta) + \cos \theta & -\sin \phi \cos \phi (1 - \cos \theta) & \cos \phi \sin \theta \\ -\sin \phi \cos \phi (1 - \cos \theta) & \cos^2 \phi (1 - \cos \theta) + \cos \theta & \sin \phi \sin \theta \\ -\cos \phi \sin \theta & -\sin \phi \sin \theta & \cos \theta \end{pmatrix} \quad (3.5b)$$

The parameters, θ , and ϕ are indicated in Fig. 3.2(b). The absolute value of the 9 components of the rotational matrix is shown in Fig. 3.2(a). The same matrix maps the complex measured fields to the complex scattered field, right after the sample, to compensate for the angular demagnification in the 4F system from the sample to CCD, including the water-dipping objective and the lens L4,

$$\vec{E}^s = \overline{\overline{R}} \times \vec{E}^m \quad (3.6)$$

Here, \vec{E}^m is the field vector, whose last component is always zero, as the perpendicular component to the camera cannot be measured. There are other contributions to the polarization change of the light, such as light refraction in the air-glass, and glass-water interface, and also oblique illumination to the polarizer. These are discussed in Appendix A.

In Eq. 3.2 and Eq. 3.4, we are working with the cross-polarized light, E_{yx}^s/E_x^{illum} . We have zero intensity values in these terms when there is no scattering and/or birefringence, which leads to random background phase values. As an example, the phase of this cross-polarized term is shown in Appendix A (Fig. A10) for one illumination angle. The random background phase values make the unwrapping and calibration challenging. To overcome this issue we can note the fact that Eq. 3.1 is linear with respect to \vec{E}^{illum} . As a result, we can get scattered fields in XY coordinate, if we illuminate with any pair of perpendicular polarization states, such as 45 degrees ab coordinate system as shown in Fig. 3.2(b). This way, when the input and output polarization states are not aligned, we don't have the intensity singularity problem. For instance, we present the phase of E_{xa}^s in section 6 of Appendix A in comparison with the phase of cross-polarized light (Fig. A10). On this subject, based on the linearity of Eq. 3.1, 3D reconstructions can be performed using E_{xa}^s , E_{xb}^s , E_{ya}^s , and E_{yb}^s , and then converted to the XY RI tensor using the procedure discussed in subsection 3.2.3.

3.2.2 Approximation of the 3×3 scattering potential tensor with a 2×2 tensor

As discussed in section A.1, the refractive index and the scattering potential tensor are 3×3 tensors in the general case. However, considering Eq. A.8, we need *three* independent illumination polarization states to make the illumination field tensor an invertible matrix. We can explain this issue using Jones formalism, in which the Jones matrix of the sample for each illumination angle can be defined as $\vec{E}^t = \vec{E}^s + \vec{E}^{illum} = \bar{J} \vec{E}^{illum}$. We can rewrite Eq. A.9 using Jones formalism as,

$$\left(\bar{J}_{3 \times 3}(r) - \mathbb{1}_{3 \times 3} \right) e^{j\vec{k}_i \cdot r} = \left[\int \bar{G}(r, r') \times \bar{V}(r') e^{j\vec{k}_i \cdot r'} d^3 r' \right] \quad (3.7)$$

Reconstruction of full 3×3 scattering potential tensor is possible using the Fourier diffraction theorem (similar to Eq. A.12), if we had the full 3×3 Jones matrix for each illumination angle. However, retrieval of such a Jones matrix is not feasible with 3×2 field tensors that we have in Eq. A.8.

In this regard we substitute the 3×3 Jones matrix and scattering potential tensor in Eq. 3.7 with 2×2 tensors and discuss the justification and validity range of this approximation. Using the Jones formalism, we can write the following matrix representation,

$$\begin{pmatrix} E_{x1}^{out} & E_{x2}^{out} \\ E_{y1}^{out} & E_{y2}^{out} \\ E_{z1}^{out} & E_{z2}^{out} \end{pmatrix} = \begin{pmatrix} J_{xx} & J_{xy} & J_{xz} \\ J_{yx} & J_{yy} & J_{yz} \\ J_{zx} & J_{zy} & J_{zz} \end{pmatrix} \begin{pmatrix} E_{x1}^{illum} & E_{x2}^{illum} \\ E_{y1}^{illum} & E_{y2}^{illum} \\ E_{z1}^{illum} & E_{z2}^{illum} \end{pmatrix} \quad (3.8)$$

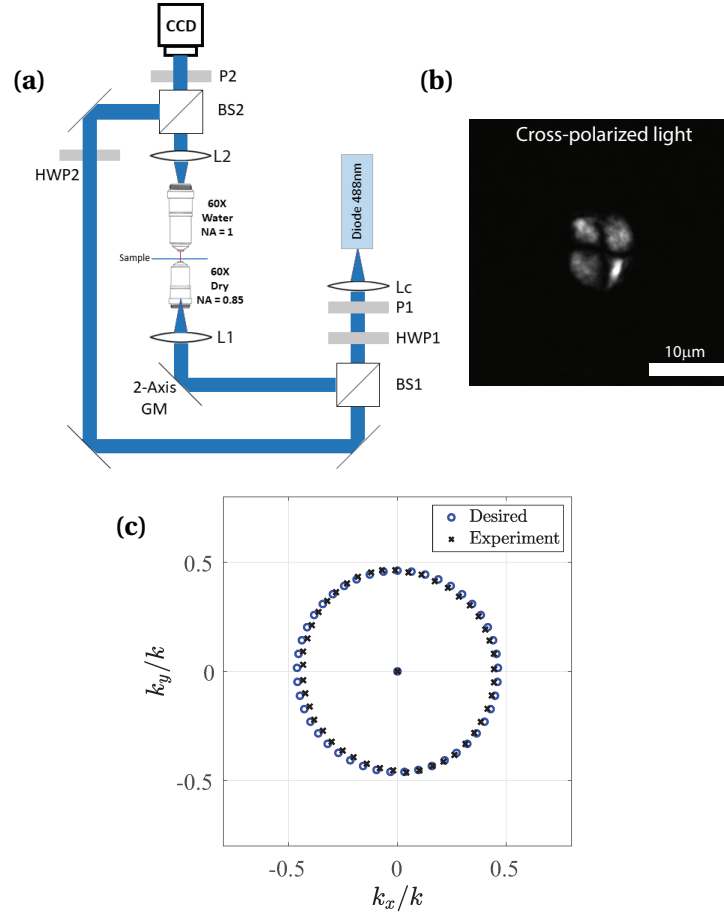


Figure 3.3: (a) Schematic of the polarization-sensitive holography setup has been used to get vectorial scattered fields for different illumination angles. (b) Cross-polarized light can be measured from a corn starch granule when illuminated with a Y-polarized light. (c) Illumination pattern in the k-space: Circles are the desired pattern, and crosses are the experimental pattern which is measured using Fourier analysis of the holograms.

Clearly, we do not have enough equations to find a 3×3 Jones matrix from these fields. We can rewrite this equation using block-matrices:

$$\begin{pmatrix} \vec{E}_{2 \times 2}^{out} \\ E_{z1}^{out} \quad E_{z2}^{out} \end{pmatrix} = \begin{pmatrix} \vec{J}_{2 \times 2} & J_{xz} \\ J_{yz} & J_{zz} \end{pmatrix} \begin{pmatrix} \vec{E}_{2 \times 2}^{illum} \\ E_{z1}^{illum} \quad E_{z2}^{illum} \end{pmatrix} \quad (3.9)$$

as a result we will have,

$$\vec{E}_{2 \times 2}^{out} = \vec{J}_{2 \times 2} \times \vec{E}_{2 \times 2}^{illum} + \begin{pmatrix} J_{xz} E_{z1}^{illum} & J_{xz} E_{z2}^{illum} \\ J_{yz} E_{z1}^{illum} & J_{yz} E_{z2}^{illum} \end{pmatrix} \quad (3.10)$$

Using the rotational matrix which is described in Eq. 3.5, we can find the components of E^{illum} . In the case of left-handed and right-handed input polarizations we have $E_{z1}^{illum} = -\sin\theta \cos(\pi/4 - \varphi)$ and $E_{z2}^{illum} = \sin\theta \cos(\pi/4 + \varphi)$. So, we will have,

$$\overline{J}_{2 \times 2} = \overline{E}_{2 \times 2}^{out} \times \left(\overline{E}_{2 \times 2}^{illum} \right)^{-1} - \sin\theta \begin{pmatrix} -J_{xz} \cos(\pi/4 - \varphi) & J_{xz} \cos(\pi/4 + \varphi) \\ -J_{yz} \cos(\pi/4 - \varphi) & J_{yz} \cos(\pi/4 + \varphi) \end{pmatrix} \left(\overline{E}_{2 \times 2}^{illum} \right)^{-1} \quad (3.11)$$

The first term of Eq. 3.11 is what we use in Eq. A.12 to reconstruct 2×2 scattering potential. We call it as the approximated Jones matrix, $\overline{J}_{2 \times 2}^{approx}$. On the other hand, we call the Jones matrix including the right term in Eq. 3.11 as the true Jones matrix, $\overline{J}_{2 \times 2}^{true}$.

We can rewrite Eq. 3.11 as follows,

$$\overline{J}_{2 \times 2}^{true} = \overline{J}_{2 \times 2}^{approx} - \begin{pmatrix} f_{11}(\theta, \varphi) J_{xz} & f_{12}(\theta, \varphi) J_{xz} \\ f_{21}(\theta, \varphi) J_{yz} & f_{22}(\theta, \varphi) J_{yz} \end{pmatrix} \quad (3.12)$$

where $f_{11}(\theta, \varphi)$, $f_{12}(\theta, \varphi)$, $f_{21}(\theta, \varphi)$, and $f_{22}(\theta, \varphi)$ can be found using Eq. 3.11 after inversion of $\overline{E}_{2 \times 2}^{illum}$.

We show the values of $f_{11}(\theta, \varphi)$, $f_{12}(\theta, \varphi)$, $f_{21}(\theta, \varphi)$, and $f_{22}(\theta, \varphi)$, in Fig. 3.4(a) for illuminations with a conical pattern. We can see that the maximum of these values is $\sin\theta$, which relates to the NA of the objectives. In our case, $\sin\theta = 0.4$ and the method is more accurate for illumination angles with smaller θ . For many cases like tissues that are placed on a coverslip (in XY-plane), the J_{xz} and J_{yz} terms are negligible as the tissue fibers are in XY-plane. However, even for the cases with J_{xz} and J_{yz} comparable to J_{xy} and J_{yx} , almost 50 % of projections have $f(\theta, \varphi)$ value smaller than 0.3.

However, the main reason that this is a good approximation can be justified by applying the Fourier diffraction theorem on Eq. 3.12. Wolf's method is a linear transform and as a result,

$$\overline{V}_{2 \times 2}^{true}(k_x - k_x^{in}, k_y - k_y^{in}, k_z - k_z^{in}) = \overline{V}_{2 \times 2}^{approx}(k_x - k_x^{in}, k_y - k_y^{in}, k_z - k_z^{in}) - \frac{k_z}{2\pi j} \mathcal{F}_{2D} \left\{ \begin{pmatrix} f_{11}(\theta, \varphi) J_{xz} & f_{12}(\theta, \varphi) J_{xz} \\ f_{21}(\theta, \varphi) J_{yz} & f_{22}(\theta, \varphi) J_{yz} \end{pmatrix} e^{j\vec{k}_{in} \cdot \vec{r}} \right\} (k_x, k_y) \quad (3.13)$$

the second term in Eq. 3.13 is the 3D tensorial reconstruction which is achieved by applying Wolf's method on 2D components of the tensor. It can be seen in Fig. A.5 that Jones matrix components change slightly for different illumination angles, and especially for the case of a thin-transparency, Jones matrix components such as J_{xz} or J_{yz} remain exactly similar for different illumination angles. In this situation, different projections with opposite signs of $f(\theta, \varphi)$ will cancel each other during the averaging process in the Fourier diffraction theorem over different illumination angles. For our numerical phantom, as we can calculate all of the 3×3 Jones matrix components, we can evaluate the accuracy of this approximation. In this regard, the xy component of the approximated scattering potential, V_{xy}^{approx} , and the true

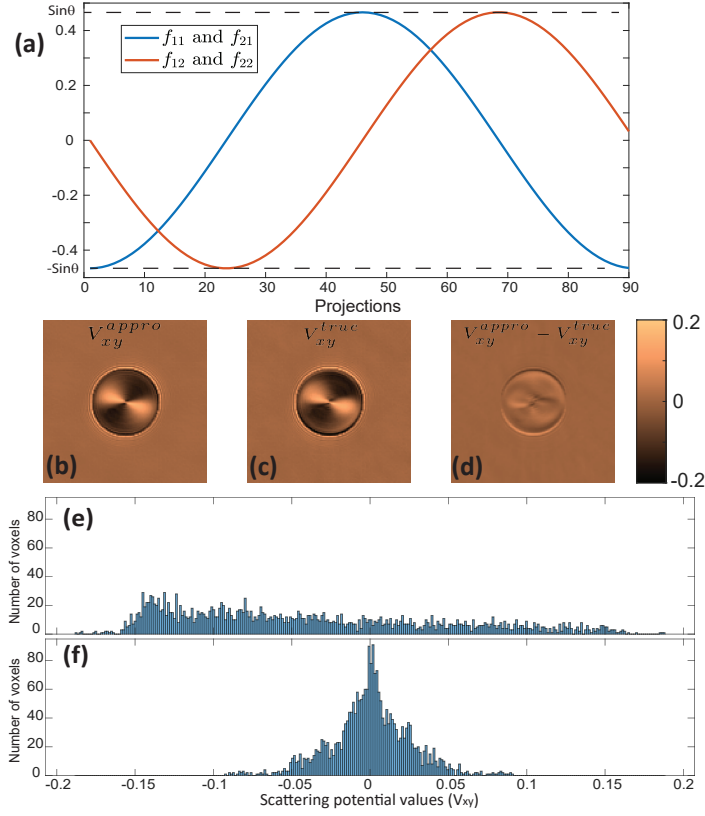


Figure 3.4: (a) Values of $f_{11}(\theta, \varphi)$, $f_{12}(\theta, \varphi)$, $f_{21}(\theta, \varphi)$, and $f_{22}(\theta, \varphi)$ for 90 projections with a conical pattern. (b) Calculated V_{xy}^{approx} , (c) V_{xy}^{true} , and (d) their difference regarding Eq. 3.13. (e) Histogram diagram of the true scattering potential values, and (f) the difference regarding Eq. 3.13.

scattering potential, V_{xy}^{true} , as well as the 3D reconstruction of the second term in Eq. 3.13 are shown in Fig. 3.4. We calculated the mean squared error (MSE) for this approximation as 7%. Additionally, for a better comparison of the true scattering potential and the error, Figs. 3.4(e-f) show the histogram diagrams of these 3D reconstructions in the plane of best focus. According to these figures, most of the values for the error is concentrated on zero or near zero, while the true reconstruction is very well distributed.

3.2.3 Relationship between reconstructions performed in different polarization states

As discussed earlier, the cross-polarized light shows zero intensities, especially at the background regions, and it results in random phase values. This makes the calibration of the off-set phase (which is necessary due to the phase fluctuations in the holography setups), and unwrapping challenging. To overcome this issue, we use the idea to make the input and measured polarization states differ by 45° . So, we illuminate a sample with $+45^\circ$ and -45° polarization states (*a* and *b*) with respect to the XY coordinate, and measure X-polarized and

Y-polarized lights. This configuration guarantees to have the background light intensity in all the measurements and avoid random phases. Now we explain how to convert these 4 tomographic reconstructions of the scattering potential, V_{xa} , V_{ya} , V_{xb} , and V_{yb} to the components of the scattering potential tensor, V_{xx} , V_{yx} , V_{xy} , and V_{yy} . At first, we find the relationship for the case with Born approximation. According to Eq. A.12, for two experiments of illumination with a -polarized and b -polarized light, we have:

$$\overline{\overline{V}}(k_x - k_x^{in}, k_y - k_y^{in}, k_z - k_z^{in}) = \frac{k_z}{2\pi j} \mathcal{F}_{2D} \left\{ \left(\begin{array}{cc} E_{xa}^s & E_{xb}^s \\ E_{ya}^s & E_{yb}^s \end{array} \right) \left(\begin{array}{cc} \tilde{E}I_{xa} & \tilde{E}I_{xb} \\ \tilde{E}I_{ya} & \tilde{E}I_{yb} \end{array} \right)^{-1} \right\} (k_x, k_y) \quad (3.14)$$

where $\tilde{E}I_{ij}$ is the amplitude of the input field component along i polarization when input field is $j = a, b$ polarized. Since, the input polarization is $\pm 45^\circ$, we have $\tilde{E}I_{xa} = \tilde{E}I_{ya} = \tilde{E}I_{xb} = -\tilde{E}I_{yb}$. By rewriting Eq. 3.14, we can get:

$$\begin{aligned} \overline{\overline{V}}(k_x - k_x^{in}, k_y - k_y^{in}, k_z - k_z^{in}) &= \frac{k_z}{2\pi j} \mathcal{F}_{2D} \left\{ \frac{1}{2\tilde{E}I_{xa}} \left(\begin{array}{cc} E_{xa}^s & E_{xb}^s \\ E_{ya}^s & E_{yb}^s \end{array} \right) \left(\begin{array}{cc} 1 & 1 \\ 1 & -1 \end{array} \right) \right\} (k_x, k_y) \\ &= \frac{k_z}{2\pi j} \mathcal{F}_{2D} \left\{ \frac{1}{2} \left(\begin{array}{cc} E_{xa}^s/\tilde{E}I_{xa} + E_{xb}^s/\tilde{E}I_{xb} & E_{xa}^s/\tilde{E}I_{xa} - E_{xb}^s/\tilde{E}I_{xb} \\ E_{ya}^s/\tilde{E}I_{ya} - E_{yb}^s/\tilde{E}I_{yb} & E_{ya}^s/\tilde{E}I_{ya} + E_{yb}^s/\tilde{E}I_{yb} \end{array} \right) \right\} (k_x, k_y) \end{aligned} \quad (3.15)$$

we can consider V_{ij} , $i \in x, y$, and $j \in a, b$, as the 3D scalar scattering potential which is reconstructed by applying the Wolf transform on $E_{ij}^s/\tilde{E}I_{ij}$. As a result, we will have:

$$\overline{\overline{V}} = \begin{pmatrix} V_{xx} & V_{xy} \\ V_{yx} & V_{yy} \end{pmatrix} = \frac{1}{2} \begin{pmatrix} V_{xa} + V_{xb} & V_{xa} - V_{xb} \\ V_{ya} - V_{yb} & V_{ya} + V_{yb} \end{pmatrix} \quad (3.16)$$

In the case of the Rytov approximation, we can replace $E_{ij}^s/\tilde{E}I_{ij}$ with $\log(1 + E_{ij}^s/\tilde{E}I_{ij})$ in Eq. 3.15. This gives us the same result as Eq. 3.16 to convert the reconstructed Rytov-based scalar scattering potentials to the elements of $\overline{\overline{V}}$.

As a result, based on the linearity of the scattering potential with scattered fields, achieved thanks to the single-scattering assumption, we can use Eq. 3.16 to calculate the scattering potential tensor elements using the $\pm 45^\circ$ -polarized data.

3.2.4 Experimental setup

The polarization-sensitive holographic tomography system used to acquire experimental data is shown in Fig. 3.3(a). The signal and reference arms are combined in an off-axis configuration to record holograms at different illumination angles. The source is a 488 nm CW fiber coupled laser diode, which is collimated and split into the signal and reference arms with a beamsplitter. The polarization of the signal arm is controlled with a half wave-plate (HW1) and a polarizer (P1). The illumination angle is scanned with a double-axis galvomirror. We consider two arbitrary polarization states for our illuminations, $+45^\circ$ and -45° , namely a , and b , according to Fig. 3.2(b). Thanks to a 4F system consisting of a lens, L1, and a 60X dry

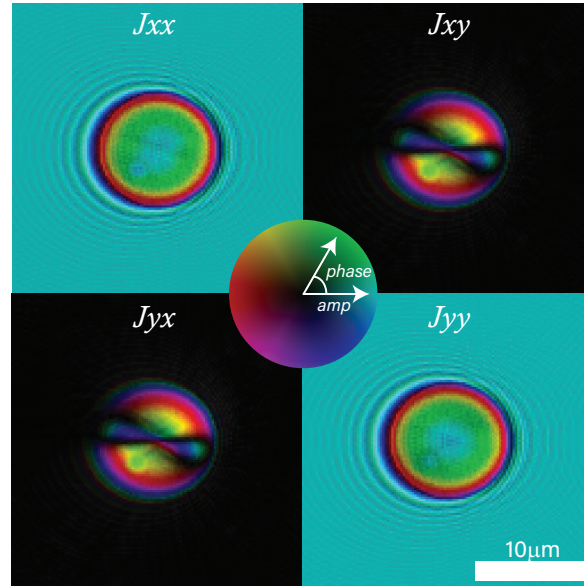


Figure 3.5: Complex Jones matrix calculated for a birefringent digital phantom with an illumination angle of $\theta = 25^\circ$ and $\phi = 0^\circ$. The synthetic measurements were generated using the V-BPM. In order to visualize the complex values, brightness shows the amplitude and color-code shows the phase of each Jones matrix component.

objective as the condenser, the position of the beam is fixed on the sample while scanning the angle. The imaging of the sample on a CCD camera is done using another 4F system with a water-dipping 60X objective and a tube lens (L2). The polarization of the reference arm is aligned at 45 degrees with respect to X and Y axis to get the same intensity of reference light for interference with both polarizations. The signal beam for which the polarization is chosen using an analyzer, in two states of X, and Y is combined with the reference arm by a beamsplitter. We measure 4 holograms totally and reconstruct the complex fields E_{xa} , E_{ya} , E_{xb} , and E_{yb} where in E_{ij} , j indicates the incident polarization and i indicates the output polarization. For calibration purposes (as the illumination fields are not perfect plane-waves), we measure E_{ij}^{illum} in the absence of the sample. In Fig. 3.3(b), the cross-polarized light due to the birefringence of the sample is shown in the absence of the reference beam, for the corn starch granule. Fig. 3.3(c), shows the illumination pattern in the k-space. The desired pattern is shown with circles. The experimental pattern is achieved using the Fourier map of the hologram, and is shown with crosses. For some angles, it is slightly different from the desired pattern, due to the imperfections of the galvo mirror. When we find the illumination pattern using our holograms, the $\overline{\overline{R}}$ matrix of Eq. 3.5(a) is calculated by sampling the pattern in Fig. 3.2(a) with the points in Fig. 3.3(c).

3.3 Results and discussion

3.3.1 Numerical Phantom

To evaluate the proposed 3D reconstruction method, we employed a numerical forward model, specifically the split-step V-BPM, to generate synthetic data and obtain 2D projections. The accuracy of the reconstruction method was evaluated by comparing it to the known index tensor distribution of the digital phantom. The derivation of the V-BPM forward model can be found in section 2 of Appendix A. The basic idea of this model is to propagate light slice-by-slice by dividing a 3D sample into multiple 2D slices. The relationship between two subsequent slices can be described by Eq. 3.17. To be specific, we can calculate the vector field, $\vec{E}(z + dz)$, by propagating the field from the previous slice, $\vec{E}(z)$, followed by the phase and amplitude modulation caused by the inhomogeneity and the birefringence of the medium, $\overline{\overline{\delta n}}(x, y, z)$:

$$\vec{E}(z + dz) = \expm\left(\frac{jk_0\overline{\overline{\delta n}}(z)dz}{\cos\theta}\right) \times \mathcal{F}^{-1}\left\{e^{-j\frac{k_x^2+k_y^2}{k+k_z}dz} \times \mathcal{F}\{\vec{E}(z)\}\right\} \quad (3.17)$$

where dz is the step size, \expm is the matrix exponential applied on the RI tensor, $\overline{\overline{\delta n}}$, \mathcal{F} is the 2D Fourier transform, and $k_x, k_y, k_z = \sqrt{k^2 - k_x^2 - k_y^2}$ represent the spatial frequencies in each direction.

The scattered vector fields are calculated for a digital phantom with $+45^\circ$, and -45° -polarized input fields using the V-BPM. The rotational matrix described in Eq. 3.5 and Eq. 3.6 is also considered. Four complex calculated fields, normalized to the input vector fields to give the Jones matrix are shown in Fig. 3.5, for illumination with $\theta = 25^\circ$, and $\phi = 0^\circ$ where θ and ϕ are defined in Fig. 3.2(b). 90 projections are calculated keeping θ but varying ϕ . Then, we use these data for our reconstruction. The reconstruction process is similar to what we use for the experimental data. We reconstruct based on the Rytov approximation and then convert the reconstructions to get n_{xx} , n_{yx} , n_{xy} , and n_{yy} . In Fig. 3.6, we present the reconstruction of n_{xx} and n_{yx} , and compare them with the ground truth. We can see the underestimation and elongation along the optical axis, which is due to the missing spatial frequencies, similar to the scalar ODT [26]. The full reconstruction of the tensor is shown in section 4 of Appendix A and discussed in detail. We define the mean squared error (MSE) as $MSE = \|n^{\text{reconstruction}} - n^{\text{ground-truth}}\|^2 / \|n^{\text{ground-truth}}\|^2$ to perform a quantitative evaluation on the 3D reconstruction of the RI tensor with respect to the ground-truth. This MSE metric is calculated separately for each component of the tensor. Based on our calculation of the data of Fig. 3.6, for n_{xx} , the MSE of the reconstruction at the plane of focus ($z = 0\mu m$) is 0.104 and the total MSE is 0.381. On the other hand, for n_{yx} , the MSE of the reconstruction at the plane of focus is 0.317 and the total MSE is 0.451. The larger value of the total MSE is due to the fact that the Rytov reconstruction is always better in the plane of best focus.

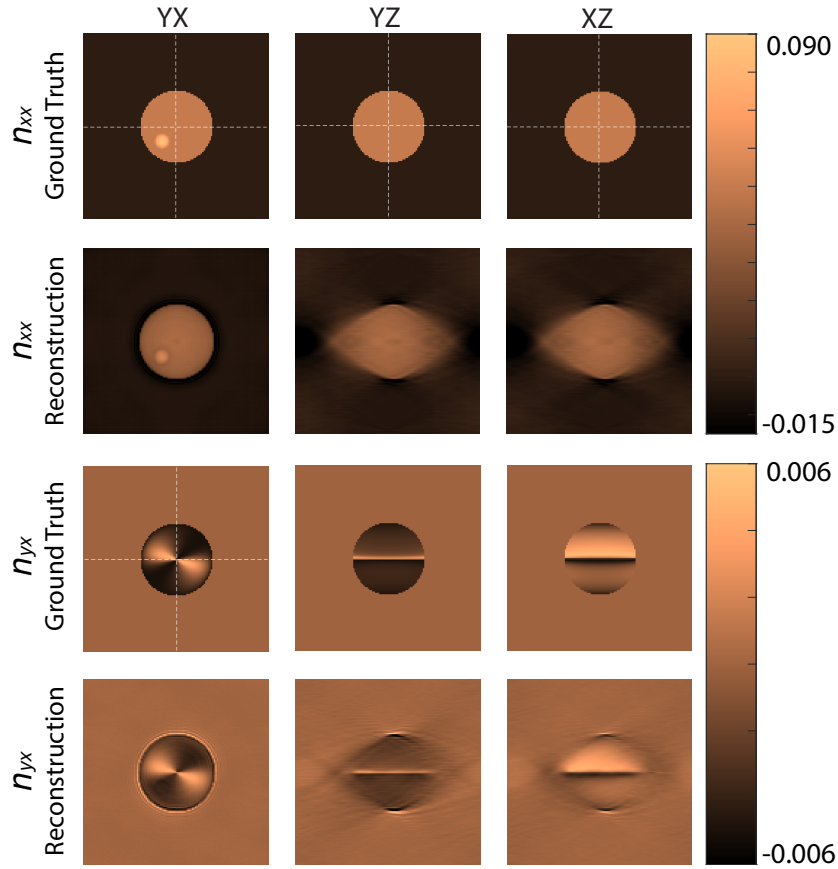


Figure 3.6: Reconstruction of the digital birefringent phantom using the Rytov approximation. The first and second rows show YX, YZ, and XZ profiles of the ground-truth, and reconstruction of n_{xx} , respectively. The third and fourth rows show the same profiles for n_{yx} . Full tensor ground truth and reconstructions are presented in section 4 of Appendix A. The colorbars show the refractive index contrast and are unitless.

3.3.2 Experiment

As proof of concept of our method, we first demonstrate our experimental setup by reconstructing the 3D RI tensor of a cornstarch granule. Cornstarch granules, which exhibit a simple birefringent structure, were suspended in silicone oil ($n_0 = 1.43$) and placed between two #1 glass coverslips for imaging. Here, in order to overcome the phase unwrapping problem in the presence of experimental noise, we use the idea of nonaligned input and output polarization. As a result, the sample is illuminated from different angles with $+45^\circ$, and -45° -polarized light and we measure X, and Y components of the output field. Then, the reconstructions are processed to get RI tensor in the XY coordinate system. A 3D total-variation (TV) denoising algorithm as defined in Eq. A23 of Appendix A with a regularization parameter of $\lambda = 2 \times 10^{-3}$ is used on the final reconstructions to diminish the coherent noise due to the unwanted reflections on the final reconstructions [66]. This TV algorithm is only for denoising purposes, directly applied to the final images, and does not compensate for the missing-cone problem.

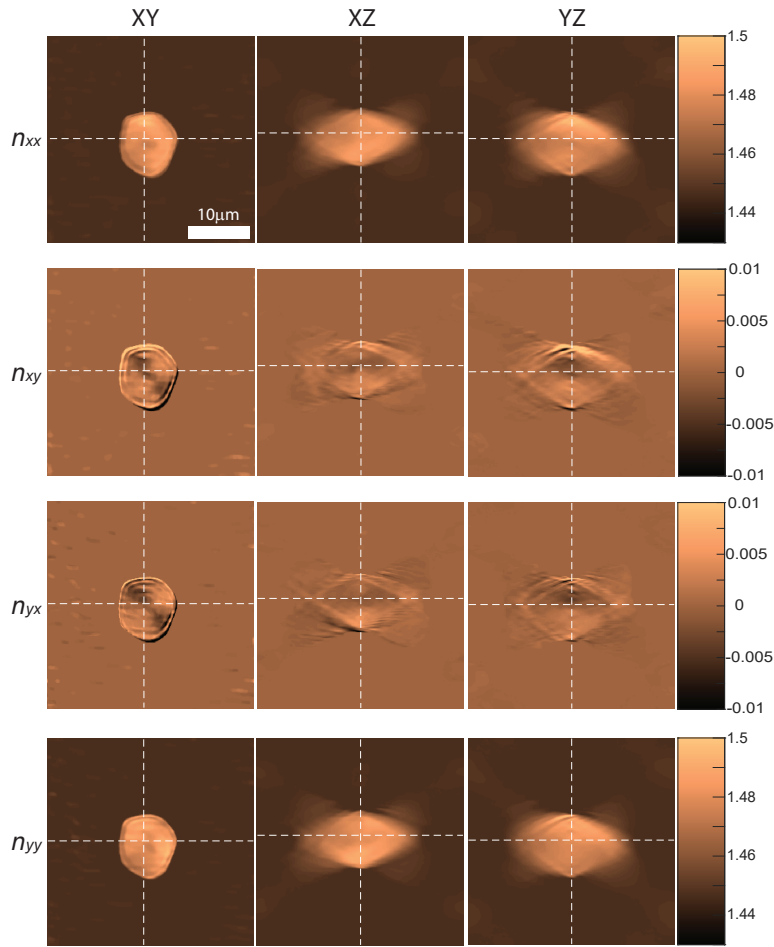


Figure 3.7: YX, XZ, and YZ profiles of the 3D RI tensor reconstruction of corn starch granule. The colorbars show the refractive index contrast and are unitless.

This issue is elaborated in section 5 of Appendix A. Results are shown in Fig. 3.7, where we can see four different components of the RI tensor, n_{xx} , n_{xy} , n_{yx} , and n_{yy} , in 3D. As it can be seen in the off-diagonal terms of the RI tensor, there are some azimuthally varying structures that came from the amylopectin crystalline structures growing radially in corn, from its hilum. The diagonal RI components are bereft of this information, the same as the conventional scalar ODT.

Next, we investigate the viability of using our method for more complex anisotropic samples. We present a case study using *ex vivo* mouse muscle tissue, a well-studied example of a naturally birefringent tissue [67]. Striated muscle fiber cells in mammals contain repeated longitudinally connected units known as sarcomeres, which are periodically organized into substructures including A-bands (anisotropic) and I-bands (isotropic). As the characteristic length scale of A- and I- bands is on the order of $1\mu m$ muscle tissue is well suited for a demonstration of our method. Fresh *ex vivo* mouse muscle was cryo-embedded, sectioned

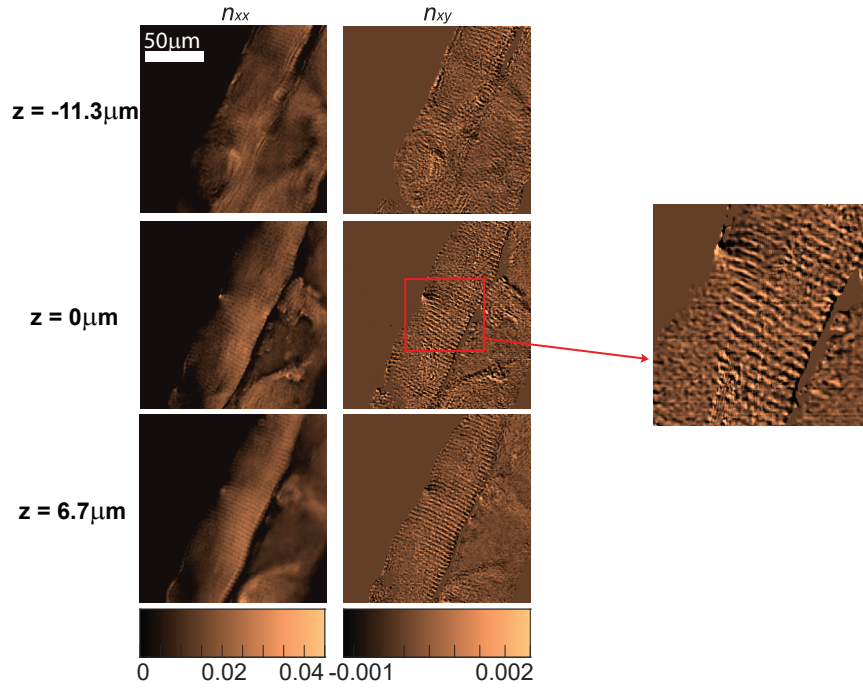


Figure 3.8: YX profiles of the 3D reconstructions of the RI tensor components, n_{xx} and n_{xy} , for a $20\mu\text{m}$ thick muscle tissue in three different depths. The inset shows a 2.5X magnified section of n_{xy} YX profile which clarifies the sarcomere structure with A-bands and I-bands in one muscle fiber. The colorbars show the refractive index contrast and are unitless.

into $20\mu\text{m}$ slices, mounted on a coverslip with water immersion, and imaged under the same conditions as the previous experiment. The cross-polarized image is shown in Fig. A9 of Appendix A. The regularization parameter in the 3D TV denoising algorithm for this muscle tissue is $\lambda = 0.8 \times 10^{-3}$ and is applied directly on the final 3D RI tensor reconstructions. Fig. 3.8 shows YX slices from the 3D reconstruction of the RI tensor at three different depths. The section of the tissue sample shown here consists of two *en face* muscle fiber cells which are separated by a thin layer of connective tissue. The inset in Fig. 3.8 providing a closer look at n_{xy} term, indicates that this measurement could be used to extract quantitative morphological data about the sarcomere structure. Some evidence of these structures is also visible in the images of n_{xx} , which can be attributed to the fact that both quantities are related to the local mass density.

3.3.3 Coordinate-invariant polarization-sensitive contrast metrics

The RI tensor which contains n_{xx} , n_{xy} , n_{yx} , and n_{yy} components, depends on the coordinate system which has been chosen arbitrarily. One can change the coordinate system and get a new RI tensor. For example, when the coordinate system matches with the optical axes of the sample, we will have a diagonal RI tensor. As a result, the values of off-diagonal components in the RI tensor do not directly indicate the inherent birefringence of the sample. A sample

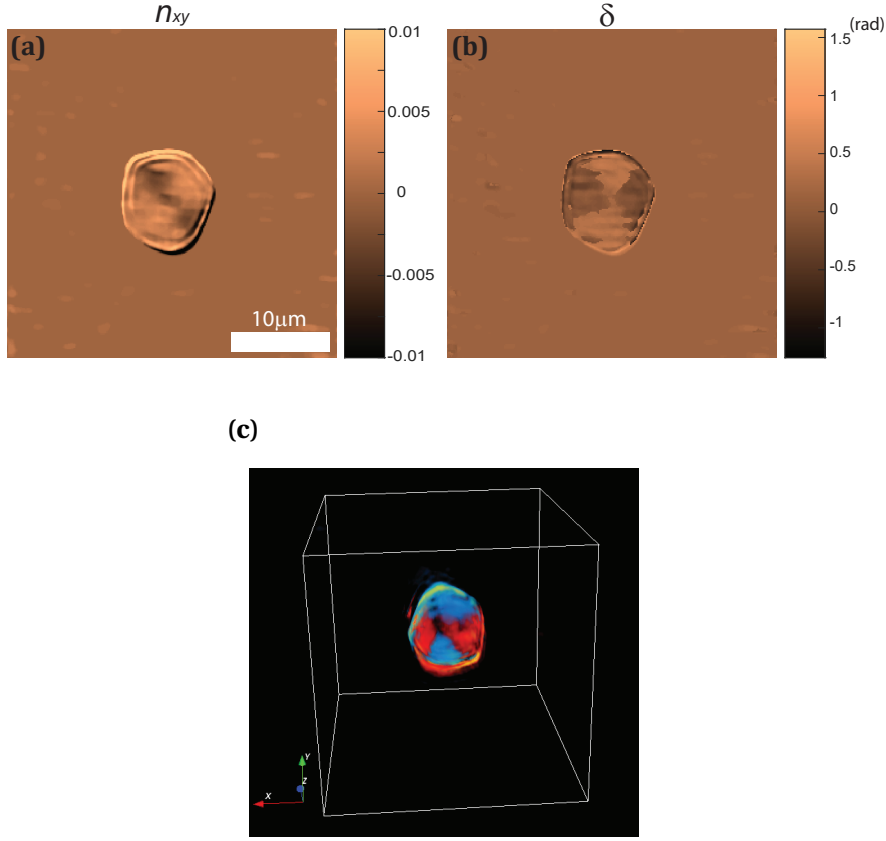


Figure 3.9: A comparison between the YX profiles of the 3D reconstructions of (a) n_{xy} and (b) phase retardation for corn starch granule. (c) A 3D rotating rendering of the phase retardation.

with a larger value of n_{yx} in a particular location may be less birefringent than another sample with a smaller n_{yx} depending on the orientation of the local optical axis with respect to the laboratory coordinates.

To solve this issue, we can study the eigenvalue decomposition of the RI tensor. The eigenvalues of a matrix are invariant under any unitary transformation, such as the coordinate rotation. We can consider the local phase modulation tensor in Eq. 3.17, $\expm(jk_0 dz \overline{\overline{n}})$, that the electric field vector experiences by propagation through a step dz . This step is a linear operator and its eigenvectors and eigenvalues can be readily calculated. We use the *difference* in the phases of these eigenvalues, (δ^1 and δ^2) as the contrast metric since they convey the local retardation, independently of orientation. It has been shown in section 2 of Appendix A that δ is directly related to the eigenvalues of the RI tensor $\mu_n^{1,2}$:

$$\delta = \delta^1 - \delta^2 = k_0 dz (\mu_n^1 - \mu_n^2) \quad (3.18)$$

The phase retardation, $\delta(x, y, z)$, is a 3D scalar quantity which is invariant under any rotation of the coordinate system in the XY plane. In Fig. 3.9 we present the calculated 3D phase retarda-

tion for the corn starch granule. The YX profiles of the reconstructed n_{xy} and phase retardation are compared in Fig. 3.9(a) and (b). We can see that these two contrast metrics can show different shapes depending on the local orientation of the optical axis. A 3D rotating rendering of the phase retardation rendered with Icy platform [68] is shown in Fig. 3.9(c). It should be mentioned that eigen-value and eigen-vector characterization of the RI tensor is the key point to quantify the parameters of anisotropy with a physical meaning. Each component of the RI tensor, by itself, does not convey information about the local birefringence or the local direction of the fibrous structures of the sample. However, the birefringence can be calculated as the difference in the eigen-values of the RI tensor ($\mu_n^1 - \mu_n^2$), and the slow-axis orientation of the sample can be calculated by eigen-vectors of the RI tensor. These parameters (that have been shown and discussed in section 4 of Appendix A) are inherent properties of the sample and do not get affected by the orientation of the experimental coordinate.

3.4 Conclusion

To summarize, our study examined optical diffraction tomography in anisotropic settings and highlighted the impact of input polarization on conventional ODT reconstruction for birefringent samples. We developed a linear ODT model for refractive index (RI) tensors, utilizing the Rytov approximation, and demonstrated its efficacy through numerical simulations using the V-BPM forward model. Furthermore, we employed a polarization-sensitive holography setup to reconstruct 3D RI tensors using vectorial scattered fields from multiple angles.

Our direct reconstruction method can be further improved by incorporating iterative reconstruction schemes along with nonlinear forward models, such as our V-BPM, and we expect to extend the previously developed learning tomography approaches for isotropic samples to general anisotropic samples [27]. Polarization-sensitive ODT, should be important for biological samples with fibrous structures, to provide information about the biological details related with the birefringence of the sample and can be resolved in the off-diagonal components of the RI tensor or the 3D phase retardation.

3.5 Follow-up works

Our results on polarization-sensitive ODT opened up a new research line in ODT and quantitative phase microscopy. We showed the first experimental reconstruction of the refractive index tensor based on several approximations that we discussed in this chapter. There have been several papers recently published based on our results. As we discussed in section 3.2.2, the ambiguity due to the inaccessible z-polarization component causes inaccuracies in the tensor reconstruction. Recently Ref.[69] presented a method to solve this issue. The idea of this work is to retrieve the z-component of the tensor by slightly tilting the illumination angle and using the Fourier differentiation theorem. This is based on the approximation that the Fourier transform of the scattering potential tensor does not change much with the small

tilt in the illumination angle. Later, they also presented a regularized reconstruction of the refractive index tensor using an iterative optimization algorithm [70]. Our reconstruction technique was based on the holographic measurements of the Jones matrix. It has been shown that by using an iterative reconstruction method, an intensity-based polarization-sensitive ODT can be achieved [71].

4 Second-harmonic ODT

This chapter is a pre-print version of the following paper:

- A. Saba, C. Gigli, Y. Pu, and D. Psaltis (2023). "Second-harmonic optical diffraction tomography". to be submitted.

4.1 Introduction

Second-harmonic (SH) microscopy is a nonlinear optical imaging technique that illuminates the sample with a high-power coherent source and images the generated light at a double frequency. This microscopy technique is based on the second-harmonic generation (SHG) process due to the interaction of light with the second-order susceptibility of the material, $\chi^{(2)}$ [30]. In SHG, two photons at the fundamental frequency interact with the second-order susceptibility, and a photon at the double frequency is generated. Owing to the fact that the second-order susceptibility is vanishing in the case of centro-symmetric molecular structure, SHG can present a microscopy modality that reveals non-centro-symmetric features in a background-free image. Additionally, the SHG process is a parametric conversion in which there is no optical energy deposition upon the sample, in other words, the energy of the SH-emitted photon is the same as the energy of the two annihilated photons. These two features make SH imaging an interesting microscopy modality for biological applications which was under intensive research study in the previous years in both wide-field and confocal configurations [72], [73].

In comparison with other background-free imaging modalities such as fluorescent microscopy, SH microscopy has several advantages. The first advantage is its stability, SHG does not experience blinking or photobleaching. The SHG is a narrow-band signal and is spectrally far from the fundamental beam, making it appropriate for the background-free imaging modality. SH emission is spectrally tunable with the fundamental beam wavelength and its emission wavelength does not depend on a specific dye. The other important feature is the temporal coherence of SHG which provides the possibility of interference-based imaging and

holography. As a result, Pu, et al. [74] presented harmonic holography where we can measure the amplitude and phase of the SH-generated beam using off-axis holography. This approach was used for focusing SH light in a turbid medium using Second Harmonic Radiation Imaging Probes [75], [76] and SH-holographic imaging of biological samples [77].

In this chapter, we present second-harmonic optical diffraction tomography (SH-ODT) to reconstruct the 3D distribution of the $\chi^{(2)}$ of the sample as a new modality or contrast agent for ODT. The 3D tomographic reconstruction is based on the 2D complex SH-generated fields by the sample, which are measured using harmonic holography as the sample is illuminated with a high-power pulsed laser from different angles. We call these SH projections. The tomographic reconstruction of SH was shown in [78], not in the ODT configuration, but using short-coherent-gated 3D sectioning which has a limited axial resolution. Very recently, the theoretical formalism for SH-ODT was proposed in [79], a concurrent work with ours. However, Ref. [79] does not provide any experiments or validation of the proposed method which is the main challenge in SH-ODT. SH-ODT requires very sophisticated experiments which we will discuss in this chapter. We provide synthetic data for digital $\chi^{(2)}$ phantoms to validate the formalism and we demonstrate our methodology by reconstructing the muscle tissue, experimentally.

4.2 Mathematical formalism

In this section, we present the mathematical description of the SHG by a sample with an inhomogeneous linear refractive index, $n(r)$, and an inhomogeneous second-order susceptibility, $\chi^2(r)$, and also the inverse SHG problem by applying the Fourier diffraction theorem [13] for the SH Helmholtz equation. As discussed in the introduction, second-order susceptibility exists where the sample is not centrosymmetric. During the SHG process, two photons at the fundamental wavelength, λ_f interact with the sample, and a photon at the SH wavelength, $\lambda_{SH} = \lambda_f/2$ is generated. The nonlinear Helmholtz equation at fundamental and SH frequencies can describe the scattering and the depletion of the fundamental beam at λ_f , as well as the generation and scattering of the SH beam at λ_{SH} [30]. It should be noted that the second-order susceptibility of the samples is usually anisotropic and a vectorial formalism should be presented to consider the polarization of light in the nonlinear Helmholtz equation. However, we assume that the linear refractive index of the sample, $n(r)$ is a scalar distribution, and also, we assume that the inhomogeneity correlation length of the sample is much longer than the wavelength, and as a result, we can neglect the depolarization term, $\nabla \nabla \cdot E$, in the vectorial nonlinear Helmholtz equation [80].

It has been shown in Appendix B that if we neglect the re-scattering of the SH-generated field, and also consider the Born approximation (neglecting the linear scattering) it can be written that,

$$\vec{E}^{SH}(r) = \int G^{SH}(\mathbf{r} - \mathbf{r}') \cdot E_0^2 e^{2j\vec{k}_{in} \cdot \mathbf{r}'} \cdot \vec{V}^{SH}(\mathbf{r}') \vec{Q}_{illum} d\mathbf{r}' \quad (4.1)$$

where $\vec{E}^{SH}(r)$ is the SH field vector in the location \mathbf{r} , $G^{SH}(\mathbf{r}-\mathbf{r}') = e^{jk_{SH}n_0|r-r'|}/|\mathbf{r}-\mathbf{r}'|$ is the Green's function of the SH Helmholtz equation with $k_{SH} = 2\pi/\lambda_{SH}$, $\vec{V}^{SH}(\mathbf{r}') = \frac{k_{SH}^2}{4\pi}\vec{\chi}^{(2)}(\mathbf{r}')$ is the SH scattering potential tensor with the size 3×6 , and we define the second-order vector $\vec{Q}_{illum} = [p_x^2, p_y^2, p_z^2, 2p_y p_z, 2p_x p_z, 2p_x p_y]^T$. The vector $\vec{p}_{illum} = [p_x, p_y, p_z]^T$ shows the polarization state of the incident beam as $\vec{E}^I(\mathbf{r}') = e^{j\vec{k}_{in}\cdot\mathbf{r}'}\vec{p}_{illum}$ and is always perpendicular to the illumination wave-vector, $\vec{p}_{illum} \cdot \vec{k}_{in} = 0$.

Next, we can invert Eq. 4.1 for the plane wave illumination beam $E^I(\mathbf{r}') = e^{j\vec{k}_{in}\cdot\mathbf{r}'}\vec{p}_{illum}$ using the Fourier diffraction theorem. We have discussed in section 2 of Appendix B the details of the Fourier domain inversion. In the simplest case, we can consider the scalar SH scattering potential and discard the vectorial formalism. In this case, the SH scattering potential can be found as,

$$V^{SH}(K_x - 2k_x^{in}, K_y - 2k_y^{in}, K_z - 2k_z^{in}) = \frac{K_z}{2\pi j E_0^2} \mathcal{F}_{2D}\{E^{SH}\}(K_x, K_y) \quad (4.2)$$

in which, \mathcal{F}_{2D} is the 2D Fourier transform, K_x and K_y are the Fourier components in the transverse direction, and $K_z = \sqrt{(k_{SH}n_0^2)^2 - K_x^2 - K_y^2}$. Eq. 4.2 shows a relationship in order to fill the 3D Fourier domain of the SH scattering potential with the 2D Fourier transform of the complex SH-generated fields. It is clear based on this equation that Ewald's spheres are two-folded bigger and the shift should be $2\vec{k}_{in}$.

Eq. 4.2 is valid for a scalar $\chi^{(2)}$ distribution. It is also applicable if we assume that the illumination angle is small and the polarization vector \vec{p}_{illum} is not changing a lot by angle change. In this case, it can provide an effective distribution of $\chi_{eff}^{(2)}$ which can qualitatively show interesting features in the 3D reconstruction. However, it will be not physically clear how this effective second-order susceptibility distribution will be related to the elements of $\chi^{(2)}$ tensor as long as we do not know the crystalline orientation of the sample. In order to present a polarization-sensitive approach and a quantitative reconstruction of the elements of the SH scattering potential tensor, we can use the methodology that we presented in [80] which is also proposed recently in [79]. For this purpose, we illuminate the sample for each illumination angle with different input polarization states and measure the complex SH-generated field for each input polarization state. Since the $\chi^{(2)}$ is a rank-3 tensor, we can have 3 independent experiments or polarization states for each illumination angle, in contrast to the linear case in which we can only have two independent states [80]. The theoretical details of the polarization-sensitive SH-ODT are presented in section 2 of Appendix B. We can see that a 2×3 section of the SH scattering potential tensor can be approximately found as,

$$\vec{V}_{2 \times 3}^{SH}(K_x - 2k_x^{in}, K_y - 2k_y^{in}, K_z - 2k_z^{in}) = \frac{K_z}{2\pi j E_0^2} \mathcal{F}_{2D} \left\{ \begin{bmatrix} E_{x1}^{SH} & E_{x2}^{SH} & E_{x3}^{SH} \\ E_{y1}^{SH} & E_{y2}^{SH} & E_{y3}^{SH} \end{bmatrix} [\vec{s}_1, \vec{s}_2, \vec{s}_3]^{-1} \right\} (K_x, K_y) \quad (4.3)$$

in which E_{ij}^{SH} is the complex 2D SH field at the imaging plane polarized along $i \in \{x, y\}$ for the input polarization state of $j \in \{1, 2, 3\}$, $\vec{s}_j = [p_x^2, p_y^2, 2p_x p_y]^T$ is a part of the vector \vec{q}_{illum} for the input polarization state of j , and the $\vec{V}_{2 \times 3}^{SH}$ is a matrix containing 6 elements of the full SH scattering potential tensor as,

$$\vec{V}_{2 \times 3}^{SH} = \frac{k_{SH}^2}{4\pi} \begin{bmatrix} \chi_{11}^{(2)} & \chi_{12}^{(2)} & \chi_{16}^{(2)} \\ \chi_{21}^{(2)} & \chi_{22}^{(2)} & \chi_{26}^{(2)} \end{bmatrix} \quad (4.4)$$

Eq. 4.3 shows how the complex SH-generated fields for 3 different independent input polarization states can be combined to create the Ewald's spheres and fill the 3D Fourier domain of the elements of the SH scattering potential tensor. This process is shown in Fig. (b). After measuring the complex SH fields holographically, we can use Eq. 4.3 to fill the 3D Fourier domain of each element of the tensor, and we can take the inverse 3D Fourier transform for each element to calculate its 3D spatial distribution. We have presented numerical and experimental results in section 4.3 to validate this formalism.

The inversion of the SHG in Eq. 4.2 is based on the zeroth-order Born approximation which completely neglects the linear scattering of the sample at the fundamental wavelength. However, if we have the viability to measure the complex fundamental scattered field, we can slightly improve the zeroth-order Born approximation by replacing $\{E^{SH}\}$ with $\{E^{SH} (E^F / E^I)^{-2}\}$ in Eq. 4.2 where E^F and E^I are the complex 2D fields with and without the sample, respectively. We call this approach corrected-field-Born approximation and the mathematical details for this approximation are presented in section 3 of Appendix B.

Due to the limited numerical aperture of the imaging optics, the limited number of projections, and also having the transmission configuration, we cannot retrieve all the 3D spatial frequencies of the SH scattering potential tensor elements. This issue is the same as the linear ODT, known as the missing cone problem, which was under intensive research study in the previous years [26]. Missing cone problem causes the 3D reconstructed scattering potential to be underestimated and also elongated along the optical axis, here z -axis. One way to fix this issue is to use a piece of prior information on the reconstruction elements of the SH scattering potential tensor. Here, we use a Total-Variation (TV) sparsity condition to regularize the reconstruction of the SH inverse problem. For this purpose, after reconstructing the 3D Fourier domain of the SH scattering potential tensor using Eq. 4.2 in the scalar case, and Eq. 4.3 in the vectorial case, which we call the mn element of its tensor as $\tilde{V}_{mn}^{SH, recon}(K_x, K_y, K_z)$, we optimize the following minimization task to find the $V_{mn}^{SH, opt}$,

$$V_{mn}^{SH, opt} = \arg \min_x [\|\mathcal{F}_{3D}\{x\} - \tilde{V}_{mn}^{SH, recon}\|_2^2 + \mathcal{R}_{TV}\{x\}] \quad (4.5)$$

in which $\mathcal{R}_{TV}\{x\}$ is the gradient-based TV regularization on the 3D distribution of x . We will see in the next section how this iterative approach can help in facing the missing cone problem for the 3D reconstruction of the SH scattering potential tensor.

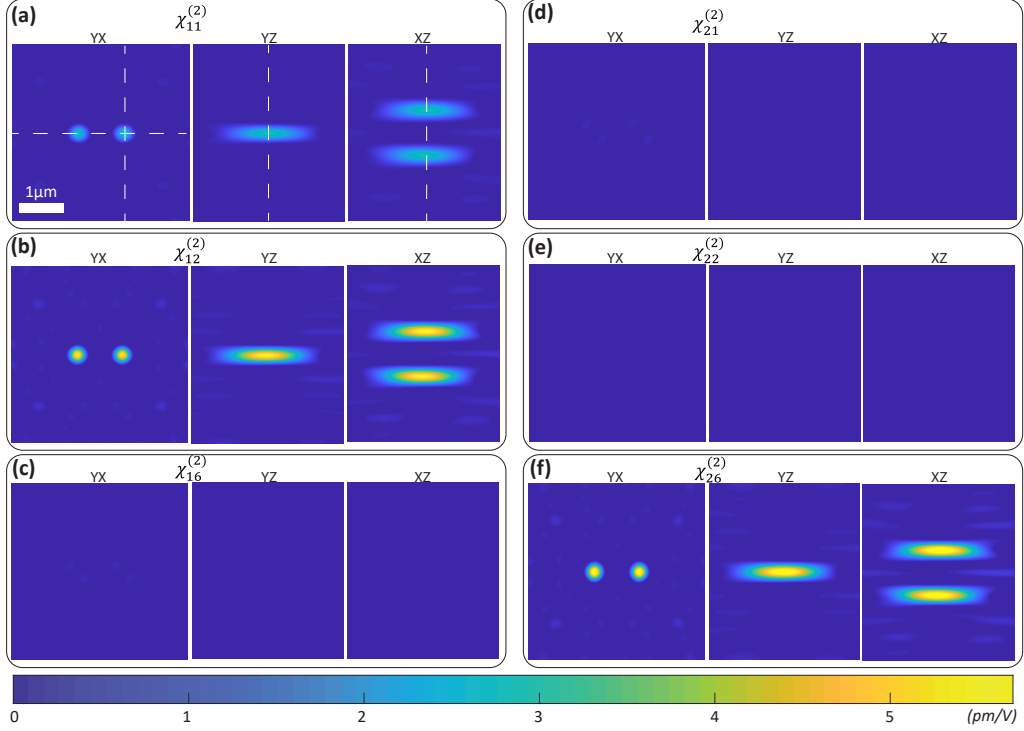


Figure 4.1: 3D reconstruction of second-order susceptibility tensor using synthetic data. The 6 elements of the second-order susceptibility tensor achieved using Eq. 4.3 are presented in (a) $\chi_{11}^{(2)}$, (b) $\chi_{12}^{(2)}$, (c) $\chi_{16}^{(2)}$, (d) $\chi_{21}^{(2)}$, (e) $\chi_{22}^{(2)}$, and (f) $\chi_{26}^{(2)}$, respectively. Each figure presents the 3D reconstruction in YX, YZ, and XZ planes.

4.3 Results

In this section, we present 3D reconstructions of $\chi^{(2)}$ distribution using the presented formalism in section 4.2. To evaluate the mathematical formalism, we first reconstruct a sample with a known ground-truth $\chi^{(2)}$ distribution using a set of synthetic measurements. In the second subsection, we present our experimental reconstruction of muscle tissue using an SH-holographic setup which we will discuss.

4.3.1 3D $\chi^{(2)}$ reconstruction based on synthetic data

We consider a 3D distribution of Barium titanate (BTO) nano-particles immersed in a background medium with the refractive index of $n_0 = 1.7$. BTO nano-particles have a $4mm$ group symmetry with non-zero $\chi_{15}^{(2)}$, $\chi_{24}^{(2)} = \chi_{15}^{(2)}$, $\chi_{31}^{(2)}$, $\chi_{32}^{(2)} = \chi_{31}^{(2)}$, and $\chi_{33}^{(2)}$ elements in their second-order susceptibility tensor. We generate complex fields at fundamental, $\lambda = 1030nm$, and SH, $\lambda = 515nm$ simulated with two frequency-domain Finite-element-method (FEM) simulations, at each of these wavelengths, coupled to each other. The simulations are done using a commercial FEM solver (COMSOL Multiphysics 5.4). We illuminate the sample with different angles and collect the complex fields at the fundamental and SH wavelengths. We use these

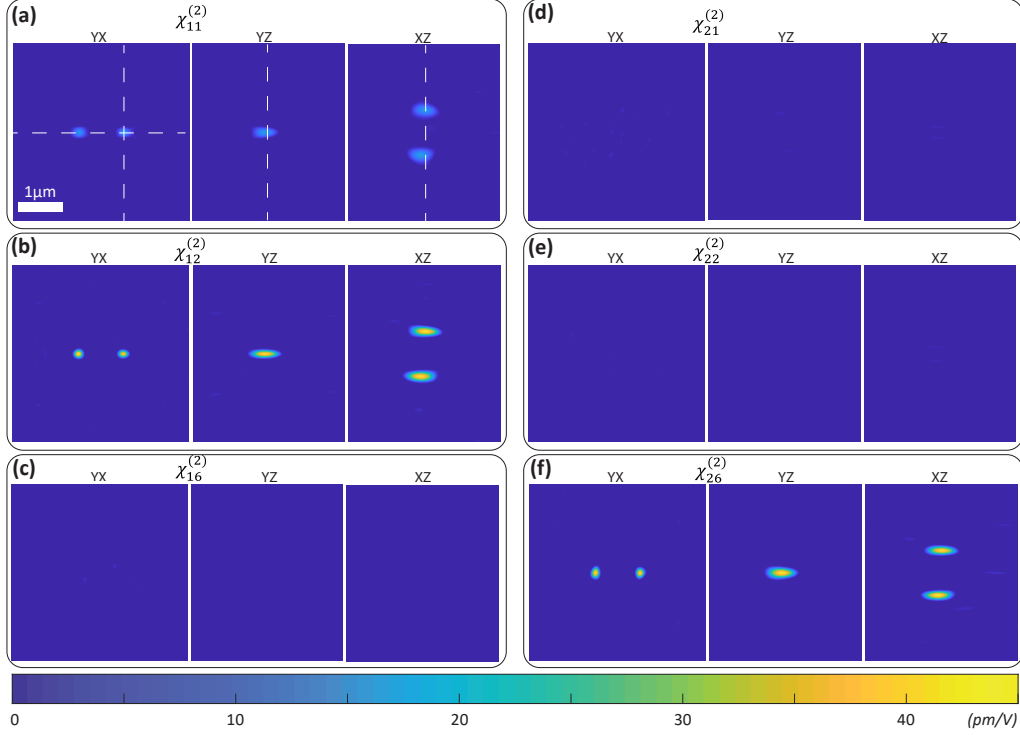


Figure 4.2: TV-based iterative reconstruction of second-order susceptibility tensor using synthetic data. The 6 elements of the second-order susceptibility tensor achieved using Eq. 4.5 are presented in (a) $\chi_{11}^{(2)}$, (b) $\chi_{12}^{(2)}$, (c) $\chi_{16}^{(2)}$, (d) $\chi_{21}^{(2)}$, (e) $\chi_{22}^{(2)}$, and (f) $\chi_{26}^{(2)}$, respectively.

data for the 3D reconstruction of our sample. The simulated sample consists of two BTO nano-particles with a diameter of $200nm$. aligned with the same crystalline orientation. The sample is illuminated with a circular pattern with the maximum angle of 10° . We have 3 input polarization states. X-polarized input, Y-polarized input, and diagonally-polarized (45°) input. The SH-generated light is calculated for all the angles and input polarization states. The cz-axis of two BTO particles is oriented along the X-axis of the experimental coordinate system. As a result, the second-order susceptibility tensor of these particles is as follows,

$$\bar{\chi}^{(2)} = \begin{pmatrix} \chi_{33}^{(2)} & \chi_{31}^{(2)} & \chi_{31}^{(2)} & 0 & 0 & 0 \\ 0 & 0 & 0 & 0 & 0 & \chi_{15}^{(2)} \\ 0 & 0 & 0 & 0 & \chi_{15}^{(2)} & 0 \end{pmatrix} \quad (4.6)$$

We use the synthetic data for different input polarization states and different illumination angles calculated using FEM, and use first-order Born approximation and Eq. 4.3 to calculate the 3D distribution of the SH susceptibility. We present the results in Fig. 4.1. The 6 elements of the $\bar{\chi}^{(2)}$ tensor is reconstructed and presented in this figure. The reconstruction is underestimated and elongated along the optical axis due to the missing-cone problem, but it matches with the ground-truth knowledge of the sample, as the $\chi_{16}^{(2)}$, $\chi_{21}^{(2)}$, and $\chi_{22}^{(2)}$ elements are zero, matching with Eq. 4.6, and the ratio of the other 3 non-zero elements are matching with the

ground-truth values.

In Fig. 4.2, the iterative reconstruction of the second-order susceptibility tensor using a TV-regularization is presented, as explained in Eq. 4.5. All 6 elements of the tensor are shown. A comparison of this figure with Fig. 4.1 clarifies how iterative reconstruction and TV-regularization help to solve the underestimation of the reconstruction and elongation along the optical axis. The values of the TV-based iterative reconstruction are much closer to the ground-truth values and $\chi_{16}^{(2)}$, $\chi_{21}^{(2)}$, and $\chi_{22}^{(2)}$ elements are zero, as the crystalline orientation implies.

4.3.2 Explanation of the experimental setup

We discussed the 3D reconstruction of the SH scattering potential tensor in the scalar and polarization-sensitive scenarios based on the 2D measurement of the SH-generated fields for each illumination angle. In this subsection, we present a summary of the experimental setup in order to measure the complex SH fields holographically and the 3D reconstruction of biological samples having endogenous second-order susceptibility.

The first experiments for digital harmonic holography were presented in [74]. We use the same principles to build a polarization-sensitive and multi-angle SH-holography setup. The polarization-sensitive holographic SH-ODT system we use to acquire our experimental SH complex fields for different samples of interest is shown in Fig 4.3(a). The light source is a yttrium-doped fiber laser (Amplitude Laser Satsuma) with a wavelength of $\lambda_F = 1030\text{nm}$, 280fs pulses, and a repetition rate of 125kHz, which leads to the pulse energy of $40\mu\text{J}$. The power of the source beam is controlled with a Half-waveplate (HW1) and a polarizer (P1) which sets its polarization to the horizontal direction (x -axis). The source beam is split into the signal and the reference arms using a beam splitter (BS1). The polarization of the signal arm is controlled with another half-waveplate (HW2) and we can set it to 3 independent states of horizontal, vertical, and 45-deg input polarization states. Using a galvo mirror (GM-V), we change the illumination angle in the vertical direction. GM-V is then imaged on a secondary galvo mirror (GM-H) using a 4F system (L1 and L2 lenses). GM-H controls the illumination beam angle in the horizontal direction and is imaged on the sample using another 4F system consisting of L3 and L4 lenses. This 4F system has a demagnification of 8 which makes an angular magnification with the same amount. The sample generates the SH light (green beam in Fig. 4.3(a)) which is imaged using a microscope objective and L5 on the Scientific CMOS camera (Andor Neo 5). On the reference side, an SH Gaussian beam is generated with a lithium-niobate LiNbO3 uniform crystal. Due to the extremely short coherent length of the light source corresponding to 280fs, the optical paths between the reference and signal arms should match. To have that, we use a delay path in the reference arm on a motorized stage to control the optical path of the reference arm. The polarization of the reference SH arm is set to 45-deg in the xy lab system with HW3 to be able to get the interference with both polarization components of the SH signal beam. The reference and signal arms are combined in an off-axis

configuration and their polarization is filtered with P2 in order to get the hologram of the desired output polarization. We consider two output polarization of x and y orientations.

Filtering the SH light is an important issue in the SH holographic setup. In order to completely block the high-power fundamental beam we use a set of spectral filters with the total optical density of OD19. On the reference side, filter F1 drops the intensity of the fundamental beam and also gives us the ability to have some part of the fundamental beam in the case of measurement of E^F and E^I which is possible by removing F3. On the signal side, we have two filters, F2 and F3 which reduce the intensity of the fundamental beam. For the imaging, we use a 60X dry objective (Nikon 60X-PF Plan Fluorite, 0.85 NA, 0.31-40mm WD). The objective is dry but the sample is immersed in water. This issue causes aberrations which can be corrected numerically as we have access to the complex fields holographically.

The desired sample of the study is illuminated with a conical illumination pattern with a maximum angle of $\theta \approx 12^\circ$ and the phase and the amplitude of the light at the SH and fundamental wavelengths are collected for different pairs of input and output polarization. We use this data for the tomographic 3D reconstruction of $\chi^{(2)}$ distribution which we discuss in the next section.

4.3.3 Experimental results on muscle tissue

As mentioned in the introduction, SH-microscopy is a useful label-free and background-free imaging modality for biological samples that include fibrous proteins with endogenous second-order susceptibility, such as collagen and myosin. In this regard, the study of the structure of the muscle fibers, and useful microscopic morphological information about the supramolecular structures of myosin can be accomplished using an SH imaging modality [81]–[83]. As a result, we investigate the viability of our 3D SH-ODT technique for muscle tissue fiber. The sample is a Fresh *ex vivo* cryo-embedded mouse muscle with a 20 μm thickness, fixed with paraformaldehyde (PFA), immersed in water as the background medium, and sandwiched between two #1 cover-slips.

We can see in Fig. 4.3(b-d) the holographic results achieved from SHG by a skeletal muscle fiber. The endogenous $\chi^{(2)}$ distribution of muscle fiber generates the SH field at the $\lambda_{SH} = 515\text{nm}$ which is combined with an SH reference beam on the detector to form the SH-hologram. The 2D Fourier transform of the SH hologram is shown in Fig. 4.3(b). We use Fourier-domain holographic extraction to achieve the amplitude and phase of the SH emission from the muscle fiber as illuminated with a tilted fundamental beam. The amplitude and phase of the complex SH field are shown in Fig. 4.3(c-d). The muscle fiber has been composed of repeating connective units, known as sarcomeres, shown in Fig. 4.3(f), which are arranged periodically along the fiber direction. The periodic structure of sarcomeres can be clearly seen in the amplitude of the SH-emission in Fig. 4.3(c). We take a closer look at this periodic structure of sarcomeres by plotting the profile of the amplitude and phase of the SH emission on the dashed line shown in Fig. 4.3(c). The phase and amplitude plots are presented in Fig. 4.3(e). We

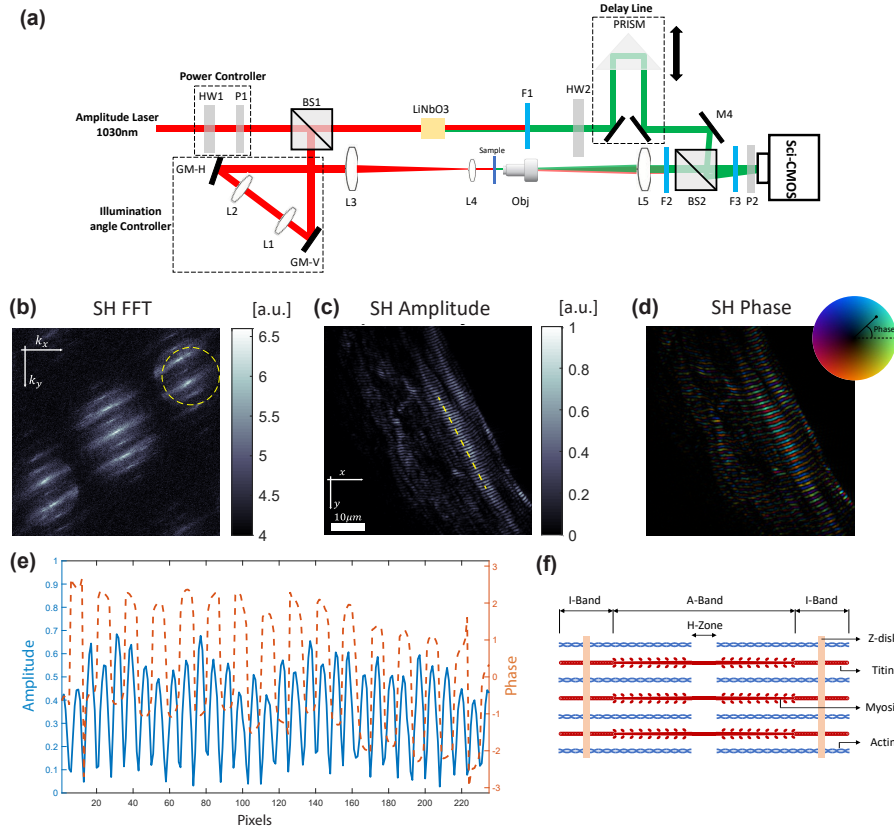


Figure 4.3: (a) Experimental setup for multi-angle SH-holography. (b) Fourier transform of the SH hologram from muscle fiber. (c-d) Holographic extraction of the amplitude and phase of the SH-generated field from the muscle fiber as the sample illuminated with a tilted fundamental Gaussian wave. The amplitude values are normalized and the phase map is shown in the color code of (d) as the brightness is modulated with the amplitude. (e) The 1D profile of the amplitude (blue) and phase (orange) of the SH-generated field along the dashed line is shown in (c). We can see the periodic amplitude and phase variation, amplitude dips between myosin crystals, and $\pm\pi$ jumps in phase. (f) Structure of the muscle tissue sarcomere.

see that the phase of the SH emission has $\pm\pi$ jumps in the dips of the amplitude. This is due to the fact that within a period of the sarcomere, the myosin filaments are mirrored with respect to the H-zone, as clearly demonstrated in Fig. 4.3(f). When a crystal gets mirrored, the $\chi^{(2)}$ values change their sign, which will lead to a π shift in the SH phase profile. This is previously studied by interferometric SH-microscopy [84]. It should be noted that the centro-symmetry implies that the amplitude of the SH emission vanishes at the ends of the sarcomere unit, known as z-disks, and also at the middle of these periodic units. This can be clearly observed in the dips of the amplitude profile of Fig. 4.3(e).

We collect the fundamental and SH holograms by illuminating the sample from 180 different angles and extracting the phase and amplitude of the SH emission and fundamental scattering for each projection. As the target muscle fiber is mainly oriented along the y-direction, the

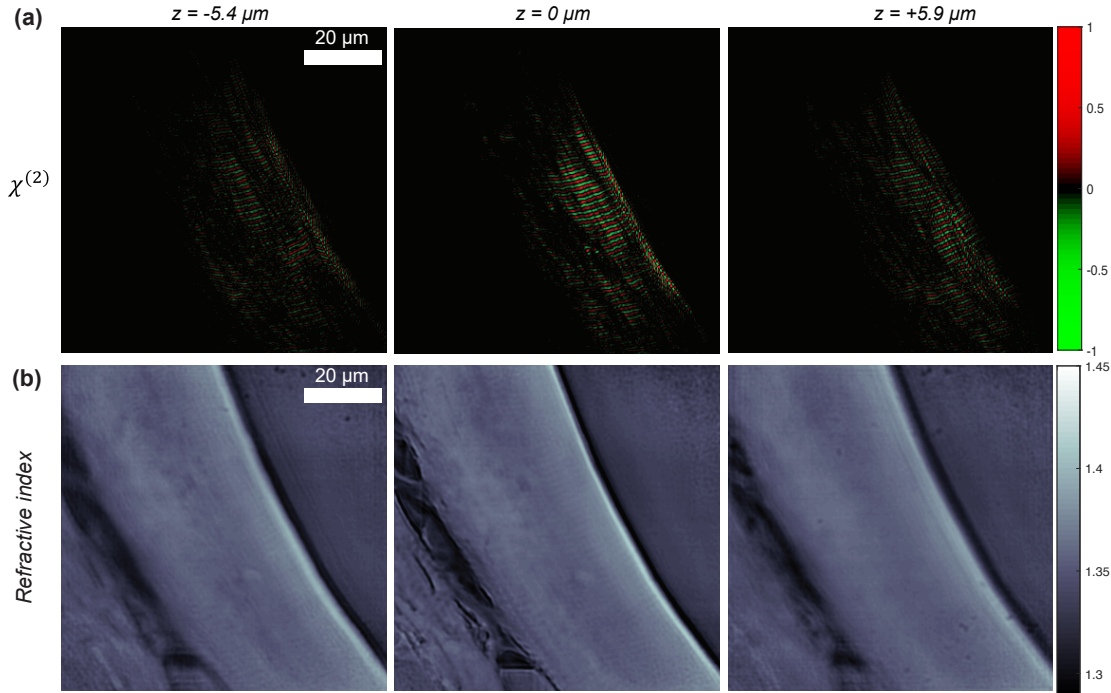


Figure 4.4: SH Tomographic reconstruction. (a) 2D YX profile of the 3D reconstruction of $\chi^{(2)}$ distribution in three different Z planes. The values are normalized to the $[-1, 1]$ range. (b) 2D YX profile of the 3D refractive index reconstruction in three different Z planes.

dominant component in the first column of its $\chi^{(2)}$ -tensor is $\chi_{y1}^{(2)}$ [82]. As a result, we consider the x-polarized illumination and measure the y-polarized complex SH-emission to reconstruct the 3D distribution of the $-21-$ element of the tensor.

The 3D reconstruction of the sample is presented in Fig. 4.4. Fig. 4.4(a) shows the yx profile of the $\chi^{(2)}$ reconstruction in three different z-planes. This figure clearly demonstrates the structure of myosin proteins which are periodically arranged. A 3D reconstruction of the linear refractive index distribution is presented in Fig. 4.4(b) using Rytov approximation [25] with the holographic measurements of the linear scattering at the fundamental wavelength. A visualization of the 3D renderings of the reconstructed $\chi^{(2)}$ and refractive distributions are shown in Fig. 4.5(a-b).

4.4 Discussion

We showed the tomographic reconstruction of the BTO nano-particles with synthetic data and muscle tissue with experimental data in section 4.3. We can observe several aspects in the reconstructions achieved using SH-ODT. The SH-holographic measurements in Fig. 4.3 show very interesting features in the amplitude and phase of the SH signal emitted from the muscle tissue. The $\pm\pi$ phase jumps present details about the morphology of the myosin proteins. Additionally, the strength of the SH emission informs about the thickness of the

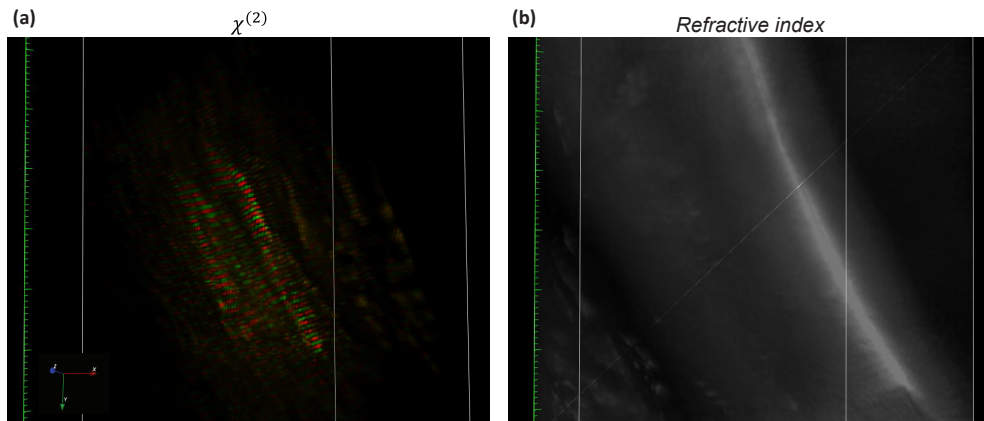


Figure 4.5: (a) 3D rendering of the $\chi^{(2)}$ reconstruction using SH-ODT. (b) 3D rendering of the refractive index reconstruction using linear ODT.

myosin proteins. On the other hand, SH-ODT presents a 3D quantitative reconstruction of $\chi^{(2)}$ of the sample. This imaging modality provides a label-free and background-free 3D image. Comparison of the reconstructed second-order susceptibility and refractive index distributions in Fig. 4.4 shows SH-ODT provides important and interesting features which cannot be seen in the linear ODT. The periodic arrangement of the sarcomeres units can be hardly seen in the linear refractive index reconstruction but with a low resolution and contrast. However, the second-order susceptibility reconstruction presents a detailed image of the muscle tissue fibers.

There are several advantages for SH-ODT in comparison with confocal SH-microscopy. First of all, ODT requires angle scanning and is faster than 3D spatial scanning in confocal microscopy. More specifically about the SHG, SH-ODT can provide a better signal-to-noise ratio due to the presence of the reference beam in the SH-holography. Additionally, the reconstruction is quantitative and shows the 3D distribution of $\chi^{(2)}$. The $\pm\pi$ phase jumps in the SH field and the positive and negative distributions of $\chi^{(2)}$ can be shown in SH-ODT.

Due to the shorter wavelength for the SH signal, the resolution of the SH-ODT is twice better than the conventional ODT, both in the transverse and axial directions. The resolution can be further improved by sample rotation or wavelength scanning. This improved resolution and contrast makes SH-ODT a very useful technique for the reconstruction of biological and non-biological samples containing non-centrosymmetric materials. All of these advantages of SH-ODT are at the expense of a complicated experimental setup and the high-power illumination beam. In the case of our experimental setup presented in Fig. 4.3, we use a light source with $3.5\mu\text{J}$ pulse energy and use 50% of this power to illuminate the sample. Increasing the intensity of the illumination more than in our case could cause several problems such as bubble generation and damaging the imaging objective lens. The required exposure time to capture a high signal-to-noise ratio SH image with our illumination intensity was about 100ms. Nevertheless, the development of high-power lasers and cameras with high quantum

efficiency facilitates the implementation of SH-holography and SH-ODT setups.

We can generalize the methodology of this chapter to other optical nonlinear processes rather than SHG. For non-centrosymmetric materials, we can observe sum-frequency generation if we have two high power sources. In sum-frequency generation, two coherent sources at frequencies ω_1 and ω_2 combine and generate a third frequency, $\omega_1 + \omega_2 \rightarrow \omega_3$. The nonlinear polarizability for this process will be,

$$P_i(r, \omega_3) = \epsilon_0 \chi^{(2)}(r) E_1(r, \omega_1) E_2(r, \omega_2) \quad (4.7)$$

where $E(r, \omega_1)$, and $E(r, \omega_2)$ represent the electric field in two pump frequencies. Considering the scalar regime, the electric field of the sum-frequency generation will be,

$$E^{SFG}(r, \omega_1 + \omega_2) = \int G^{SH}(\mathbf{r} - \mathbf{r}') \cdot E_1 e^{j\vec{k}_{in,1} \cdot \mathbf{r}'} \cdot E_2 e^{j\vec{k}_{in,2} \cdot \mathbf{r}'} \cdot V^{SF}(\mathbf{r}') d\mathbf{r}' \quad (4.8)$$

by inverting Eq. 4.8 using the Fourier diffraction theorem, we can find the sum-frequency scattering potential,

$$V^{SF}(K_x - k_x^{in,1} - k_x^{in,2}, K_y - k_y^{in,1} - k_y^{in,2}, K_z - k_z^{in,1} - k_z^{in,2}) = \frac{K_z}{2\pi j E_1 E_2} \mathcal{F}_{2D}\{E^{SF}\}(K_x, K_y) \quad (4.9)$$

in which K_x and K_y are the Fourier components in the transverse direction, E_1 and E_2 are the amplitude of the fields at frequencies ω_1 , and ω_2 , and $K_z = \sqrt{(k_{SF} n_0^{\omega_3})^2 - K_x^2 - K_y^2}$. Eq. 4.9 shows how the spatial frequency domain of the scattering potential should be filled based on the 2D Fourier transform of the generated nonlinear signal. According to this equation, the phase matching condition is the key point in understanding how different frequencies of the scattering potential contribute to the 2D Fourier transform of the generated signal. If we decompose the generated signal into plane waves in the Fourier domain, the phase-matching condition should be satisfied for the plane wave of $E^{SF}(K_x, K_y)$. The phase-matching condition applies that $\vec{K} = [K_x, K_y, K_z] = \vec{K}_g + \vec{k}^{in,1} + \vec{k}^{in,2}$ where \vec{K}_g is the frequency vector of the corresponding grating in the scattering potential which generates this plane wave of E^{SF} . Considering Eq. 4.9, we can clearly see this phase-matching condition in the way that the frequency components of the scattering potential are filled. As a result, we can simply rewrite this equation for any parametric nonlinear conversion, such as third-harmonic generation or four-wave mixing by taking the phase-matching condition into account for that nonlinear conversion process.

4.5 Conclusion and future work

Concluding, we presented ODT for the second-harmonic parametric conversion and showed 3D reconstructions of the second-order susceptibility of the sample using multiple-angle holographic measurements of SHG. The presented formalism was based on applying the Fourier diffraction theorem for the SH Helmholtz equation. We developed SH-ODT for recon-

structuring the second-order susceptibility based on the first-order Born approximation. The proposed methodology is tested with synthetic examples achieved using FEM. We applied our methodology to a biological example, a muscle tissue fiber, and reconstructed its second-order susceptibility showing various features such as myosin crystals in the sarcomere units of the tissue. The presented SH-ODT shows high-resolution label- and background-free 3D images of details that cannot be revealed in linear ODT or QPI.

The presented work in this chapter has a significant impact on the theory and experiments of ODT and can contribute to developing new modalities for digital-holography-based 3D imaging. There are 3 aspects for SH-ODT to be conducted in the future. Firstly, studying more biological and non-biological samples using SH-ODT. Secondly, developing iterative approaches for SH-ODT based on different forward models such as the nonlinear beam propagation method in order to improve the reconstruction fidelity and avoid artifacts due to the missing-cone problem or multiple scattering, and lastly, generalizing nonlinear ODT to other nonlinear optical processes such as sum-frequency generation, third-harmonic generation, and Coherent Anti-stokes Raman scattering.

5 Iterative ODT using physics-informed deep learning

This work has been published in the following paper [85]:

- A. Saba, C. Gigli, A. B. Ayoub, and D. Psaltis (2022). Physics-informed neural networks for diffraction tomography. *Advanced Photonics*, 4(6), 066001.

A. Saba carried out the algorithm implementation and obtained the results and reconstructions.

5.1 Introduction

In the last years, many different iterative methods have been proposed to reconstruct accurate refractive indices from ill-posed measurements [26]–[28], [35], [86]. The main idea driving iterative approaches is to utilize a forward model that forecasts the potential projections for the current estimation of the refractive index in each iteration. Then, the 2D prediction is compared with the experimental measurements of the projection as a loss function, and the refractive index estimation is adjusted through the minimization of this loss function, incorporating any additional prior knowledge, such as sparsity conditions. Importantly, such an iterative scheme requires an analytical/semi-analytical model in order to backpropagate the computed loss and update the estimation of the refractive index. This precludes the use of common mesh-based numerical solvers like finite difference and finite element methods. In Ref. [26] the authors use a linear (single-scattering) forward model, in the approach proposed in Refs. [27], [28], [86], referred as learning tomography, the forward model is beam propagation method (BPM), and in Ref. [35] the authors resort to the Lippmann–Schwinger equation. In the case of high-contrast samples or multiple-scattering, the forward models employed in these iterative solutions can either be computationally demanding or prone to inaccuracies. As a result, presenting a fast, accurate, and differentiable forward model is necessary to be used in iterative ODT. Physics-informed neural networks (PINNs), can be a good candidate for solving forward scattering problem and being used in iterative tomographic reconstruction.

PINNs have recently gotten intensive research attention for solving different complex problems in physics [87], [88]. These networks use physics laws as the loss function instead of the data-driven loss functions. In conventional supervised deep learning, a large dataset of labeled examples is used for the training process: by comparing the known ground truth with the predictions from a deep multi-layer neural network, one can construct a loss function and tune the parameters of the network in order to solve complex physical problems. Different examples of these data-driven neural networks are proposed for optical applications such as resolution enhancement [89], imaging through multi-mode fibers [90], [91], phase retrieval [92], ODT [29], and digital holography [93], [94]. In these networks, the knowledge acquired by the network strongly depends on the statistical information provided in the dataset, and training such a network requires access to a large dataset. In contrast, PINNs directly minimize the physical residual from the corresponding partial differential equation (PDE) that governs the problem instead of extrapolating physical laws after going through a large amount of examples. In the pioneering approach proposed by Lagaris et al. [95], the neural network maps independent variables, such as spatial and time coordinates, to a surrogate solution of a PDE. By applying the chain rule, for example through auto-differentiation integrated in many deep-learning packages, one can easily extract the derivatives of the output fields with respect to the input coordinates and consequently construct a physics based loss [96]. The correct prediction can be therefore retrieved by minimizing the loss with respect to the network weights. This approach has been used to solve nonlinear differential equations [97]–[100], to realize the forward model in the inverse design of optical components [101], and to extract material parameters in near field microscopy [102].

Having the independent variables of PDE as the input of the neural network limits the use of PINNs when fast inference is required. For the example of optical scattering, the neural network should be trained for each refractive index distribution separately. A different idea was proposed recently in Ref. [103] to solve Maxwell's equations for microlenses with different permittivity distributions. The calculation of physical loss, in this case, is based on the finite difference scheme, and in contrast to the previous approach which is trained for a single example, this model proved to be well-suited for cases in which fast inference is required. However, such a PINN was only demonstrated to work for homogeneous 2D samples.

In this chapter, we extend this idea for inhomogeneous and 3D cases and present a MaxwellNet which is able to solve different forward scattering problems, such as light scattering from biological cells. In the first part of the work, we train MaxwellNet for 2D digital phantoms and show how this pretrained network can be fine-tuned to predict light scattering from more complex and experimentally relevant samples, in our case HCT-116 cells. We benchmark the performance of MaxwellNet in solving scattering problems for 2D and 3D objects. Next, we demonstrate that such PINN can be efficiently used to invert the scattering problem through an iterative scheme and improve the results of conventional ODT. We first demonstrate the reconstruction of the refractive index distribution from synthetic data and then we validate the technique with experimental measurements of scattering from polystyrene microspheres.

5.2 Methodology

In recent years, it has been observed that Artificial Intelligence (AI) can perform tasks in image processing, vision, and natural language processing more effectively than humans. Deep neural networks are a subset of AI algorithms that are built based on the large and deep arrangements of nodes, allowing them to learn based on the statistics provided by the data and extract important features in performing a specific task. In supervised learning, a dataset of input and output pairs is given to the deep neural network, allowing it to learn its parameters in order to predict the output examples as close as possible to the given ground-truth outputs in the dataset. Physics-informed deep neural networks have been proposed as a solution when the output dataset is not directly known but is known to conform to a differential equation. As an example, if we desire to implement a deep neural network that predicts optical scattering, in the data-driven approach we can create a dataset of input topology and output scattered lights using a numerical optical solution and train the neural network with this dataset. On the other hand, we know that optical scattering follows Maxwell's equations which can be used as a physics-informed loss function to train the deep neural network. This is the idea of a physics-informed neural network for optical scattering.

Fig. 5.1 summarizes the main concept of our work, which consists of two blocks. The first, MaxwellNet, is a neural network that takes as an input the refractive index distribution $n(\mathbf{r})$ and predicts the scattered field U^s . Its structure is based on the U-Net architecture [104], and the training is performed on a large dataset of digital phantoms using a physics-defined loss function. Then, this network is used as a forward model in a second optimization task which compares the fields predicted by MaxwellNet for a candidate RI distribution with the ground-truth projections, e.g. computed numerically or evaluated experimentally, and updates $n(\mathbf{r})$ up to convergence.

5.2.1 Forward Model: MaxwellNet

This subsection explains the implementation of a PINN that predicts the scattered field given a known input RI distribution. Initially, we present the method for the 2D scenario for simplicity; however, we will elaborate on the extension to 3D in the following section. In this case, MaxwellNet takes as an input the RI distribution as a discrete array of shape $N_x \times N_z \times 1$ and we do expect an output with size $N_x \times N_z \times 2$, where the two channels correspond to the real and imaginary parts of the complex field. Among all the available architectures, the choice of U-Net appears favorable as we do expect to embed the latent features of the RI distributions in a lower dimensional space through consecutive 2D convolutions and then retrieve the complex electromagnetic field in the same spatial points through the decoding step. A similar architecture was also proven to provide good accuracy for the computation of the scattered field from microlenses [103]. We implement the present network in TensorFlow 2.6.0. For each step in the encoder, we use two Conv2D layers, each followed by batch-normalization and *elu* activation function. A total number of five layers is adopted to encode the information and

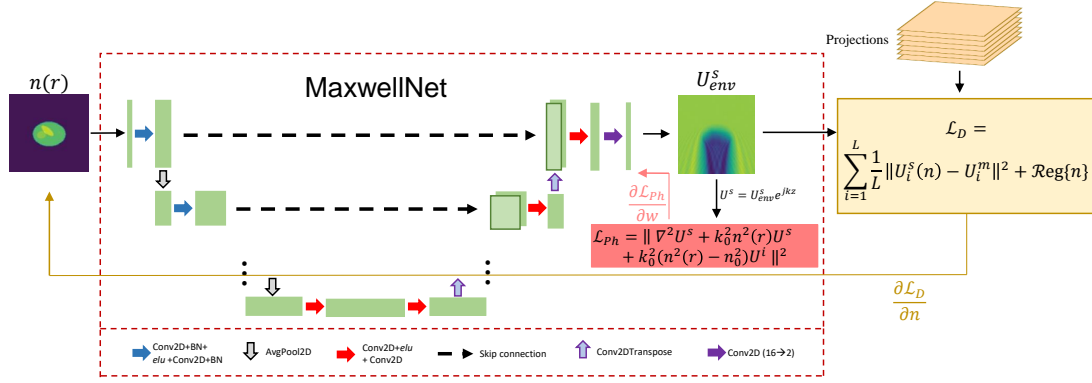


Figure 5.1: Schematic description of MaxwellNet, with U-Net architecture, and its application for tomographic reconstruction. The input is a refractive index distribution and the output is the envelope of the scattered field. The output is modulated by the fast-oscillating term $e^{jk_0 n_0 z}$ to compute the physics-informed loss for tuning the weights. To perform tomographic reconstruction, we employ MaxwellNet to minimize a data-driven loss that quantifies the disparity between measured and predicted projections. The addition of a regularization term can improve the reconstruction.

each one is terminated with average pooling to reduce the dimension. The maximum number of channels that we get in the latent space is 512. On the decoder side, we used transposed convolutional layers to the output with the size $N_x \times N_z \times 2$ (or $N_x \times N_y \times N_z \times 2$ in the 3D case). It should be noted that we also use residual skip connections from the encoder branch. In common data-driven training, we would tune the weights of this network by minimizing the difference between predictions and ground-truth data computed with numerical solvers, in turn requiring a large database of simulations and consequently a massive computational cost. Here we do not provide input-output pairs, instead, we train the network by requiring that the Helmholtz equation is satisfied on the predicted field. In order to speed up the training and improve performance, we require the network to predict the slowly varying envelope of the scattered field U_{env}^s being the scattered field obtained after demodulated by the fast-oscillating component along propagation direction $U^s = U_{env}^s e^{jk_0 n_0 z}$. The physics-informed loss function to be minimized by updating the weights of the network is as follows:

$$\mathcal{L}_{Ph} = \sum_r \frac{1}{N} \left\| \{\nabla^2 + k_0^2 n^2(r)\} U^s + k_0^2 (n^2(r) - n_0^2) U^i \right\|^2 \quad (5.1)$$

where, k_0 is the wave-number which is $k_0 = 2\pi/\lambda$ and $\lambda = 1.030\mu m$ is the wavelength. $n(r)$ is the RI distribution and n_0 is the RI of the background medium. The summation in Eq. (5.1) is done over the pixels of the computational domain and N is the number of pixels. In order to implement the Laplacian in Eq. (5.1), we follow the Yee grid finite difference scheme, computing the derivative of variables by 2D convolutions with a 5×5 kernel [105]. Additionally,

light scattering is by definition an open boundary problem. In order to satisfy the Sommerfeld radiation condition and confine the problem in a finite space we use a stretched-coordinate perfectly-matched layer (PML) [106] at the edges of the simulation domain by introducing a complex coordinates transformation ($x \rightarrow x + if(x)$) when calculating the derivatives inside the PML region. We use the gradient of the so-computed physical loss function to update the weights of the neural network, w through the Adam optimizer:

$$w \rightarrow w - \gamma_{Ph} \frac{\partial \mathcal{L}_{Ph}}{\partial w} \quad (5.2)$$

When we train MaxwellNet for a class of samples, it can accurately calculate the field for unseen samples from the same class. However, the key point to mention is that if we want to use MaxwellNet for a different set of RI distributions, we can fix some of the weights, and adjust only a part of the network for the new dataset, instead of re-starting the training from scratch. This process, referred to in the following as fine-tuning, is much faster than the original training of MaxwellNet. We will elaborate on and discuss this interesting feature in section 5.3.

It should be mentioned that we train MaxwellNet based on the Helmholtz equation with scalar field approximation, as described in Eq. 5.1. The scalar approximation allows us to have a network with 2-channel output, representing the real and imaginary of the scalar field. We can also consider the full-vectorial Helmholtz equation where we need a larger network with 6-channel output to represent the real and imaginary of the three components of the field vector. However, the depolarization term can be neglected for samples with low refractive index gradients[80], [107], allowing us to have a MaxwellNet with fewer parameters and the scalar Helmholtz equation as the loss function.

5.2.2 Optical diffraction tomography using MaxwellNet

Once MaxwellNet has been trained on a class of RI distributions, it can be used to rapidly backpropagate reconstruction errors with an approach similar to learning tomography [27]. Let us assume that we measure L projections U_i^m , with $i = 0, \dots, L$, from an unknown RI distribution $\bar{n}(x, z)$ for different rotational angles. From these data, we can reconstruct a first inaccurate candidate $n(x, z)$ through Wolf's transform using Rytov approximation. Then, we need to calculate the projections by MaxwellNet for different illumination angles. To implement illumination angle rotation, we can geometrically rotate $n(x, z)$ based on the corresponding illumination angle and calculate the scattered field for the rotated refractive index. By feeding MaxwellNet with $n_i(x, z) = \mathcal{R}_i\{n(x, z)\}$, where \mathcal{R}_i is the image rotation operator corresponds to the i -th projection, we predict the complex scattered fields U_i^s for the same L angles. Consequently, we can construct a data-driven loss function \mathcal{L}_D given by the difference $\|U_i^s - U_i^m\|^2$ plus any additional regularizer, compute its gradient through auto-differentiation, update $n(x, z)$ and iterate up to convergence:

$$\mathcal{L}_D = \sum_{i=1}^L \frac{1}{L} \|U^s(\mathcal{R}_i\{n\}) - U_i^m\|^2 + \mathcal{R}eg\{n, U^s(n)\} \quad (5.3)$$

$$n \rightarrow n - \gamma_D \frac{\partial \mathcal{L}_D}{\partial n} \quad (5.4)$$

Also in this case, we use Adam optimizer for updating RI values. The regularizer in Eq. (5.3) consists of three parts, a total-variation (TV), a non-negativity and a physics-informed terms, $\mathcal{R}eg\{n, U_i^s(n)\} = \lambda_{TV} \mathcal{R}_{\mathcal{T}V}(n) + \lambda_{NN} \mathcal{R}_{\mathcal{N}\mathcal{N}}(n) + \lambda_{Ph} \mathcal{L}_{Ph}(n, U^s)$. The TV regularizer helps smoothing the RI reconstruction and the non-negativity regularizer adds the prior information that $n(x, z)$ should be larger than the background refractive index:

$$\mathcal{R}_{\mathcal{T}V}(n) = \sum_r \sqrt{|\nabla_x n(r)|^2 + |\nabla_y n(r)|^2 + |\nabla_z n(r)|^2} \quad (5.5a)$$

$$\mathcal{R}_{\mathcal{N}\mathcal{N}}(n) = \sum_r \min(n(r) - n_0, 0)^2 \quad (5.5b)$$

Importantly, we have to remark that MaxwellNet is trained for a specific dataset and accurately predicts the scattered field for RI distributions that are not too far from this set. To take into account this effect we add the physics-informed loss to the regularizer. This further correction term helps to find RI values in a way that MaxwellNet can predict the scattered field for them correctly. In contrast to TV and non-negativity constraints that are used due to the ill-posedness of the ODT problem, the physics-informed regularizer is necessary in our methodology to ensure that the index distributions remain within the domain in which MaxwellNet has been trained.

The key advantages of using MaxwellNet with respect to other forward models are three folds: differently from BPM, it can accurately calculate field scattering, considering reflection, multiple-scattering, or any other electromagnetic effects [26]–[28], [86]; once trained, the field computations are performed in milliseconds, much faster than Lipmann-Schwinger model; and finally, the data-driven error in Eq. (5.3) can be easily backpropagated differently from commercially available full-vectorial solvers. We discuss the reconstruction results and compare them with other methods in subsection 5.3.2.

5.3 Results and Discussion

5.3.1 MaxwellNet results

In this subsection, we evaluate the performance of MaxwellNet for the prediction of the scattered field from RI structures such as biological cells. At first, we check the performance on a 2D sample assuming that the system is invariant along the y axis. The number of pixels for our model are $N_x = N_z = 256$ for both the x and z directions, and their size is $dx = 100\text{nm}$. We also use PML with the thickness of $1.6\mu\text{m}$ at the edges of our computational domain. We create a dataset of digital cell phantoms and divide it into the training and testing sets. MaxwellNet has $\sim 5.9\text{M}$ parameters to train and we use the Adam optimizer with a learning rate of 1×10^{-4} and batch training. The details about the dataset and training and validation losses are discussed in Appendix C.2. We train and test MaxwellNet in Tensorflow 2.6.0 on a desktop computer (Intel Core i7-9700K CPU, 3.6GHz, 64GB RAM, GPU GeForce RTX 2080Ti).

In Fig. 5.2(a) and Fig. 5.2(b), we choose two random examples of the digital phantoms in the test set (which is not seen by the network during the training). For each test case, in the second and third rows, we present the prediction of the envelope of the scattered field by the network, and we compare it with the result achieved by the finite element method (FEM) using COMSOL Multiphysics 5.4. We can see a very small difference between the results of MaxwellNet and COMSOL, which we attribute to discretization error. There are different schemes of discretization in two methods that can cause such differences. In order to quantitatively evaluate the performance of MaxwellNet, we define the relative error of MaxwellNet with respect to COMSOL as,

$$error = \frac{\int \|U_{MaxwellNet}(r) - U_{COMSOL}(r)\|^2 dr}{\int \|U_{COMSOL}(r)\|^2 dr} \quad (5.6)$$

where $U_{MaxwellNet}$ and U_{COMSOL} are the total fields calculated with MaxwellNet and COMSOL. The integration is done excluding the PML regions. The calculated relative errors for the test case 1 and the test case 2 in Fig. 5.2 are 4.1×10^{-2} and 4.6×10^{-2} , respectively.

It should be noted that once MaxwellNet is trained, the scattered field calculation is much faster than numerical techniques such as FEM. We present a time comparison in Table 5.1. For the test phantoms in Fig. 5.2, it took 17ms for MaxwellNet in comparison with 13s for COMSOL meaning three orders of magnitude acceleration.

Furthermore, performing physics-based instead of direct data-driven training holds promises for exploiting the advantages of Transfer learning[108]. Maxwell equations are general but having a neural network that predicts the scattered field for any class of RI distribution in milliseconds with a negligible physical loss is usually unfeasible. Most of the previous PINN studies for solving partial differential equations are trained for one example, and they will work for that specific example. In our case, U-Net architecture proved to be expressive enough

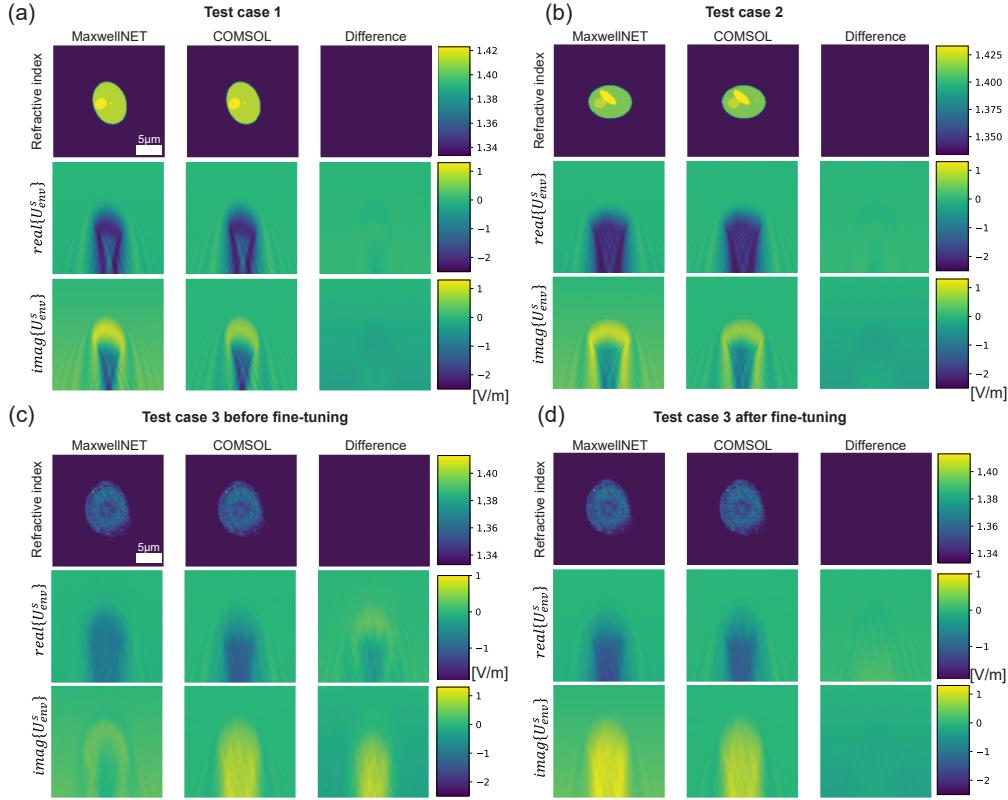


Figure 5.2: Results of MaxwellNet and its comparison with COMSOL. (a,b) Two test cases from the digital phantom dataset and the prediction of the real and imaginary of the envelope of the scattered fields using MaxwellNet, COMSOL, and their difference. (c) Scattered field predictions from the network trained in (a,b) for the case of an experimentally measured RI of HCT-116 cancer cell and comparison with COMSOL. The difference between the two is no longer negligible. (d) Comparison between MaxwellNet and COMSOL after fine-tuning the former for a set of HCT-116 cells. MaxwellNet predictions reproduce much more accurate results after fine-tuning.

to predict the field for a class of samples. However, if we use MaxwellNet for inference on a RI distribution completely uncorrelated with the training set, the accuracy drops. In order to evaluate MaxwellNet extrapolation capability, we considered the model trained on phantoms samples in Fig. 5.2 and use it for inference on HCT-116 cancer cells. The comparison between MaxwellNet and COMSOL is shown in Fig. 5.2(c). The input of the network is a 2D slice of the experimentally-measured HCT-116 cell in the plane of best focus. The discrepancy between MaxwellNet and COMSOL is due to the fact that the former does not see examples of such RI distributions during the training. As a result, if we require accurate results for a new set of samples with different features, we have to re-train MaxwellNet for the new dataset, which would take a long time as reported in Table 5.1. However, it turns out that learning a physical law, as Maxwell equations, even though on a finite dataset is better suited than

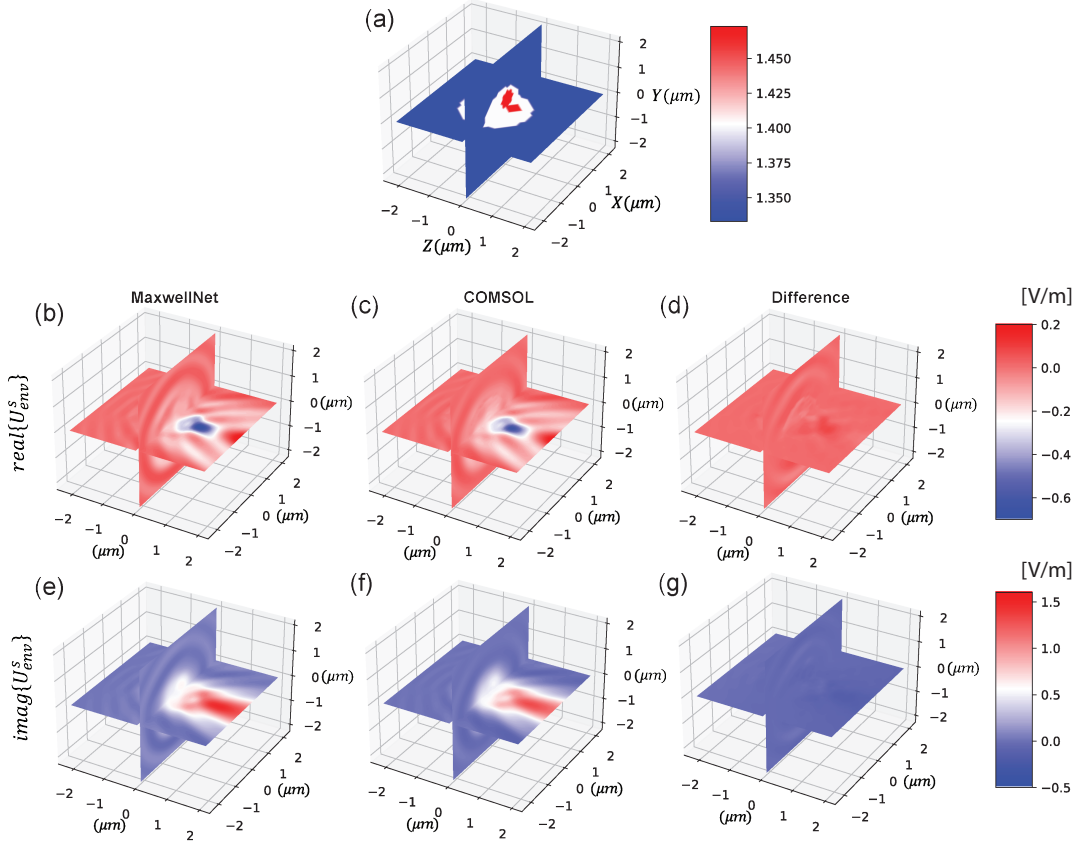


Figure 5.3: Results of MaxwellNet3D and its comparison with COMSOL. The RI distribution is shown in (a). The real part of the envelope of the scattered field calculated by MaxwellNet3D is shown in (b), calculated by COMSOL in (c), and their difference in (d). The imaginary part of the envelope of the scattered field calculated by MaxwellNet3D, COMSOL, and their difference are presented in (e-g), respectively.

data-driven training for transfer learning on new batches. Indeed, we can use the pretrained MaxwellNet on digital phantoms and fine-tune some parts of the network for HCT cells to achieve good convergence in a few epochs. In this example, we create a dataset of 136 RI distributions of HCT-116 cancer cells and divide them into training and validation sets. Some examples of HCT-116 refractive index dataset are shown in Appendix C.2. A wide range of cells with different shapes is included in the dataset. We have single cancer cells, like Fig. 5.2(c), examples of cells in the mitosis process, or examples with multiple cells. In this case, we freeze the weights of the encoder part and fine-tune the decoder with the new dataset. We can see in Fig. 5.2(d) that after this correction step, the calculated field is much more accurate. As it can be seen in Table 5.1, the fine-tuning process is two orders of magnitude faster than complete training from scratch.

The 2D case is helpful for demonstrating the method and rapidly evaluating performance.

Nevertheless, full 3D fields are required for many practical applications. We can straightforwardly recast MaxwellNet in 3D using arrays of size $N_x \times N_y \times N_z \times 1$ as inputs of the network and requiring a $N_x \times N_y \times N_z \times 2$ output, with the two channels corresponding to the real and imaginary of the envelope of the scattered field. In this case, the network consists of Conv3D, AveragePool3D, and Conv3DTranspose layers instead of 2D counterparts. As a benchmark test, we created a dataset of 3D phantoms with 200 examples (180 for training and 20 for testing). The computational domain is defined with $N_x = N_y = N_z = 64$, $dx = 100\text{nm}$, and PML thickness of $0.8\mu\text{m}$. In order to show the proof of concept of 3D MaxwellNet with limited computational resources, we used a lower number of pixels per dimension with respect to the 2D case, keeping the pixel size, dx , the same to have an accurate finite difference calculation. As a result, we have a limited computational domain size, which can be improved using more powerful resources.

The 3D version of MaxwellNet has $\sim 17.2\text{M}$ parameters. We use Adam optimizer (learning rate = 1×10^{-4}), and a batch size of 10. The results of the predicted field for an unseen example and its comparison with COMSOL are shown in Fig. 5.3. We can see that MaxwellNet performs as good as COMSOL in field calculation. The quantitative error described in Eq. 5.6 is 3.4×10^{-3} for the 3D example of Fig. 5.3. There are some marginal differences due to different discretization schemes. However, we can see in Table 5.1 that MaxwellNet is about 50000 faster than COMSOL in predicting fields (44.9 milliseconds versus 41.2 minutes). This result and the significant efficiency in the computation time highlight MaxwellNet potential for the calculation of the field in different applications. In the next subsection, we demonstrate how this method can be applied for improving ODT reconstruction fidelity.

5.3.2 Tomographic reconstruction results

To show the ability of MaxwellNet to be used for different imaging applications, we implement an optimization task with MaxwellNet as the forward model for ODT as explained in subsection 5.2.2. In this example, we consider one of the digital phantoms in the test set of Fig. 5.2 and we use 2D MaxwellNet as the forward model to compute the 1D scattered field along the transverse direction x for $N = 81$ different rotation angles θ . We restrict ourselves to the range

Table 5.1: MaxwellNet computation time comparison

Dataset	2D Phantoms (Training)	2D HCT-116 (Fine-tuning)	3D Phantoms (Training)
Training details	2700 samples 5000 epochs	122 samples 600 epochs	180 samples 5000 epochs
MaxwellNet training/fine-tuning	30.5h	0.18h	15.5h
MaxwellNet inference	17.0ms	17.0ms	44.9ms
COMSOL	13s	13s	2472s

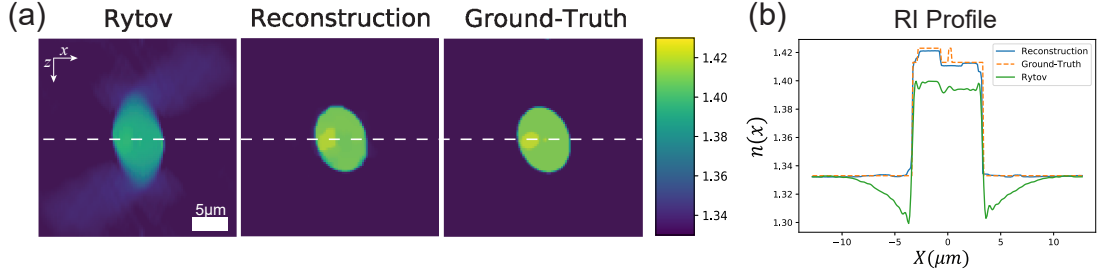


Figure 5.4: Tomographic reconstruction of RI using MaxwellNet. (a) The RI reconstruction was achieved by Rytov, MaxwellNet, and the ground-truth. (b) 1D RI profile at $z = 0$ (plane of best focus), for Rytov (green), MaxwellNet (blue), and the ground-truth (orange).

$\theta \in [-40^\circ, 40^\circ]$ as this is consistent with the typical conditions in common tomographic setups. As is shown in Fig. 5.4(a), the Rytov reconstruction obtained from these field projections is elongated along z -axis and underestimated due to missing frequencies. We then minimize the loss function (5.3) to improve the RI reconstruction choosing as regularizer parameters $\lambda_{TV} = 3.1 \times 10^{-7}$, $\lambda_{NN} = 1 \times 10^{-1}$, $\lambda_{Ph} = 5 \times 10^{-2}$ and Adam optimizer with initial learning rate of 3×10^{-4} . We also scheduled the learning rate, halving it every 1000 epochs to speed-up convergence. The resulting RI distribution after 3000 epochs is shown in Fig. 5.4. It can be seen that the reconstructed RI is not anymore underestimated nor elongated along the z -axis. This is a significant improvement in comparison with Rytov prediction. The missing details in the reconstructed RI, which can be better visible in the 1D cutline in Fig. 5.4(b), can be due to the missing information in 1D fields that the optimization of RI could not retrieve this information.

Next, we try a 3D digital phantom from the test set and we use 3D MaxwellNet as the forward model in our tomographic reconstruction method. Since generating synthetic data with COMSOL is time-consuming for multiple angles, we create synthetic scattered fields from the phantom with the Lippmann–Schwinger equation [35]. We will show later an experimental example, where we illuminate the sample with a circular illumination pattern with an angle $\approx 10^\circ$. As a result, in this numerical example, we rotate the sample for 181 angles (including 1 normal incidence), equivalently to an illumination rotation with a fixed illumination angle of 10° . We keep the experimental conditions, $\lambda = 1.030 \mu\text{m}$, and $n_0 = 1.33$. Then, we use these synthetic measurements for our optimization task along with TV, non-negativity, and physics-informed regularization. The reconstruction is achieved after 6000 epochs with $\lambda_{TV} = 1.2 \times 10^{-8}$, $\lambda_{NN} = 2 \times 10^1$, and λ_{Ph} started with 5×10^{-1} and divided by two every 500 epochs. The reconstructions are shown in Fig. 5.5 in YX, YZ, and XZ planes. The first row shows the Rytov reconstruction where we can see a significant underestimation and elongation along z -axis which is due to the small illumination angle (10°). The details in the reconstruction achieved using MaxwellNet are slightly blurred in comparison with the ground-truth as a result of low resolution with $\lambda = 1.030 \mu\text{m}$.

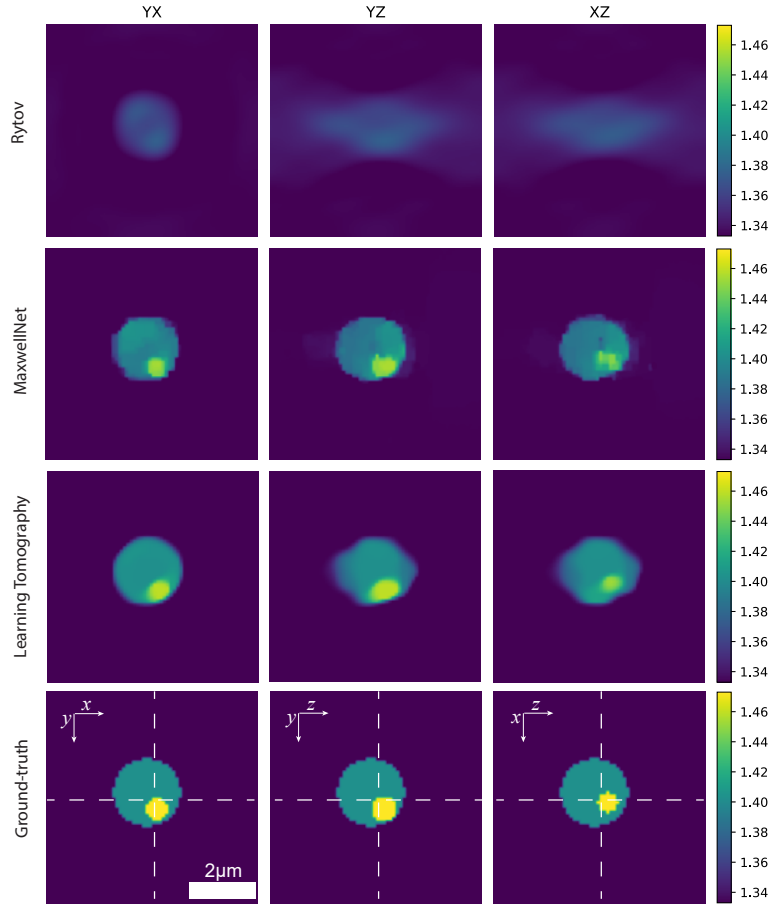


Figure 5.5: Tomographic RI reconstruction of 3D sample using MaxwellNet. The RI reconstruction is achieved by Rytov, MaxwellNet, Learning tomography, and the ground-truth in different rows at YX, YZ, and XZ planes in the center of the sample.

Additionally, we performed Learning tomography[27] for the synthetic measurements using 181 projections. The 3D tomographic reconstruction using Learning tomography is shown in the third row of Fig. 5.5. In comparison with MaxwellNet, Learning tomography has some elongated artifacts which can be due to the fact that reflection is neglected in its forward model. However, the reconstruction with Learning tomography is smoother in comparison with the reconstruction of MaxwellNet which is slightly pixelated. The problem arises due to the fact that the beam propagation method, which serves as the forward model in Learning tomography, is a smooth forward model with respect to the voxels of the refractive index distribution. However, this is not the case for deep neural networks like MaxwellNet. However, the reconstructions are quantitatively comparable. If we assume the reconstruction error of $\varepsilon(n_{recon}, n_{truth}) = \|n_{recon} - n_{truth}\|_2^2 / \|n_{truth} - n_0\|_2^2$, we get the error of 0.613 for Rytov, the error of 0.146 for Learning tomography, and the error of 0.116 for MaxwellNet reconstructions, shown in Fig. 5.5. In terms of computation time with the desktop specifications we mentioned

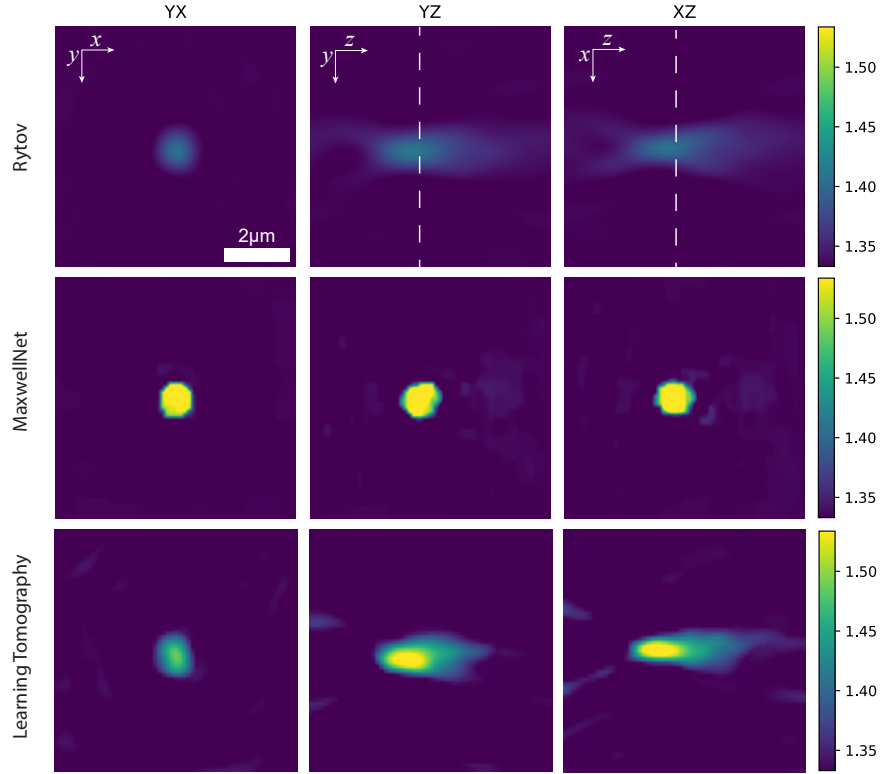


Figure 5.6: Tomographic RI reconstruction of a polystyrene micro-sphere immersed in water. The projections are measured with off-axis holography for different angles. The RI reconstruction achieved by Rytov, MaxwellNet, and Learning tomography are presented at YX, YZ, and XZ planes in the center of the sample.

earlier, we used 3000 epochs for iterative optimization with MaxwellNet, each epoch taking 570ms and 600 epochs for Learning tomography, each epoch taking 710ms, which means a four-fold factor for MaxwellNet in the computation time.

We conducted experimental evaluations of our methodology. As mentioned earlier, MaxwellNet handles reflection as a forward model, making our reconstruction technique suitable for samples with high contrast. In our experimental analysis, we try a polystyrene micro-sphere immersed in water, where we expect to have a ~ 0.25 refractive index contrast. Polystyrene micro-spheres (Polybead® Polystyrene 2.0 Micron) are immersed in water and placed between two #1 glass coverslips. We have an off-axis holographic setup where we use a yttrium-doped fiber laser (Amplitude Laser Satsuma) with $\lambda = 1.030\mu\text{m}$ and we change the illumination angle with two Galvo mirrors. Using a delay path, the optical length of the reference and signal arms are matched. We measure holograms for 181 illumination angles and extract the phase and amplitude of the complex scattered fields using Fourier holography. More details about the experimental setup are discussed in Appendix C.3. Then, we use the extracted scattered fields for different projections for our optimization task to reconstruct the 3D RI distribution of the

sample. The experimental projections are 2D complex fields that are imaged in the center of the sample using a microscope objective lens and we can propagate them in the background medium to calculate the scattered field in any other plane, perpendicular to z -axis, after the sample. This 2D field can be compared with the output of MaxwellNet in that plane, as described in Eq. 5.3. Additionally, the experimental projections are based on illumination rotation and we interpolate them to achieve the equivalent sample rotation projections. We iteratively optimize the loss function in Eq. 5.3 for 2000 epochs where we use the regularization parameters of $\lambda_{TV} = 3.8 \times 10^{-9}$, $\lambda_{NN} = 5 \times 10^1$, and λ_{Ph} started with 1.5×10^{-1} and divided by two in every 500 epochs. The reconstruction is shown in Fig. 5.6 using Rytov, MaxwellNet, and Learning tomography. It can be seen that the underestimation and z -axis elongation in the Rytov reconstruction is remarkably improved. The reconstruction using Learning tomography in Fig. 5.6 has artifacts due to the high refractive index contrast of the polystyrene bead and reflections that cannot be considered in the beam propagation method.

5.4 Nonlinear MaxwellNet

Recently, our group had another extension of MaxwellNet to consider the nonlinear polarizability [109]. The idea of this work is to add the nonlinear polarizability based on the third-order Kerr nonlinearity into the Helmholtz equation and minimized the nonlinear Helmholtz equation as the physical loss function of the PINN. In this regard, the refractive index in the physical loss (Helmholtz equation) is modulated with the input intensity and the input intensity is entered into the deep neural network using a fully-connected layer. This way, a tunable U-Net is predicting the optical scattering in the presence of the Kerr nonlinearity.

Although the presented nonlinear MaxwellNet predicts the optical scattering for the intensity-dependent refractive index based on third-order optical nonlinearity, a similar approach can be implemented for other nonlinear processes such as SHG. Such an approach can be used for inverse SHG problems such as SH-ODT which was discussed in chapter 4. For this case, a deep neural network is given with the 3D refractive index and second-order susceptibility distributions as well as the illumination intensity and polarization state as inputs and predicts the fundamental and SH fields in the computational domain using two nonlinear Helmholtz equations at the fundamental and SH wavelengths as the physics-informed loss function. Such an SH-MaxwellNet can be used as a surrogate forward model in an iterative reconstruction of SH-ODT. The power of PINNs is that they can calculate the forward physics rapidly in any scenario and can be used in an iterative approach for any linear or nonlinear inverse problem due to the availability of the gradients of the output values with respect to the input variables.

5.5 Conclusion

In summary, we have introduced a PINN that can efficiently calculate the scattered field from inhomogeneous RI distributions, such as those found in biological cells. Our network is

trained by minimizing a loss function based on Maxwell equations. We have demonstrated that the network can be trained on a set of samples and used to predict the scattered field for unseen examples within the same class. Since our PINN is not a data-driven neural network, it can be trained for various examples under different conditions. Although the network may not extrapolate efficiently to classes that differ significantly from the training dataset, we have shown that freezing the encoder weights and fine-tuning the decoder branch can yield a new predictive model in a few minutes. We believe this approach could also be used for modification of other physical parameters such as wavelength, or boundary condition.

To recover the RI distribution from scattered fields obtained by illuminating a sample from different illumination angles, an imaging method known as optical diffraction tomography, we employed our PINN as a forward model in an optimization loop. This example highlights the ability of MaxwellNet to be used as a forward model for inverse scattering or inverse design problems using iterative approaches.

6 Conclusion and future work

6.1 Summary of the results

This thesis explores new modalities for optical diffraction tomography and how we can use other linear and nonlinear optical contrast agents such as birefringence and nonlinear susceptibility for ODT.

In chapter 2, we presented the theoretical background and principles of light scattering in inhomogeneous media, in anisotropic media, and in nonlinear media. The mathematical formalism for light scattering in inhomogeneous media was proposed using first-order Born and Rytov approximation, and the inverse scattering is analyzed based on these approximations using the Fourier diffraction theorem. We also discussed polarization of light and light interaction in polarization-sensitive media and nonlinear optical processes such as frequency mixing and harmonic generation.

Chapter 3 studies polarization-sensitive ODT. The focus of this chapter is on vectorial ODT which is based on the inversion of the vectorial light scattering from inhomogeneous samples, specifically for birefringent samples. The proposed method utilizes vectorial scattered fields for multiple illumination angles to reconstruct the 3D refractive index tensor. These vectorial fields are obtained through holographic measurements under varying polarization states of the illumination. To validate the theoretical concepts discussed, a numerical example based on vectorial-BPM is presented. The numerical example presented in this chapter demonstrates the feasibility and effectiveness of the proposed method for polarization-sensitive ODT. The experimental methodology is also described in detail. Finally, the 3D refractive index tensor is reconstructed for mouse muscle tissue. The reconstruction of the 3D refractive index tensor using vectorial scattered fields for multiple illumination angles has several advantages. Firstly, the technique provides a more accurate representation of the sample by considering its anisotropic properties. Secondly, the 3D reconstruction of the refractive index tensor reveals features that are not highlighted in the scalar refractive index distribution. The reconstructed 3D refractive index tensor for the muscle tissue fibers provides valuable insights into the tissue's microstructure. Additionally, we discuss contrast agents that are calculated based on

the eigenvalue analysis of the reconstructed refractive index tensor in order to present 3D reconstructions that are inherently dependent on the sample. The proposed technique has potential applications in biomedical imaging and can aid in the diagnosis and treatment of various biological issues.

In Chapter 4, we provided a detailed analysis of SH-ODT, from both theoretical and experimental viewpoints. This chapter presents the tomographic reconstruction of the 3D second-order susceptibility tensor using 2D measurements of SH-generated fields at the double frequency for different illumination angles and polarization states. This novel method is inspired by conventional linear ODT and has been generalized for the nonlinear SH scenario. The mathematical formalism is based on the nonlinear Helmholtz equation and uses the same tricks of chapter 3 to handle the tensorial reconstruction. To measure the SH-generated complex fields, we used a multi-angle harmonic holography setup. Our technique is particularly useful for samples with Centro-asymmetric features, which is necessary for the sample to have a second-order susceptibility and generate the SH light. By retrieving the SH-generated complex fields with Fourier holography, and reconstructing the 3D distribution of the second-order susceptibility we can provide a background-free imaging technique that highlights features of interest possessing asymmetry at the molecular level. We presented synthetic and experimental results for BTO nanoparticles and muscle tissue fibers to demonstrate the viability of our theoretical formalism and 3D reconstruction methods. Our results demonstrate a new modality for ODT that can potentially be used in various applications. This technique can acquire high-resolution and high-contrast 3D images of biological samples, revealing their structural and morphological characteristics.

Chapter 5 investigates physics-informed neural networks for optical scattering from inhomogeneous samples and uses them as forward models for the inverse scattering problem in ODT. Accurately predicting optical scattering in a non-uniform 3D refractive index distribution is crucial for using the forward model in the iterative reconstruction process of ODT. Iterative methods used in ODT begin with an initial estimation of the 3D refractive index. The forward model is then utilized to compute the scattered fields for each illumination angle, which are compared with the actual measurements to derive a loss function. This loss function is minimized iteratively by modifying and updating the 3D refractive index distribution until the correct 3D refractive index distribution is achieved. This chapter introduced a PINN named MaxwellNet, designed to solve 3D optical scattering, and used it as a forward model in an iterative reconstruction for ODT. The proposed PINN is a deep convolutional neural network that takes the 3D refractive index array as the input array and provides the 3D scattered light at the output array. Using synthetic examples, we trained and tested MaxwellNet and provided numerical examples to validate the forward scattering problem. Synthetic results achieved using Lippmann–Schwinger equation and experimental results measured using off-axis holography are exploited to investigate the ability of MaxwellNet for the inverse scattering problem of ODT. The results of chapter 5 show how PINNs can be powerful in inverse problems.

Both polarization-sensitive and SH ODT techniques provide 3D distribution of the quantitative

modalities that cannot be imaged using other imaging methods. These modalities for ODT enable label-free 3D imaging of biological and non-biological samples. Both of these methods are based on the inversion of the vectorial or nonlinear variations of the Helmholtz equation and it can be challenging to be fully studied or be generalized. This is where PINNs or other deep neural networks can play a role in accurately and quantitatively inverting optical scattering and frequency generation.

6.2 Future work

In this thesis, several aspects of optical diffraction tomography were studied which could be the topic of future work.

The polarization-sensitive chapter should be continued in the biology direction in order to explore more interesting biological features that can be revealed in this 3D imaging modality. On the other hand, it is desirable to present new ideas in the physical and algorithm directions. As described in chapter 3, there were several approximations that will degrade the accuracy of the presented technique to provide a quantitatively accurate reconstruction of the 3D refractive index tensor. Better physical models to evaluate light propagation in anisotropic inhomogeneous media and iterative approaches for reconstructing the full 3×3 inhomogeneous refractive index tensor should be studied. Moreover, building polarization-sensitive multi-angle holographic setups can be challenging, and intensity-based iterative techniques are helpful to reconstruct the complete refractive index tensor using cross-polarized intensity or Mueller matrix measurements.

SH-ODT has many different directions to be addressed in the future. The first direction is to investigate more biological and non-biological samples using SH-ODT to broaden its application scope. The background-free property of this ODT modality can elaborate important features in biological studies. The second direction is to improve the accuracy of the reconstruction and eliminate artifacts caused by the missing-cone problem or multiple scattering by developing iterative approaches for SH-ODT. This can enhance the reliability and efficacy of the SH-ODT technique. Lastly, SH-ODT can be extended to other nonlinear optical processes such as sum-frequency generation, and third-harmonic generation to potentially open up new areas of research and applications in inverse nonlinear frequency mixing. By addressing these three directions, the SH-ODT technique can be further improved and utilized in a wider range of applications, leading to more discoveries in the field of nonlinear ODT.

The studies of this thesis can be generalized to further explore more optical modalities for 3D imaging. Some of these optical modalities in the materials can interact with light in a physically complicated way. Deep learning approaches such as PINNs can be utilized to assist in modeling physical problems in the examination of different optical imaging modalities.

A Appendix: Polarization-sensitive ODT

This part has been reported in the supplementary document of the following paper:

- A. Saba, J. Lim, AB. Ayoub, EE. Antoine, and D. Psaltis (2021). "Polarization-sensitive optical diffraction tomography". *Optica*, 8(3), 402-408.

A.1 Light Propagation in anisotropic inhomogeneous media and vectorial inverse scattering

Here, we discuss the propagation of light and scattering problem for a weak anisotropic scatterer placed in a homogeneous and isotropic background medium. Starting from Maxwell's equations for a monochromatic wave,

$$\nabla \times \vec{E} = j\omega \vec{B} \quad (\text{A.1a})$$

$$\nabla \times \vec{B} = -j\omega/c^2 \overline{\overline{\epsilon}}_r \vec{E} \quad (\text{A.1b})$$

where, $\overline{\overline{\epsilon}}_r$ is the relative permittivity tensor, ω is the temporal frequency, and c is the speed of light in vacuum, we can get the following equation,

$$\nabla \times \nabla \times \vec{E} = -\nabla^2 \vec{E} + \nabla \nabla \cdot \vec{E} = \omega^2/c^2 \overline{\overline{\epsilon}}_r \vec{E} \quad (\text{A.2})$$

We can define the refractive index tensor of the birefringent sample as,

$$\overline{\overline{\epsilon}}_r = \left(n_0 \mathbb{1} + \overline{\overline{\delta n}} \right)^2 \approx n_0^2 \mathbb{1} + 2n_0 \overline{\overline{\delta n}} = n_0^2 \mathbb{1} + \overline{\overline{\delta \epsilon}} \quad (\text{A.3})$$

where, n_0 is the refractive index of the isotropic background medium, and $\overline{\overline{\delta n}}$ and $\overline{\overline{\delta \epsilon}}$ are the refractive index and permittivity tensors of the anisotropic scatterer relative to the background. $\mathbb{1}$ is the identity matrix. Diagonalization of the refractive index tensor we defined in Eq. A.3 yields the phase velocity of the polarization eigenstates. The term of $\nabla \nabla \cdot \vec{E}$ can lead to polarization coupling even in the absence of birefringence, i.e. for a sample with scalar permittivity. This term can be neglected if the scale of the variation of the permittivity (or the envelope of the field) is much larger than the wavelength (the slowly varying envelope approximation), $\lambda \ll \xi(\delta \epsilon)^I$ [107], which is equivalent to the paraxiality [110]. We assume that the only reason for polarization coupling is the birefringence of the sample since the sample varies slowly with respect to the wavelength. The total field vector, \vec{E} , can be represented as the summation of the incident, \vec{E}^i , and scattered, \vec{E}^s , field vectors. By considering the fact that $(\nabla^2 + k_0^2 n_0^2) \vec{E}^i = 0$, we have,

$$(\nabla^2 + k_0^2 n_0^2) \vec{E}^s = -k_0^2 \overline{\overline{\delta \epsilon}} \vec{E} \quad (\text{A.4})$$

k_0 is the light wave-vector in the free-space. The right hand side of this equation is a vector that functions as a scattering source, and we look for the solution of vector \vec{E}^s that satisfies Eq. A.4. The left hand side of this equation is related to the background medium, n_0 which is isotropic and homogenous. This makes each component of these vectors (left and right side) uncoupled from each other. So, the Green's function of this equation can be represented by a diagonal tensor with same components for each polarization,

$$\overline{\overline{G}} = \begin{pmatrix} g(r, r') & 0 & 0 \\ 0 & g(r, r') & 0 \\ 0 & 0 & g(r, r') \end{pmatrix} \quad (\text{A.5})$$

in which, $g(r, r') = e^{jk_0 n_0 (r-r')} / |r-r'|$, same as the scalar case. Now, we assume the first-order Born approximation, and replace the field vector in the right hand side of Eq. A.4 with the input unperturbed beam. Defining the scattering potential tensor as $\overline{\overline{V}} = k_0^2 \overline{\overline{\delta \epsilon}} / 4\pi$, we can represent the scattered field vector as,

$$\vec{E}^s(r) = \int \overline{\overline{G}}(r, r') \times \overline{\overline{V}}(r') \times \vec{E}^{illum}(r') d^3 r' \quad (\text{A.6})$$

There is an important point regarding Eq. A.6. In Eq. (15) of [111], the scattered field under the Born approximation is derived as,

$$\vec{E}^s(|r| \hat{u}) = \int \overline{\overline{G}}(r, r') \times \overline{\overline{V}}(r') \times \left(\vec{E}^{illum}(r') - \hat{u} \cdot \vec{E}^{illum}(r') \right) d^3 r' \quad (\text{A.7})$$

\hat{u} is the unit vector along the scattered field component. Unlike Eq. A.6, Eq. A.7 has the $\hat{u} \cdot \vec{E}^{illum}$ term. It can be followed in [111] that this term is coming from $\nabla \nabla \cdot \vec{E}$ in the

^I $\xi(\delta \epsilon)$ is the correlation length of the inhomogeneity of the sample, which can be defined as $\langle \delta \epsilon(r) | \delta \epsilon(r') \rangle \approx e^{-(r-r')/\xi}$.

vectorial Helmholtz equation which we neglected. In the topic of paraxiality, we can say that the scattered field has the spatial frequency components that are very close to the incident illumination, \vec{k}_i , and as a result, we will have $\hat{u} \cdot \vec{E}^{illum} \approx 0$ which will lead to the same equation as ours. This shows the equivalence of the slowly varying approximation, paraxiality, and the approximation that the light does not depolarize due to the inhomogeneity of the sample. It should be noted that in the scalar case, the relationship between the scattered field and the scattering potential becomes linear, under the Born approximation. However, if we do not neglect the $\nabla \nabla \cdot \vec{E}$ term, due to the presence of the spatial frequency component of the scattered field, \hat{u} , on the right side of Eq. A.7, the relationship remains nonlinear even under the Born approximation. This is the reason why we actually neglect this term, which is valid for slowly-varying samples.

In the general case, the scattering potential tensor in Eq. A.6 as well as the refractive index tensor are 3×3 tensors. However, the polarization state of the illumination beam \vec{E}^{illum} should be perpendicular to its wave-vector, and as a result, can only have two *independent* states. Lets us consider two separate experiments with two different and independent polarization states for E^{illum} . We can put these two experiments in the same framework by representing the incident field in two different columns of a 3×2 matrix. We assume that the measured fields are in XY coordinate system:

$$\begin{pmatrix} E_{x1}^s(r) & E_{x2}^s(r) \\ E_{y1}^s(r) & E_{y2}^s(r) \\ E_{z1}^s(r) & E_{z2}^s(r) \end{pmatrix} = \int \overline{\overline{G}}(r, r') \times \overline{\overline{V}}(r') \times \begin{pmatrix} E_{x1}^{illum}(r') & E_{x2}^{illum}(r') \\ E_{y1}^{illum}(r') & E_{y2}^{illum}(r') \\ E_{z1}^{illum}(r') & E_{z2}^{illum}(r') \end{pmatrix} d^3 r' \quad (\text{A.8})$$

By assuming a plane wave illumination, $\vec{E}^{illum}(r') = \tilde{E}^{illum} e^{j\vec{k}_i \cdot r'}$ (\tilde{E}^{illum} is the illumination field amplitude, and \vec{k}_i is its wave-vector), Eq. A.8 can be written as:

$$\begin{pmatrix} E_{x1}^s(r) & E_{x2}^s(r) \\ E_{y1}^s(r) & E_{y2}^s(r) \\ E_{z1}^s(r) & E_{z2}^s(r) \end{pmatrix} = \left[\int \overline{\overline{G}}(r, r') \times \overline{\overline{V}}(r') e^{j\vec{k}_i \cdot r'} d^3 r' \right] \times \begin{pmatrix} \tilde{E}_{x1}^{illum} & \tilde{E}_{x2}^{illum} \\ \tilde{E}_{y1}^{illum} & \tilde{E}_{y2}^{illum} \\ \tilde{E}_{z1}^{illum} & \tilde{E}_{z2}^{illum} \end{pmatrix} \quad (\text{A.9})$$

It can be seen from Eq. A.9 that all the 9 components of the 3×3 scattering potential tensor cannot be retrieved using only two independent input polarization states. We can approximate this equation with a 2×2 representation of the fields and the scattering potential tensors,

$$\begin{pmatrix} E_{x1}^s(r) & E_{x2}^s(r) \\ E_{y1}^s(r) & E_{y2}^s(r) \end{pmatrix} \approx \left[\int \overline{\overline{G}}(r, r') \times \overline{\overline{V}}_{2 \times 2}(r') e^{j\vec{k}_i \cdot r'} d^3 r' \right] \times \begin{pmatrix} \tilde{E}_{x1}^{illum} & \tilde{E}_{x2}^{illum} \\ \tilde{E}_{y1}^{illum} & \tilde{E}_{y2}^{illum} \end{pmatrix} \quad (\text{A.10})$$

$\overline{\overline{V}}_{2 \times 2}$ is the 2×2 block matrix of the full scattering potential tensor whose definition can be

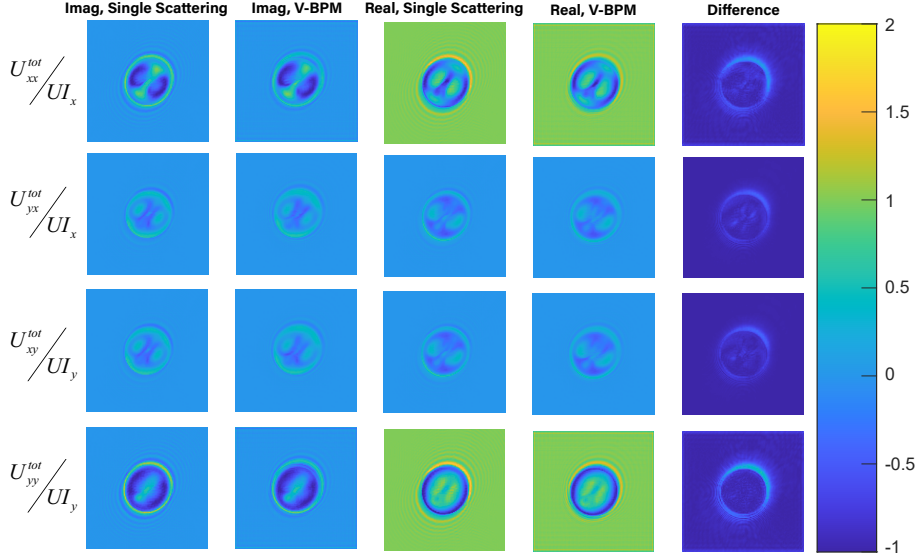


Figure A.1: Comparison of the scattered vectorial fields for the birefringent digital phantom based on the vectorial single scattering and V-BPM. Four rows represent the components of the Jones matrix. First and second columns show the imaginary part of Jones components based on the single scattering and V-BPM model, respectively. Third and fourth columns show the real parts of them, and the last column shows the absolute value of the difference between the single scattering model and V-BPM.

clarified as,

$$\overline{\overline{V}} = \begin{pmatrix} \overline{\overline{V}}_{2 \times 2} & V_{xz} \\ V_{zx} & V_{zy} \\ V_{zx} & V_{zy} & V_{zz} \end{pmatrix} \quad (\text{A.11})$$

From now, the 2×2 scattering potential tensor is referred as $\overline{\overline{V}}$ and we drop the 2×2 index. More details about this approximation and accuracy of that is further discussed in section 3.2.2 of this document.

Writing Eq. A.10 in the Fourier domain and using the Fourier diffraction theorem [13], we arrive at the vectorial version of the Wolf transform as follows:

$$\overline{\overline{V}}(k_x - k_x^{in}, k_y - k_y^{in}, k_z - k_z^{in}) = \frac{k_z}{2\pi j} \mathcal{F}_{2D} \left\{ \begin{pmatrix} E_{x1}^s & E_{x2}^s \\ E_{y1}^s & E_{y2}^s \end{pmatrix} \begin{pmatrix} \tilde{E}_{x1}^{illum} & \tilde{E}_{x2}^{illum} \\ \tilde{E}_{y1}^{illum} & \tilde{E}_{y2}^{illum} \end{pmatrix}^{-1} \right\} (k_x, k_y) \quad (\text{A.12})$$

where, $k_z = \sqrt{k^2 - k_x^2 - k_y^2}$, and \mathcal{F}_{2D} is the 2D Fourier transform. This equation maps the 2D Fourier components of the Jones matrix to the 3D Fourier components of the scattering potential tensor. The Fourier transforms should be applied independently for each term of the matrices.

A.2 Vectorial Beam Propagation method

We start from the vectorial Helmholtz equation:

$$\left(\nabla^2 + k_0^2 \overline{\overline{\epsilon_r}}\right) \vec{E} = 0 \quad (\text{A.13})$$

We can define the complex vector envelope of $\vec{\psi}(r)$ as,

$$\vec{E}(r) = \vec{\psi}(r) e^{jk_0 n_0 z} \quad (\text{A.14})$$

By assuming the slowly varying envelope approximation and neglecting $\partial^2 / \partial z^2 \vec{\psi}(r)$, we can rewrite Eq. A.13 as follows,

$$\frac{\partial}{\partial z} \vec{\psi}(r) = \frac{j}{2k} \left(\mathbb{1} \nabla_t^2 + k_0^2 \overline{\overline{\epsilon_r}} \right) \vec{\psi}(r) = \mathcal{M}_1 \{ \vec{\psi}(r) \} + \mathcal{M}_2 \{ \vec{\psi}(r) \} \quad (\text{A.15})$$

where the diffraction operator, \mathcal{M}_1 , is a diagonal operator, and \mathcal{M}_2 is the phase and amplitude modulation operator. Like the scalar BPM, the solution of this equation can be approximated as,

$$\vec{\psi}(x, y, z + dz) \approx e^{\mathcal{M}_2 dz} e^{\mathcal{M}_1 dz} \vec{\psi}(x, y, z) \quad (\text{A.16})$$

This approximation comes from the fact that operators \mathcal{M}_1 and \mathcal{M}_2 do not necessarily commute with each other and as a result we have $e^{(\mathcal{M}_2 + \mathcal{M}_1) dz} \neq e^{\mathcal{M}_1 dz} e^{\mathcal{M}_2 dz}$. However, based on the Baker-Campbell-Hausdorff formula [112], we can make this approximation for a small dz . Then, the diffraction operator, \mathcal{M}_1 , is a diagonal operator which we can be implemented in the Fourier domain:

$$e^{\mathcal{M}_1 dz} \vec{\psi}(x, y, z) = \mathcal{F}^{-1} \left\{ \mathbb{1} e^{-j \frac{k_x^2 + k_y^2}{2k} dz} \times \mathcal{F} \{ \vec{\psi}(x, y, z) \} \right\} \quad (\text{A.17})$$

A more accurate way of implementing the diffraction operator with a nonparaxial version is presented in [113] where we replace the multiplier in Eq. A.17 with $\exp(-j(k_x^2 + k_y^2)/(k + k_z) dz)$. The role of operator \mathcal{M}_2 is the phase modulation of the complex vector of $\vec{\psi}(x, y, z)$, during the propagation through the step, dz , with the refractive index tensor. This is an operator with off-diagonal components which leads to the polarization coupling as light propagates through the birefringence sample. Using Eq. A.3, we can write it as,

$$e^{\mathcal{M}_2 dz} \vec{\psi}(x, y, z) = \text{expm}(j k_0 \overline{\overline{\delta n}}(x, y, z) dz) \times \vec{\psi}(x, y, z) \quad (\text{A.18})$$

operator expm is the matrix exponential. For a matrix, A , the matrix exponential can be defined as,

$$\text{expm}(A) = \sum_{k=0}^{\infty} \frac{A^k}{k!} \quad (\text{A.19})$$

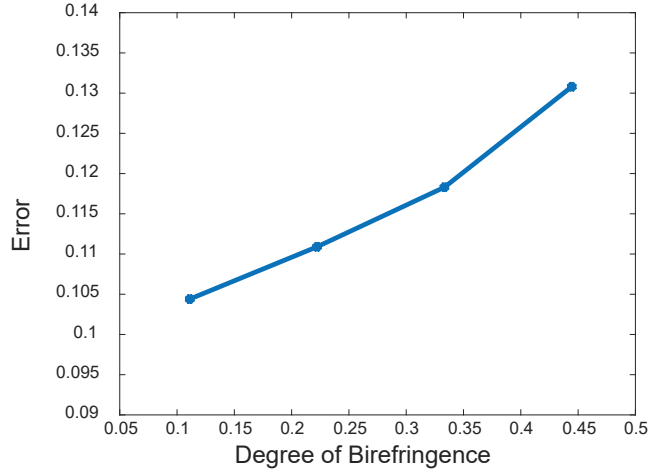


Figure A.2: Error of the single scattering forward model with respect to V-BPM for different digital phantoms as the degree of birefringence increases.

If we diagonalize the matrix $A = UDU^{-1}$, where D is a diagonal matrix with the eigenvalues of A , the exponential of that can be written as $\expm(A) = Ue^DU^{-1}$. This way, the eigenvalues of the phase modulation matrix in Eq. A.18 will be $e^{jk_0\mu_n^1}$ and $e^{jk_0\mu_n^2}$ where $\mu_n^{1,2}$ are the eigenvalues of the refractive index tensor [114].

It should be noted that both amplitudes and phases of each element of the field will change while the overall amplitude of the vector remains unchanged. In [115], it has been shown that we can get more accurate results if we replace dz with $dz/\cos\theta$, owing to the fact that the length of propagation will scale with the illumination angle. Finally, we can write the following equation to summarize V-BPM:

$$\vec{\psi}(x, y, z + dz) = \expm\left(jk_0\overline{\overline{\delta n}}dz/\cos\theta\right) \times \mathcal{F}_{2D}^{-1}\left\{e^{-j\frac{k_x^2+k_y^2}{k+k_z}}dz \times \mathcal{F}_{2D}\{\vec{\psi}(x, y, z)\}\right\} \quad (\text{A.20})$$

As the reconstruction method is based on the single-scattering model (Rytov approximation), the accuracy of the reconstruction is directly related to the validity of the single-scattering approximation. In order to test this validity, we generated synthetic scattered field measurements using V-BPM and compared them with the ones generated using the single scattering model (Eq. A.8). For a digital birefringent phantom (same as the one which is shown in section A.4), we compare the complex fields achieved after the scattering from the phantom. We show this comparison in Fig. A.1. Imaginary and real parts of the complex Jones matrix components are presented. Each row shows one of the 4 components of the Jones matrix, columns show the imaginary and real parts of it, acquired using the single scattering forward model and V-BPM. The last column shows the absolute value of their differences. You can see the pronounced differences around the edges where we have strong scattering. In Fig. A.2, we tried 4 different phantoms by increasing the degree of their birefringence (off diagonal refractive index), and we calculated the error between the single scattering model and V-BPM. We can see that

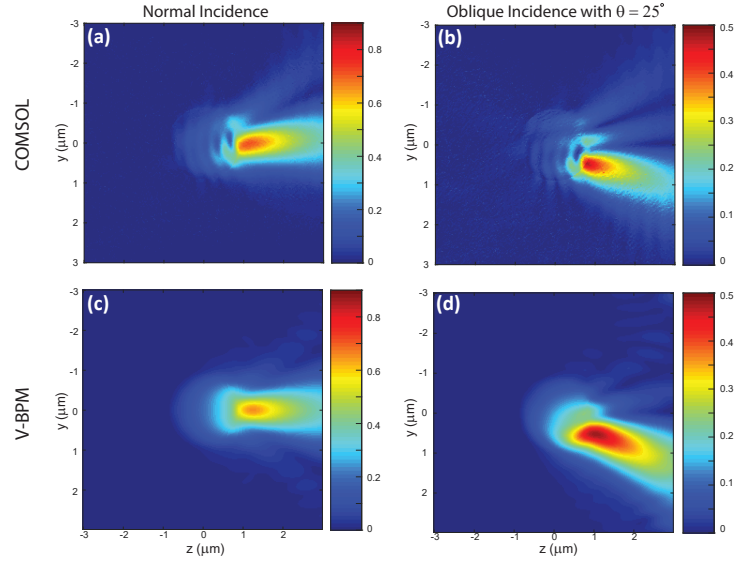


Figure A.3: Verification of V-BPM using FEM: calculated $|E_y|/|E_x^{in}|$ by FEM (COMSOL) for (a) normal incidence and (b) oblique incidence with $\theta = 25^\circ$ and using V-BPM for (c) normal and (d) oblique incidence with $\theta = 25^\circ$.

the stronger the birefringence, we have the larger value of error. This is independent of the fact that how much the sample is scattering, while in these 4 phantoms, the strength of the scatterer is relaxed by keeping the diagonal components of the refractive index fixed.

In order to verify the accuracy of our V-BPM, we did a full-wave 3D simulation with the finite element method (FEM). This simulation has been done using a commercial FEM solver, COMSOL Multiphysics 5.4. In this simulation, we illuminate a birefringent sphere with a refractive index tensor of

$$\bar{\bar{n}} = n_0 \mathbb{1} + \begin{pmatrix} 0.09 & 0.02 & 0.02 \\ 0.02 & 0.09 & 0.02 \\ 0.02 & 0.02 & 0.09 \end{pmatrix} \quad (\text{A.21})$$

which is placed in the background homogeneous medium with refractive index n_0 . We study two cases of a normal illumination with input X-polarized light and an oblique illumination with X-polarization state with $\theta = 25^\circ$ in the YZ-plane. Results are presented in Fig. A.3. We show the YZ field profiles and compare them with V-BPM. We can see a good agreement between these two methods even in the case of oblique illumination. It should be noted that due to computational reasons we use a Tetrahedral meshing in the FEM simulation and a rectangular meshing in the V-BPM.

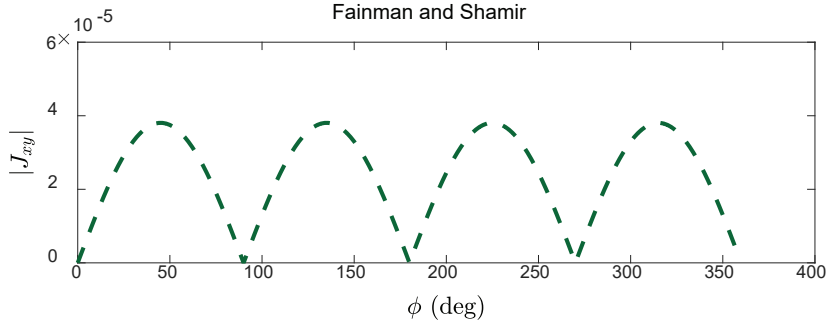


Figure A.4: The off-diagonal component of the Jones matrix of an ideal polarizer as it is illuminated with a tilted beam as we scan φ .

A.3 Effect of a tilted polarizer

According to the experimental setup in Fig. 3.3(a) of chapter 3, we put a polarizer after the imaging system to measure the desired output polarizer. However, this polarizer is illuminated obliquely while scanning the illumination angle. Therefore, the Jones matrix of a tilted polarizer changes depending on its angle and is different from when it is illuminated normally. To analyze the effect of tilted polarization, we use the Fainman-Shamir model [116]. According to this model which is for an ideal polarizer, the Jones matrix of a polarizer can be achieved as,

$$\bar{J}_P = \frac{(\hat{P}_A - \hat{P}_A \cdot \hat{k}_{in})(\hat{P}_A - \hat{P}_A \cdot \hat{k}_{in})^\dagger}{1 - (\hat{P}_A \cdot \hat{k}_{in})^2} \quad (\text{A.22})$$

in which, \hat{P}_A is the unitary vector along which the polarizer/analyzer are aligned (in the plane of the polarizer), and \hat{k}_{in} is the unitary vector of the incident wave-vector. In our setup, we use a 60X imaging system which means a 60X angular demagnification. This way, the polarizer is illuminated with a 0.5° angle ($\sim 30^\circ/60$). The off-diagonal term, J_{xy} , of the Jones matrix, J_P , is shown in Fig. A.4. According to this figure, we can see that this term is very small, compared to J_{xx} and we can completely neglect this effect. Especially, a calibration step, which measures both co and cross-polarizations without the sample will handle these inaccuracies. Moreover, the most important issue to be considered for the tilted illumination is the rotational matrix described as Eq.3.5 of chapter 3.

A.4 Numerical Results

Here, we present more figures about the numerical results partly presented in chapter 3. For the digital phantom which we discussed in chapter 3, we show the Jones matrix calculated for 3 different illumination angles, $\varphi = 0^\circ$, $\varphi = 120^\circ$, $\varphi = 240^\circ$ in Fig. A.5. The complex values are coded using the brightness and color (amplitude and phase, respectively) in the figure. The circular diffraction pattern along the illumination direction is clear in the amplitude of

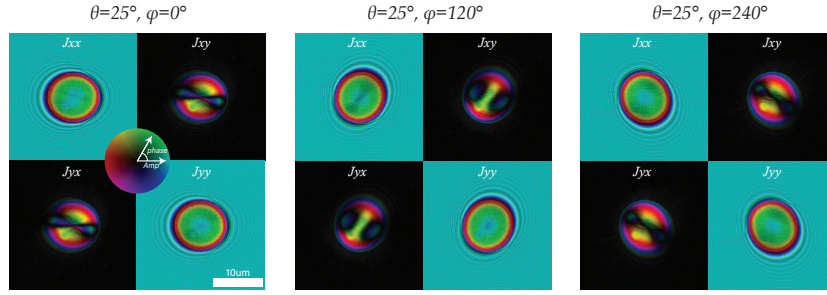


Figure A.5: The Jones matrix of the digital phantom calculated with the V-BPM for 3 different projections. Same data for 180 projections are used to reconstruct the 3D phantom.

the total field. In the absence of the sample, the off-diagonal terms of the Jones matrix are zero, which means that there is no cross-polarization coupling. In Fig. A.6, we show the full reconstruction of the refractive index tensor, which we showed only two of them, n_{xx} , and n_{yx} in Fig. 3.6 of chapter 3. For each component of the refractive index tensor, the first row shows the ground truth and the second row shows the reconstruction using the polarization-sensitive ODT with Rytov approximation. Here, we show the YX, XZ, and YZ profiles of the 3D reconstruction.

An important issue regarding the refractive index tensor is the fact that the off-diagonal components of this tensor do not present any inherent information, by their own value, regarding the birefringence, or orientation of the slow-axis (or fast axis) of the sample. In fact, the latest parameters have a physical meaning about the anisotropy of the sample and the tensorial representation of the refractive index is the consequence of an unknown rotation of the sample with respect to its axis and the experiment coordinate system. It has been discussed in chapter 3 that how the eigen-value characterization of the refractive index tensor can help to find some 3D parameters correlated with physical and inherent meanings. In fact, eigenvalues and eigen-vectors of a tensor are invariant under any unitary transformation such as coordinate rotation. In each voxel of the sample, the difference between the eigen-values of the 3D refractive index tensor can represent the birefringence of the sample and the orientation of the eigen-vector corresponding to the bigger (smaller) eigen-value can represent the direction of the slow-(fast-)axis of the sample. In Fig. A.7 you can see the 3D birefringence and also the orientation of the slow-axis that are extracted from the eigen-value characterization of the refractive index tensor for the numerical phantom.

A.5 Denoising and Iterative reconstruction

Due to the coherent noise which exists in the holography technique, we used a denoising technique based on a 3D total-variation (TV) to a bit smooth-out our final reconstruction. In the denoising problem, we minimize the following cost function, to calculate the image \hat{x}

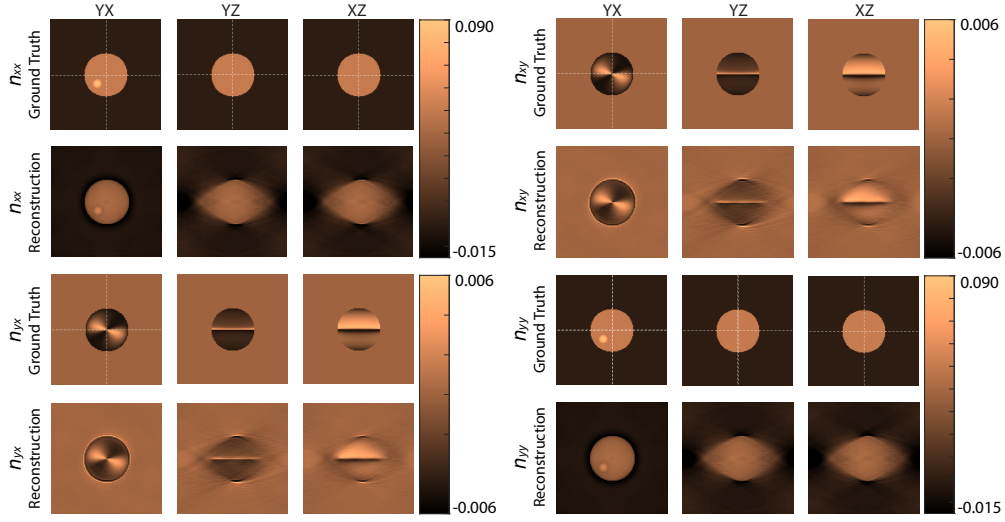


Figure A.6: Polarization-sensitive reconstruction of the digital phantom using the Rytov approximation. For each component of the tensor, we show the ground-truth and the reconstruction in YX, YZ, and XZ planes. Dashed lines show the lines that we show the profile of the index along them.

from the noisy image x :

$$\min_{\hat{x}} \{ \|\hat{x} - x\|^2 + \lambda R_{TV}(\hat{x}) \} \quad (\text{A.23})$$

in which, $R_{TV}(\hat{x})$ is the TV regularization and λ is the regularization parameter which determines how strongly this TV denoising regularization applies. However, a very important issue is that this denoising should not be confused with iterative techniques that are used to compensate for the missing-cone problem. In the missing-information problem, on the other hand, we have an under-determined problem that we use a total variation or a set of sparsity constraints to overcome. This has to be done using the minimization of such a cost function:

$$\min_{\hat{x}} \{ \|A\{\hat{x}\} - b\|^2 + \lambda R_{TV}(\hat{x}) \} \quad (\text{A.24})$$

for which A is some linear map which is usually the Fourier transform in the case of missing-cone problem for ODT [26]. A clearer discussion on this topic is presented in a work by A. Beck and M. Teboulle [117] where they clarify the difference between the two problems of denoising and deblurring (which solves missing frequencies similar to the missing cone problem in ODT).

As a result, in our work, we just used TV regularization to denoise the final reconstructions and we should not expect that the missing cone problem gets fixed. However, we also did an iterative reconstruction using TV regularization to solve the missing cone problem that we wish to extend in another work later. This method is based on the tensorial version of [26]. We use Eq. A.24 where,

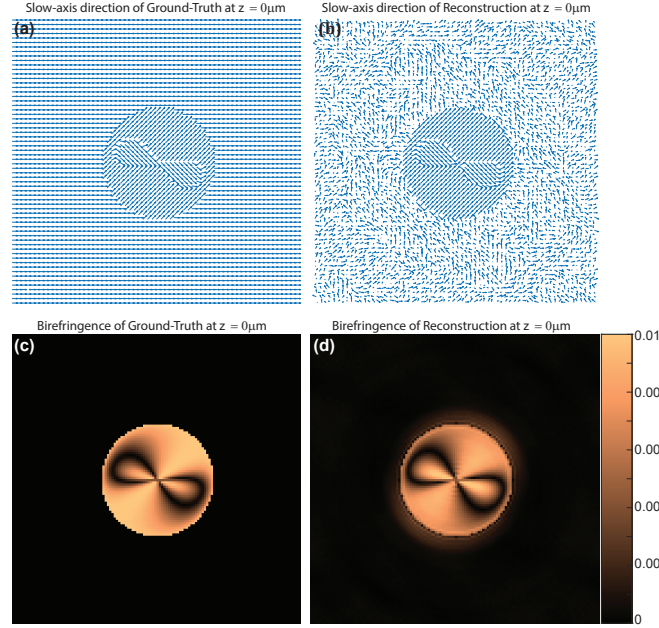


Figure A.7: Eigen-value characterization of the refractive index tensor of the digital phantom: (a) Profile of the 3D Slow-axis direction at $z = 0\mu\text{m}$ for the ground-truth, (b) Profile of the 3D Slow-axis direction at $z = 0\mu\text{m}$ for the 3D reconstruction, (c) Profile of the 3D Birefringence ($\mu_n^1 - \mu_n^2$) of the ground-truth, (d) Profile of the 3D Birefringence ($\mu_n^1 - \mu_n^2$) of the 3D reconstruction.

$$A\{\overline{\mathbf{V}}\} = \overline{\mathbf{V}} \left(k_x - k_x^{in}, k_y - k_y^{in}, k_z - k_z^{in} \right) \quad (\text{A.25a})$$

$$b = \frac{k_z^{in}}{2\pi j} \mathcal{F}_{2D} \left\{ \begin{pmatrix} E_{x1}^s & E_{x2}^s \\ E_{y1}^s & E_{y2}^s \end{pmatrix} \begin{pmatrix} E_{x1}^i & E_{x2}^i \\ E_{y1}^i & E_{y2}^i \end{pmatrix}^{-1} \right\} \quad (\text{A.25b})$$

with the parameters similar to what is defined in chapter 3. The iterative reconstruction is presented in Fig. A.8. In the first row, we show the ground-truth, in the second row we show the direct Rytov-based reconstructions as presented in chapter 3, and in the third row, we show the iterative reconstruction using TV regularization. As is clear from this figure, the third-row reconstructions do not include any elongation along z-axis in contrast to the second row. This shows that similar to the scalar ODT, iterative techniques with a linear forward model, or even a nonlinear forward model can be used for polarization-sensitive ODT.

A.6 Muscle tissue Experiment

To show the importance of the PS-ODT for biological samples, we did the experiment for muscle tissue. Muscle tissue is birefringent due to its fibrous structures and A-bands (thick filaments) inside the sarcomere of the muscle fiber. The fresh frozen muscle section is em-

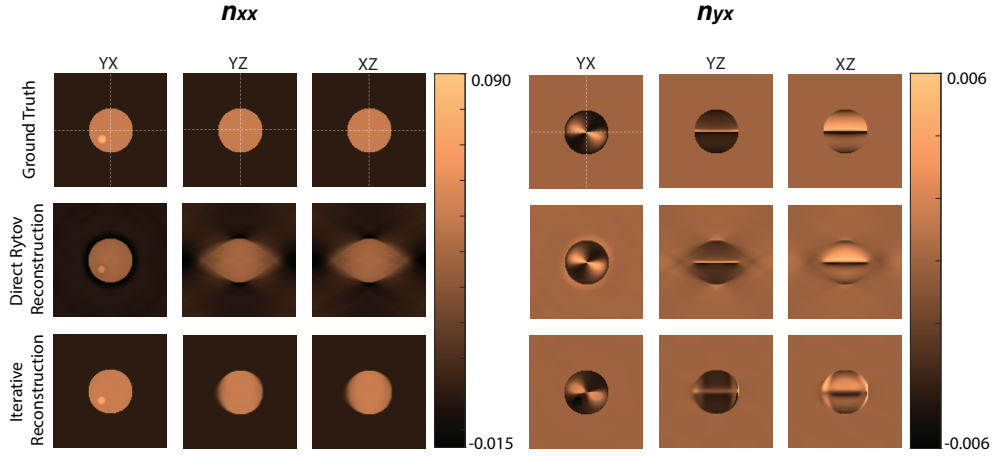


Figure A.8: Iterative reconstruction of the digital phantom: 1st row: ground-truth, 2nd row: direct iterative reconstructions, 3rd row: iterative reconstruction using TV regularization.

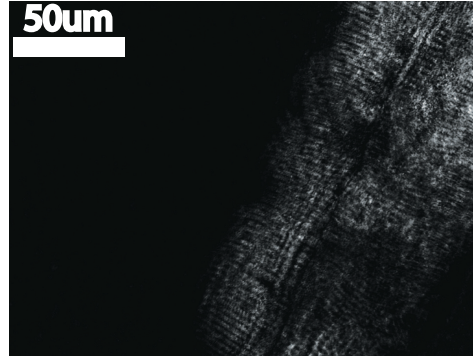


Figure A.9: The cross-polarized light amplitude $|U_{xy}^s|^2$ which is measured for the muscle tissue.

bedded in cryo medium and cut with $20\mu m$ thickness. This thickness is enough to get a nice and strong cross-polarized light and at the same time keep the single-scattering condition satisfied. In Fig. A.9, we present the cross-polarized light (U_{xy}^s) intensity. In Fig. A.10, the extracted holographical phase of one of the projections is shown for the muscle tissue. In Fig. A.10(a), the phase of the cross-polarized light is presented (U_{xy}^s) while in Fig. A.10(b) we show the phase of (U_{xa}^s). In Fig. A.10(a), due to the zero background intensity, the background phase is random which makes the calibration (because of the ambiguity of the phase of the reference beam) and phase unwrapping difficult. On the other hand, using 45° polarization idea, the background phase of the complex field (U_{xa}^s) is smooth and nearly uniform since the input and output polarizations have only 45° of miss-alignment and as a result we have a background intensity. This helps to unwrap and calibrate the phase of the complex fields easily and then convert the reconstructions to the XY coordinate system.

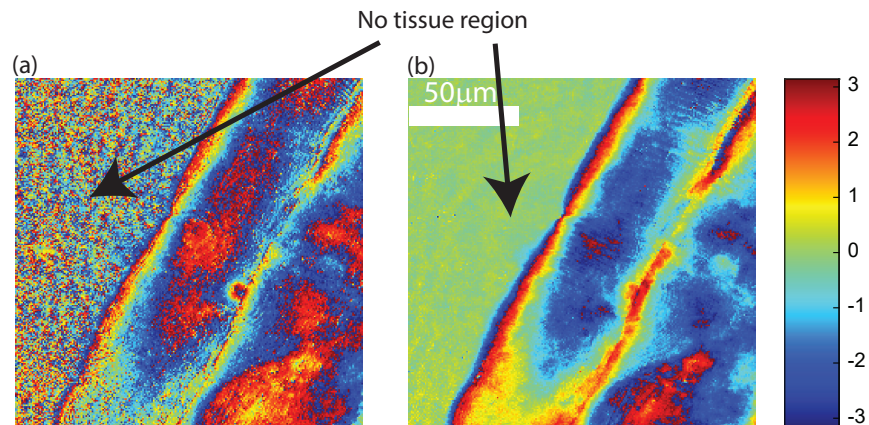


Figure A.10: The phase of the scattered field. (a) for U_{xy}^s and (b) for U_{xa}^s . The background phase is random due to the zero intensity in the cross-polarized light. By contrast, in (b) the background phase can be easily calibrated and unwrapped.

B Appendix: Second-harmonic ODT

B.1 Wave propagation in nonlinear inhomogeneous media

The nonlinear polarizability for SHG process is as,

$$\begin{pmatrix} P_x(2\omega) \\ P_y(2\omega) \\ P_z(2\omega) \end{pmatrix} = \epsilon_0 \bar{\chi}^{(2)} \begin{pmatrix} E_x(\omega)^2 \\ E_y(\omega)^2 \\ E_z(\omega)^2 \\ 2E_y(\omega)E_z(\omega) \\ 2E_x(\omega)E_z(\omega) \\ 2E_x(\omega)E_y(\omega) \end{pmatrix} \quad (\text{B.1})$$

where $E_x(\omega)$, $E_y(\omega)$, and $E_z(\omega)$ are the field components for the fundamental light. We write the 6×1 squared field vector as $(\vec{E}_F \star \vec{E}_F)$ notation. Considering the undepleted pump approximation, and neglecting the depolarization of light due to the high-gradient variations in the refractive index distribution, we can write two Helmholtz equations at fundamental and SH wavelengths,

$$\begin{aligned} \nabla^2 \vec{E}_F(r, \omega) + k_0^2 n^2(r, \omega) \vec{E}_F(r, \omega) &= 0 \\ \nabla^2 \vec{E}_{SH}(r, 2\omega) + 4k_0^2 n^2(r, 2\omega) \vec{E}_{SH}(r, 2\omega) &= -4k_0^2 \bar{\chi}^{(2)}(r) \cdot (\vec{E}_F(r, \omega) \star \vec{E}_F(r, \omega)) \end{aligned} \quad (\text{B.2})$$

where $\vec{E}_F(r, \omega)$ and $\vec{E}_{SH}(r, 2\omega)$ are the field vectors at the fundamental and SH wavelengths, $k_0 = 2\pi/\lambda_F$ is the fundamental wave number, and $n(r, \omega)$ and $n(r, \omega)$ are the refractive index distributions at the fundamental and SH wavelengths that will be equal in the case of no dispersion. The first equation of Eq. B.2 provides the linear scattering of the fundamental light. We can rewrite the right side of the second equation using the first-order Born approximation by replacing $\vec{E}_F(r)$ with the incident field $\vec{E}_i(r)$. The incident field is a plane wave that is propagating unchanged through the background medium, and as a result, its amplitude and polarization state will be fixed. If we consider this incident plane wave as the electric

field vector of $\vec{E}_i(r) = E_0 e^{j\vec{k}_{in}\cdot r} [p_x, p_y, p_z]^T$, we can write the Helmholtz equation at the SH wavelength as,

$$\nabla^2 \vec{E}_{SH}(r, 2\omega) + 4k_0^2 n^2(r, 2\omega) \vec{E}_{SH}(r, 2\omega) = 4\pi E_0^2 e^{2j\vec{k}_{in}\cdot r} \vec{V}^{(SH)}(r) \cdot \vec{Q}_{illum} \quad (\text{B.3})$$

where $\vec{Q}_{illum} = [p_x, p_y, p_z]^T \star [p_x, p_y, p_z]^T = [p_x^2, p_y^2, p_z^2, 2p_y p_z, 2p_x p_z, 2p_x p_y]^T$ is the 6×1 squared polarization vector, and $\vec{V}^{(SH)} = k_0^2 / \pi \bar{\chi}^{(2)}(r)$ is the SH scattering potential. Eq. B.3 is the vectorial Helmholtz equation governing the generation of the SH field in the second-order nonlinear media. This equation is achieved with 3 approximations so far: (i) only ω and 2ω frequencies are involved in the interaction, (ii) Neglecting the depletion of the fundamental beam, and (iii) the first-order Born approximation in the scattering of the fundamental beam. The inhomogeneity of the sample in the refractive index distribution, $n^2(r, 2\omega)$ controls the scattering of the generated SH field in the sample. A fourth approximation to further simplify Eq. B.3 is to neglect the rescattering of the SHG due to the inhomogeneity of the sample. This approximation implies to replace $n(r, 2\omega)$ with $n_0(2\omega)$ in the left side of Eq. B.3. Using this approximation, we can write the integral solution of Eq. B.3 using Green's function of this equation,

$$\vec{E}^{SH}(r) = \int G^{SH}(\mathbf{r} - \mathbf{r}') \cdot E_0^2 e^{2j\vec{k}_{in}\cdot \mathbf{r}'} \cdot \vec{V}^{SH}(\mathbf{r}') \vec{Q}_{illum} d\mathbf{r}' \quad (\text{B.4})$$

in which $G^{SH}(\mathbf{r} - \mathbf{r}') = e^{2jk_0 n_0(2\omega)|r-r'|} / |\mathbf{r} - \mathbf{r}'|$ is the Green's function at SH wavelength. Eq. B.4 is the simplest way to calculate the SHG from an anisotropic sample with inhomogeneous second-order susceptibility illuminated with a plane wave fundamental beam.

B.2 Fourier diffraction theorem for SHG

Next, we try to invert Eq. B.4 in order to present the Fourier diffraction theorem for SHG and a reconstruction method for the scattering potential using multiple-angle SH-generated fields. We use the Fourier diffraction theorem which was presented in section 2.3 on the wave equation for SHG. By taking the Fourier transform of Eq. B.4 and applying the Fourier diffraction theorem which was presented in Eq. 2.20, we have,

$$\vec{V}^{SH}(K_x - 2k_x^{in}, K_y - 2k_y^{in}, K_z - 2k_z^{in}) \vec{Q}_{illum}(k_x^{in}, k_y^{in}, k_z^{in}) = \frac{K_z e^{-jK_z z_0}}{2\pi j E_0^2} \mathcal{F}_{2D} \left\{ \vec{E}^{SH} \right\} (K_x, K_y) \quad (\text{B.5})$$

where K_x , K_y , and K_z are the spatial frequencies. It should be noted that \vec{V}^{SH} is a 3×6 tensor and \vec{Q}_{illum} is a 6×1 vector. As a result, their matrix product will be a 3×1 vector which is coherent with the size of the SH field vector.

In the scalar field approximation, we completely neglect the tensorial form of Eq. B.5 and reconstruct the scalar SH scattering potential, V^{SH} using the scalar SH-generated field. As a

result, we have,

$$V^{SH}(K_x - 2k_x^{in}, K_y - 2k_y^{in}, K_z - 2k_z^{in}) = \frac{K_z e^{-jK_z z_0}}{2\pi j E_0^2} \mathcal{F}_{2D} \{E^{SH}\} (K_x, K_y) \quad (B.6)$$

However, the inversion is more complicated for the tensorial second-order susceptibility. The SH scattering potential is a 3×6 matrix. As a result, we need to measure 3 components of the complex SH field vector for 6 independent states of \vec{Q}_{illum} to be able to find all of the 18 elements of the SH scattering potential tensor. Nevertheless, measurement of E_z^{SH} is impossible as the polarization vector is perpendicular to the cameras. Additionally, there can be only 3 independent states for the \vec{Q}_{illum} of the plane wave. We consider these 3 independent states as generated by the input field polarized along x -axis, y -axis, and $+45^\circ$ in the xy plane. Considering the approximation that the incident illumination angle with respect to the optical axis, z , is small, we can use the same approximation in Appendix ???. As a result, we completely remove the z -term in Eq. B.5 by considering p_z as zero in this equation and removing the last row of this equation which is responsible for E_z^{SH} . Regarding this approximation, we can write,

$$\bar{V}_{2 \times 6}^{SH}(K_x - 2k_x^{in}, K_y - 2k_y^{in}, K_z - 2k_z^{in}) \begin{pmatrix} p_x^2(\vec{k}^{in}) \\ p_y^2(\vec{k}^{in}) \\ 0 \\ 0 \\ 0 \\ 2p_x(\vec{k}^{in})p_y(\vec{k}^{in}) \end{pmatrix} = \frac{K_z e^{-jK_z z_0}}{2\pi j E_0^2} \mathcal{F}_{2D} \left\{ \begin{pmatrix} E_x^{SH} \\ E_y^{SH} \end{pmatrix} \right\} (K_x, K_y) \quad (B.7)$$

where $\bar{V}_{2 \times 6}^{SH}$ contains only the first two rows of the SH scattering potential tensor. We can see that there are three zeros in the \vec{Q}_{illum} which makes the third, fourth, and fifth columns of the SH scattering potential tensor impossible to be retrieved. Thus, we remove these columns and rewrite Eq. B.7 with a 2×3 scattering potential,

$$\bar{V}_{2 \times 3}^{SH}(K_x - 2k_x^{in}, K_y - 2k_y^{in}, K_z - 2k_z^{in}) \cdot \vec{s} = \frac{K_z e^{-jK_z z_0}}{2\pi j E_0^2} \mathcal{F}_{2D} \{ \vec{E}^{SH} \} (K_x, K_y) \quad (B.8)$$

in which $\vec{s} = [p_x^2, p_y^2, 2p_x p_y]^T$. As mentioned earlier, we can invert Eq. B.8 with 3 states for the vector \vec{s} . Considering the 3 states of \vec{s} for x -polarized, y -polarized, and 45° -polarized input field as \vec{s}_1 , \vec{s}_2 , and \vec{s}_3 . Therefore, we can invert Eq. B.8 as follows,

$$\bar{V}_{2 \times 3}^{SH}(K_x - 2k_x^{in}, K_y - 2k_y^{in}, K_z - 2k_z^{in}) = \frac{K_z e^{-jK_z z_0}}{2\pi j E_0^2} \mathcal{F}_{2D} \left\{ \begin{bmatrix} E_{x1}^{SH} & E_{x2}^{SH} & E_{x3}^{SH} \\ E_{y1}^{SH} & E_{y2}^{SH} & E_{y3}^{SH} \end{bmatrix} [\vec{s}_1, \vec{s}_2, \vec{s}_3]^{-1} \right\} (K_x, K_y) \quad (B.9)$$

in which E_{ij}^{SH} is the complex 2D SH field at the imaging plane polarized along $i \in \{x, y\}$ for the input polarization state of $j \in \{1, 2, 3\}$.

B.3 Fourier diffraction theorem with corrected-field Born approximation

We can improve the calculation of the SH field by modifying the first-order Born approximation in Eq. B.2. For the sake of simplicity, we write this section in the scalar field regime but it can be easily written in the tensorial form. We can rewrite Eq. B.2 as follows,

$$\nabla^2 E^{SH}(r) + 4k_0^2 n^2(r) E^{SH}(r) = -4\pi V^{SH}(r) \left(E^F(r) / E^i(r) \right)^2 \left(E^i(r) \right)^2 \quad (\text{B.10})$$

if we define $\psi(r) = (E_F(r) / E_i(r))^{-2}$ and use the relationship of $\nabla^2(fg) = f\nabla^2g + 2\nabla f \cdot \nabla g + g\nabla^2f$, we can write,

$$\nabla^2(\psi(r)E^{SH}(r)) - 2\nabla\psi(r) \cdot \nabla E^{SH} + (4k_0^2 n^2(r)\psi(r) - \nabla^2\psi(r))E^{SH}(r) = -4\pi V^{SH}(r) \left(E^i(r) \right)^2 \quad (\text{B.11})$$

Using the slowly varying approximation we can assume that $\psi(r)$ and E^{SH} are varying slowly. As a result, we can neglect the second term of the left side and replace $4k_0^2 n^2(r)\psi(r) - \nabla^2\psi(r)$ with $4k_0^2 n_0^2(r)\psi(r)$ in the third term of the left side in Eq. B.11. This way, we will have,

$$\{\nabla^2 + 4k_0^2 n_0^2(r)\} (E_{SH}(r)\psi(r)) = -4\pi V^{SH}(r) (E_i(r))^2 \quad (\text{B.12})$$

Comparing Eq. B.12 with Eq. B.2, we can simply apply the Fourier diffraction theorem and write a similar equation to Eq. B.6 as,

$$V^{SH}(K_x - 2k_x^{in}, K_y - 2k_y^{in}, K_z - 2k_z^{in}) = \frac{K_z e^{-jK_z z_0}}{2\pi j E_0^2} \mathcal{F}_{2D} \left\{ E^{SH}(r) \left(\frac{E_i(r)}{E_F(r)} \right)^2 \right\} (K_x, K_y) \quad (\text{B.13})$$

Eq. B.13 corrects the SH field with the fundamental field scattering and can slightly improve the first-order Born approximation considering the scattering of the fundamental beam due to the inhomogeneity of the refractive index distribution.

B.4 Muscle tissue experiment

We placed a muscle tissue sample containing several fibers in the experimental setup shown in chapter 4. In order to have an SH bright-field imaging mode, we block the SH reference beam. Additionally, a bright field image of the sample is measured using a green LED source. We can see many interesting details of the sample in the SH image which cannot be revealed in the bright-field image, such as the periodic arrangement of the sarcomeres units.

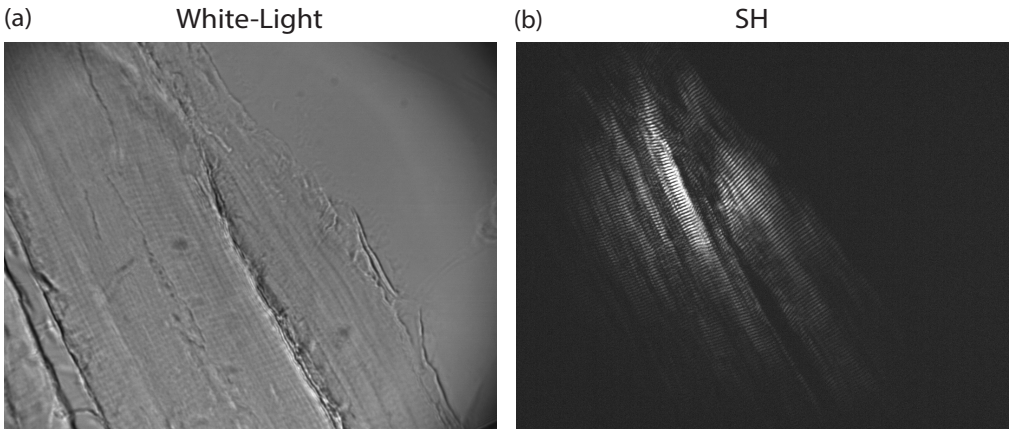


Figure B.1: (a) Bright-field microscopy of the muscle fiber tissue using green light. (b) Wide-field SH image of the muscle fiber in the same region.

C Appendix: Iterative ODT using physics-informed deep learning

This part has been taken from the appendices of the following paper:

- A. Saba, C. Gigli, A. B. Ayoub, and D. Psaltis (2022). Physics-informed neural networks for diffraction tomography. *Advanced Photonics*, 4(6), 066001.

C.1 Calculation of Physics-informed Loss

During the training of MaxwellNet, we calculate at each epoch the loss function in Eq. 5.1 for the network output. In order to evaluate the Helmholtz equation residual, we should numerically compute the term $\frac{\partial^2 U^s}{\partial x^2} + \frac{\partial^2 U^s}{\partial y^2} + \frac{\partial^2 U^s}{\partial z^2}$. In the previous PINN papers for solving PDEs [95]–[97], [99]–[102], the inputs of the network are the spatial coordinates x , y , z , and the derivatives with respect to these variables can be calculated using the chain rule. In this implementation, the weights of the network can be trained to minimize the loss function for a single refractive index distribution, $n(r)$ in Eq. 5.1. In our approach, the PINN gets the refractive index, $n(r)$, on a uniform grid as the input and finds the field on the same grid which minimizes the loss function for that refractive index. The output of the network is the 3D array of the scattered field envelope, and we use a finite difference scheme to calculate the derivative of the field with respect to the coordinates:

$$\frac{\partial U^s}{\partial x} = \frac{U^s((i+1)\Delta x, j\Delta y, k\Delta z) - U^s((i-1)\Delta x, j\Delta y, k\Delta z)}{2\Delta x} \quad (\text{C.1})$$

in which (i, j, k) are the pixel indices and Δx , Δy , Δz , are the pixel sizes along the x , y , and z axes. This way, we can calculate $\frac{\partial U^s}{\partial x}$ by convolving U^s with a kernel of $[-1/2, 0, 1/2]$ along the x axis. When computing electromagnetic fields, since the curl of the electric field gives the magnetic field and vice versa, a smart technique to improve accuracy is to use two staggered grids for discretizing fields, commonly referred to as Yee scheme [105]. In practice, this can be easily implemented through two shifted convolutional kernels for the two grids, $[-1/2, 1/2, 0]$ and $[0, -1/2, 1/2]$.

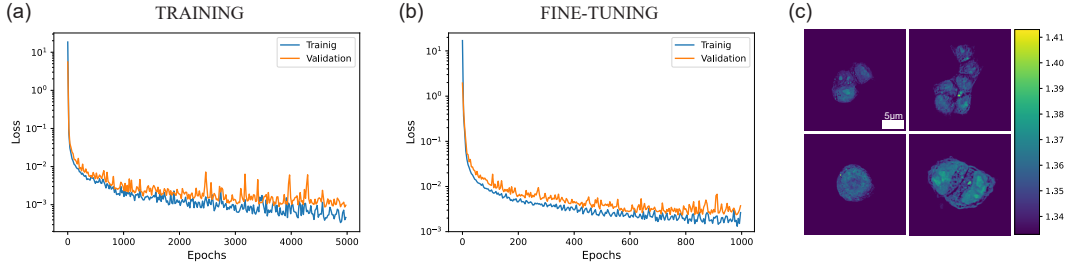


Figure C.1: Training and fine-tuning of MaxwellNet. (a) Training (blue) and validation (orange) loss of MaxwellNet for Digital cell phantoms dataset. (b) Fine-tuning the pretrained MaxwellNet for a dataset of HCT-116 cells for 1000 epochs. (c) Examples of the HCT-116 dataset.

In order to minimize the discretization error, one can use a smaller pixel size, Δx or higher order approximations. Here, we use the fourth-order finite difference scheme [118] in which convolutional kernels of $[0, +1/24, -9/8, +9/8, -1/24]$ and $[+1/24, -9/8, +9/8, -1/24, 0]$ are used for the calculation of the derivatives in Eq. 5.1.

C.2 Training and Fine-tuning of MaxwellNet

As mentioned in Section 5.3, we create a dataset of digital cell phantoms to train and validate MaxwellNet. The dataset for 2D MaxwellNet includes 3000 phantoms with elliptical shapes oriented in different directions. The size of these phantoms is in the range of $5 - 10 \mu\text{m}$, their refractive index varies in the range of $(1.38, 1.45)$, and the background refractive index is $n_0 = 1.33$. Two examples of these phantoms are shown in Fig. 5.2. We divide this dataset into 2700 phantoms for training and 300 phantoms for testing. We use batch training with a batch size of 10 for 5000 epochs. This training took 30.5 hours and after 5000 epochs, no significant decrease in the validation loss could be observed. The training and validation curves of the physical loss are presented in Fig. C.1(a). This figure shows that MaxwellNet performs very well for out-of-sample cases.

We discussed in Section 5.3 using MaxwellNet which was trained for cell phantoms to predict the scattered field for real cells. A dataset of HCT-116 cancer cells is used for this purpose. The 3D refractive index of these cells is reconstructed using Rytov approximation with projections achieved with an experimental setup utilizing spatial light modulator as described in [28]. Then, a 2D slice of the refractive index is chosen in the plane of best focus. A total number of 8 cells are used and we rotated and shifted these cells to create a dataset of 136 inhomogeneous cells whose refractive index range is $(1.33, 1.41)$. We use 122 of these images for training and 14 for validation. Some examples of HCT-116 refractive index dataset are shown in Fig. C.1(c). We freeze the encoder of MaxwellNet and fine-tune its decoder for this new dataset. The training and validation losses are presented in Fig. C.1(b).

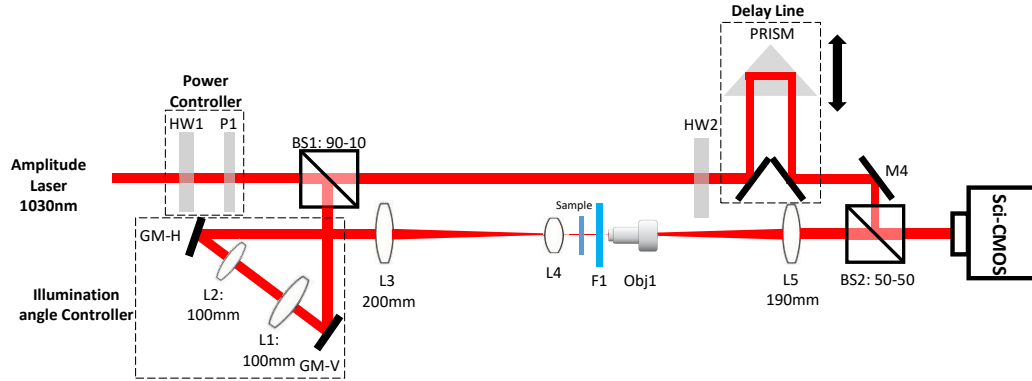


Figure C.2: Experimental setup for multiple illumination angle off-axis holography. HW: Half-wave plate, P: Polarizer, BS: Beam splitter, L: Lens, Obj: microscope objective, M: Mirror.

For 3D MaxwellNet, a dataset of 200 phantoms is created. These 3D phantoms have a spherical shape with some details inside them and the range of their diameter is $1.8 - 2.4 \mu\text{m}$. We randomly choose 180 phantoms for training and 20 phantoms for testing. We train 3D MaxwellNet with the training dataset with batch size of 10. The example of Fig. 5.3 and Fig. 5.5 is one of the phantoms in the testing dataset.

C.3 Experimental Setup for ODT

For ODT, we require complex scattered fields from multiple illumination angles. The off-axis holographic setup to accomplish that is shown in Fig. C.2. It relies on a ytterbium-doped fiber laser at $\lambda = 1.030 \mu\text{m}$ whose power is controlled with a half-wave plate and a polarizing beam splitter. The optical beam is divided into the signal and reference arms using a beam splitter (BS1). In the signal arm, we use two galvo mirrors, GM-V and GM-H to control the illumination angle in the vertical and horizontal directions. Using two 4F systems (L1-L4), we image these galvo mirrors on the sample plane, so the position of the beam remains fixed while changing the illumination angle. This way, we can illuminate the sample with a condensed plane wave. The sample is then imaged on the camera (Andor sCMOS Neo 5.5) using another 4F system consisting of a 60X water dipping objective (Obj1) and a tube lens L5. The signal and reference arms are then combined with another beam splitter, BS2 to create the off-axis hologram on the camera. A motorized delay line controls the optical path of the reference arm to match the optical path of the signal arm.

Bibliography

- [1] B. Kemper, A. Bauwens, A. Vollmer, *et al.*, “Label-free quantitative cell division monitoring of endothelial cells by digital holographic microscopy,” *Journal of Biomedical Optics*, vol. 15, no. 3, pp. 036 009–036 009, 2010.
- [2] P. Marquet, C. Depeursinge, and P. J. Magistretti, “Review of quantitative phase-digital holographic microscopy: promising novel imaging technique to resolve neuronal network activity and identify cellular biomarkers of psychiatric disorders,” *Neurophotonics*, vol. 1, no. 2, pp. 020 901–020 901, 2014.
- [3] K. Licha and C. Olbrich, “Optical imaging in drug discovery and diagnostic applications,” *Advanced drug delivery reviews*, vol. 57, no. 8, pp. 1087–1108, 2005.
- [4] B. Kemper, D. Carl, J. Schnekenburger, *et al.*, “Investigation of living pancreas tumor cells by digital holographic microscopy,” *Journal of biomedical optics*, vol. 11, no. 3, pp. 034 005–034 005, 2006.
- [5] B.-G. Wang, K. König, and K.-J. Halbhuber, “Two-photon microscopy of deep intravital tissues and its merits in clinical research,” *Journal of microscopy*, vol. 238, no. 1, pp. 1–20, 2010.
- [6] L. Song, E. Hennink, I. T. Young, and H. J. Tanke, “Photobleaching kinetics of fluorescein in quantitative fluorescence microscopy,” *Biophysical journal*, vol. 68, no. 6, pp. 2588–2600, 1995.
- [7] J. W. Lichtman and J.-A. Conchello, “Fluorescence microscopy,” *Nature methods*, vol. 2, no. 12, pp. 910–919, 2005.
- [8] F. Zernike, “Phase contrast, a new method for the microscopic observation of transparent objects,” *Physica*, vol. 9, no. 7, pp. 686–698, 1942.
- [9] D. Gabor, “A new microscopi principle,” *nature*, vol. 161, pp. 777–778, 1948.
- [10] A. Nwaneshiudu, C. Kuschal, F. H. Sakamoto, R. R. Anderson, K. Schwarzenberger, and R. C. Young, “Introduction to confocal microscopy,” *Journal of Investigative Dermatology*, vol. 132, no. 12, pp. 1–5, 2012.
- [11] P. A. Santi, “Light sheet fluorescence microscopy: a review,” *Journal of Histochemistry & Cytochemistry*, vol. 59, no. 2, pp. 129–138, 2011.

- [12] J. M. Schmitt, "Optical coherence tomography (oct): a review," *IEEE Journal of selected topics in quantum electronics*, vol. 5, no. 4, pp. 1205–1215, 1999.
- [13] E. Wolf, "Three-dimensional structure determination of semi-transparent objects from holographic data," *Optics communications*, vol. 1, no. 4, pp. 153–156, 1969.
- [14] F. Charrière, A. Marian, F. Montfort, *et al.*, "Cell refractive index tomography by digital holographic microscopy," *Optics letters*, vol. 31, no. 2, pp. 178–180, 2006.
- [15] W. Choi, C. Fang-Yen, K. Badizadegan, *et al.*, "Tomographic phase microscopy," *Nature methods*, vol. 4, no. 9, pp. 717–719, 2007.
- [16] D. Jin, R. Zhou, Z. Yaqoob, and P. T. So, "Tomographic phase microscopy: principles and applications in bioimaging," *JOSA B*, vol. 34, no. 5, B64–B77, 2017.
- [17] K. Iwata and R. Nagata, "Calculation of refractive index distribution from interferograms using the born and rytov's approximation," *Japanese Journal of Applied Physics*, vol. 14, no. S1, p. 379, 1975.
- [18] Y. Sung, W. Choi, C. Fang-Yen, K. Badizadegan, R. R. Dasari, and M. S. Feld, "Optical diffraction tomography for high resolution live cell imaging," *Optics express*, vol. 17, no. 1, pp. 266–277, 2009.
- [19] Y. Cotte, F. Toy, P. Jourdain, *et al.*, "Marker-free phase nanoscopy," *Nature Photonics*, vol. 7, no. 2, pp. 113–117, 2013.
- [20] S. Vertu, J. Flügge, J.-J. Delaunay, and O. Haerberlé, "Improved and isotropic resolution in tomographic diffractive microscopy combining sample and illumination rotation," *Central European Journal of Physics*, vol. 9, no. 4, pp. 969–974, 2011.
- [21] P. Hosseini, Y. Sung, Y. Choi, N. Lue, Z. Yaqoob, and P. So, "Scanning color optical tomography (scot)," *Optics express*, vol. 23, no. 15, pp. 19 752–19 762, 2015.
- [22] F. Merola, P. Memmolo, L. Miccio, *et al.*, "Tomographic flow cytometry by digital holography," *Light: Science & Applications*, vol. 6, no. 4, e16241–e16241, 2017.
- [23] M. M. Villone, P. Memmolo, F. Merola, *et al.*, "Full-angle tomographic phase microscopy of flowing quasi-spherical cells," *Lab on a Chip*, vol. 18, no. 1, pp. 126–131, 2018.
- [24] M. Azimi and A. Kak, "Distortion in diffraction tomography caused by multiple scattering," *IEEE Transactions on Medical Imaging*, vol. 2, no. 4, pp. 176–195, 1983.
- [25] A. Devaney, "Inverse-scattering theory within the rytov approximation," *Optics letters*, vol. 6, no. 8, pp. 374–376, 1981.
- [26] J. Lim, K. Lee, K. H. Jin, *et al.*, "Comparative study of iterative reconstruction algorithms for missing cone problems in optical diffraction tomography," *Optics express*, vol. 23, no. 13, pp. 16 933–16 948, 2015.
- [27] U. S. Kamilov, I. N. Papadopoulos, M. H. Shoreh, *et al.*, "Learning approach to optical tomography," *Optica*, vol. 2, no. 6, pp. 517–522, 2015.

- [28] J. Lim, A. B. Ayoub, E. E. Antoine, and D. Psaltis, "High-fidelity optical diffraction tomography of multiple scattering samples," *Light: Science & Applications*, vol. 8, no. 1, pp. 1–12, 2019.
- [29] J. Lim, A. B. Ayoub, and D. Psaltis, "Three-dimensional tomography of red blood cells using deep learning," *Advanced Photonics*, vol. 2, no. 2, p. 026 001, 2020.
- [30] R. W. Boyd, *Nonlinear optics*. Academic press, 2020.
- [31] e. P. Franken, A. E. Hill, C. e. Peters, and G. Weinreich, "Generation of optical harmonics," *Physical Review Letters*, vol. 7, no. 4, p. 118, 1961.
- [32] J. Mertz, "Nonlinear microscopy: new techniques and applications," *Current opinion in neurobiology*, vol. 14, no. 5, pp. 610–616, 2004.
- [33] M. Born and E. Wolf, *Principles of optics: electromagnetic theory of propagation, interference and diffraction of light*. Elsevier, 2013.
- [34] M. Slaney, A. C. Kak, and L. E. Larsen, "Limitations of imaging with first-order diffraction tomography," *IEEE transactions on microwave theory and techniques*, vol. 32, no. 8, pp. 860–874, 1984.
- [35] T.-a. Pham, E. Soubies, A. Ayoub, J. Lim, D. Psaltis, and M. Unser, "Three-dimensional optical diffraction tomography with lippmann-schwinger model," *IEEE Transactions on Computational Imaging*, vol. 6, pp. 727–738, 2020.
- [36] U. S. Kamilov, I. N. Papadopoulos, M. H. Shoreh, *et al.*, "Optical tomographic image reconstruction based on beam propagation and sparse regularization," *IEEE Transactions on Computational Imaging*, vol. 2, no. 1, pp. 59–70, 2016.
- [37] A. C. Kak and M. Slaney, *Principles of computerized tomographic imaging*. SIAM, 2001.
- [38] Y. Sung and R. R. Dasari, "Deterministic regularization of three-dimensional optical diffraction tomography," *JOSA A*, vol. 28, no. 8, pp. 1554–1561, 2011.
- [39] J. W. Goodman, *Introduction to Fourier optics*. Roberts and Company publishers, 2005.
- [40] A. Yariv and P. Yeh, *Optical waves in crystals*. Wiley New York, 1984, vol. 5.
- [41] S. N. Savenkov, "Jones and mueller matrices: structure, symmetry relations and information content," *Light Scattering Reviews 4: Single Light Scattering and Radiative Transfer*, pp. 71–119, 2009.
- [42] R. C. Miller, "Optical second harmonic generation in piezoelectric crystals," *Applied Physics Letters*, vol. 5, no. 1, pp. 17–19, 1964.
- [43] F. Zernike and J. E. Midwinter, *Applied nonlinear optics*. Courier Corporation, 2006.
- [44] S. Inoué, "Polarization microscopy," *Current protocols in cell biology*, vol. 13, no. 1, pp. 4–9, 2002.
- [45] P. Arun Gopinathan, G. Kokila, M. Jyothi, C. Ananjan, L. Pradeep, and S. Humaira Nazir, "Study of collagen birefringence in different grades of oral squamous cell carcinoma using picosirius red and polarized light microscopy," *Scientifica*, vol. 2015, 2015.

- [46] T. Wilson, R. Juškaitis, and P. Higdon, "The imaging of dielectric point scatterers in conventional and confocal polarisation microscopes," *Optics Communications*, vol. 141, no. 5-6, pp. 298–313, 1997.
- [47] J.-X. Cheng, L. D. Book, and X. S. Xie, "Polarization coherent anti-stokes raman scattering microscopy," *Optics letters*, vol. 26, no. 17, pp. 1341–1343, 2001.
- [48] G. Latour, I. Gusachenko, L. Kowalczyk, I. Lamarre, and M.-C. Schanne-Klein, "In vivo structural imaging of the cornea by polarization-resolved second harmonic microscopy," *Biomedical optics express*, vol. 3, no. 1, pp. 1–15, 2012.
- [49] T. Colomb, P. Dahlgren, D. Beghuin, E. Cucho, P. Marquet, and C. Depeursinge, "Polarization imaging by use of digital holography," *Applied optics*, vol. 41, no. 1, pp. 27–37, 2002.
- [50] T. Colomb, E. Cucho, F. Montfort, P. Marquet, and C. Depeursinge, "Jones vector imaging by use of digital holography: simulation and experimentation," *Optics Communications*, vol. 231, no. 1-6, pp. 137–147, 2004.
- [51] X. Liu, B.-Y. Wang, and C.-S. Guo, "One-step jones matrix polarization holography for extraction of spatially resolved jones matrix of polarization-sensitive materials," *Optics letters*, vol. 39, no. 21, pp. 6170–6173, 2014.
- [52] S. Aknoun, P. Bon, J. Savatier, B. Wattellier, and S. Monneret, "Quantitative retardance imaging of biological samples using quadriwave lateral shearing interferometry," *Optics express*, vol. 23, no. 12, pp. 16 383–16 406, 2015.
- [53] B. Ge, R. Zhou, Y. Takiguchi, Z. Yaqoob, and P. T. So, "Single-shot optical anisotropy imaging with quantitative polarization interference microscopy," *Laser & photonics reviews*, vol. 12, no. 8, p. 1 800 070, 2018.
- [54] Y. Jiao, M. E. Kandel, X. Liu, W. Lu, and G. Popescu, "Real-time jones phase microscopy for studying transparent and birefringent specimens," *Optics Express*, vol. 28, no. 23, pp. 34 190–34 200, 2020.
- [55] M. Shribak and R. Oldenbourg, "Techniques for fast and sensitive measurements of two-dimensional birefringence distributions," *Applied Optics*, vol. 42, no. 16, pp. 3009–3017, 2003.
- [56] M. I. Shribak and R. Oldenbourg, "Mapping polymer birefringence in three-dimensions using a polarizing microscope with oblique illumination," in *Biophotonics Micro-and Nano-Imaging*, International Society for Optics and Photonics, vol. 5462, 2004, pp. 57–67.
- [57] J. F. De Boer, T. E. Milner, M. J. Van Gemert, and J. S. Nelson, "Two-dimensional birefringence imaging in biological tissue by polarization-sensitive optical coherence tomography," *Optics letters*, vol. 22, no. 12, pp. 934–936, 1997.
- [58] J. F. De Boer, C. K. Hitzenberger, and Y. Yasuno, "Polarization sensitive optical coherence tomography—a review," *Biomedical optics express*, vol. 8, no. 3, pp. 1838–1873, 2017.

- [59] C. K. Hitzenberger, E. Götzinger, M. Sticker, M. Pircher, and A. F. Fercher, "Measurement and imaging of birefringence and optic axis orientation by phase resolved polarization sensitive optical coherence tomography," *Optics express*, vol. 9, no. 13, pp. 780–790, 2001.
- [60] B. S. DeMay, N. Noda, A. S. Gladfelter, and R. Oldenbourg, "Rapid and quantitative imaging of excitation polarized fluorescence reveals ordered septin dynamics in live yeast," *Biophysical journal*, vol. 101, no. 4, pp. 985–994, 2011.
- [61] S. Abrahamsson, M. McQuilken, S. B. Mehta, *et al.*, "Multifocus polarization microscope (mf-polscope) for 3d polarization imaging of up to 25 focal planes simultaneously," *Optics express*, vol. 23, no. 6, pp. 7734–7754, 2015.
- [62] N. Ortega-Quijano and J. L. Arce-Diego, "Generalized jones matrices for anisotropic media," *Optics Express*, vol. 21, no. 6, pp. 6895–6900, 2013.
- [63] S. Shin, K. Lee, Z. Yaqoob, P. T. So, and Y. Park, "Reference-free polarization-sensitive quantitative phase imaging using single-point optical phase conjugation," *Optics express*, vol. 26, no. 21, pp. 26 858–26 865, 2018.
- [64] J. M. Bioucas-Dias and G. Valadao, "Phase unwrapping via graph cuts," *IEEE Transactions on Image processing*, vol. 16, no. 3, pp. 698–709, 2007.
- [65] M. R. Foreman and P. Török, "Computational methods in vectorial imaging," *Journal of Modern Optics*, vol. 58, no. 5-6, pp. 339–364, 2011.
- [66] L. I. Rudin, S. Osher, and E. Fatemi, "Nonlinear total variation based noise removal algorithms," *Physica D: nonlinear phenomena*, vol. 60, no. 1-4, pp. 259–268, 1992.
- [67] A. Douplik, G. Saiko, I. Schelkanova, and V. Tuchin, "The response of tissue to laser light," in *Lasers for Medical Applications*, Elsevier, 2013, pp. 47–109.
- [68] F. De Chaumont, S. Dallongeville, N. Chenouard, *et al.*, "Icy: an open bioimage informatics platform for extended reproducible research," *Nature methods*, vol. 9, no. 7, pp. 690–696, 2012.
- [69] S. Shin, J. Eun, S. S. Lee, *et al.*, "Tomographic measurement of dielectric tensors at optical frequency," *Nature Materials*, vol. 21, no. 3, pp. 317–324, 2022.
- [70] H. Hugonnet, S. Shin, and Y. Park, "Regularization of dielectric tensor tomography," *Optics Express*, vol. 31, no. 3, pp. 3774–3783, 2023.
- [71] C. Joo, S. Song, J. Kim, *et al.*, "Polarization-sensitive intensity diffraction tomography," 2022.
- [72] I. Freund and M. Deutsch, "Second-harmonic microscopy of biological tissue," *Optics letters*, vol. 11, no. 2, pp. 94–96, 1986.
- [73] P. Stoller, P. M. Celliers, K. M. Reiser, and A. M. Rubenchik, "Quantitative second-harmonic generation microscopy in collagen," *Applied optics*, vol. 42, no. 25, pp. 5209–5219, 2003.

- [74] Y. Pu, M. Centurion, and D. Psaltis, "Harmonic holography: a new holographic principle," *Applied Optics*, vol. 47, no. 4, A103–A110, 2008.
- [75] C.-L. Hsieh, R. Grange, Y. Pu, and D. Psaltis, "Three-dimensional harmonic holographic microscopy using nanoparticles as probes for cell imaging," *Optics express*, vol. 17, no. 4, pp. 2880–2891, 2009.
- [76] C.-L. Hsieh, Y. Pu, R. Grange, and D. Psaltis, "Digital phase conjugation of second harmonic radiation emitted by nanoparticles in turbid media," *Optics express*, vol. 18, no. 12, pp. 12 283–12 290, 2010.
- [77] O. Masihzadeh, P. Schlup, and R. A. Bartels, "Label-free second harmonic generation holographic microscopy of biological specimens," *Optics express*, vol. 18, no. 10, pp. 9840–9851, 2010.
- [78] C. Hu, J. J. Field, V. Kelkar, *et al.*, "Harmonic optical tomography of nonlinear structures," *Nature Photonics*, vol. 14, no. 9, pp. 564–569, 2020.
- [79] W. Yu, X. Li, B. Wang, J. Qu, and L. Liu, "Optical diffraction tomography of second-order nonlinear structures in weak scattering media: theoretical analysis and experimental consideration," *Optics Express*, vol. 30, no. 25, pp. 45 724–45 737, 2022.
- [80] A. Saba, J. Lim, A. B. Ayoub, E. E. Antoine, and D. Psaltis, "Polarization-sensitive optical diffraction tomography," *Optica*, vol. 8, no. 3, pp. 402–408, 2021.
- [81] S. V. Plotnikov, A. C. Millard, P. J. Campagnola, and W. A. Mohler, "Characterization of the myosin-based source for second-harmonic generation from muscle sarcomeres," *Biophysical journal*, vol. 90, no. 2, pp. 693–703, 2006.
- [82] V. Nucciotti, C. Stringari, L. Sacconi, *et al.*, "Probing myosin structural conformation in vivo by second-harmonic generation microscopy," *Proceedings of the National Academy of Sciences*, vol. 107, no. 17, pp. 7763–7768, 2010.
- [83] M. Dubreuil, F. Tissier, L. Le Roy, *et al.*, "Polarization-resolved second harmonic microscopy of skeletal muscle in sepsis," *Biomedical optics express*, vol. 9, no. 12, pp. 6350–6358, 2018.
- [84] M. Rivard, C.-A. Couture, A. K. Miri, *et al.*, "Imaging the bipolarity of myosin filaments with interferometric second harmonic generation microscopy," *Biomedical Optics Express*, vol. 4, no. 10, pp. 2078–2086, 2013.
- [85] A. Saba, C. Gigli, A. B. Ayoub, and D. Psaltis, "Physics-informed neural networks for diffraction tomography," *Advanced Photonics*, vol. 4, no. 6, p. 066 001, 2022.
- [86] S. Chowdhury, M. Chen, R. Eckert, *et al.*, "High-resolution 3d refractive index microscopy of multiple-scattering samples from intensity images," *Optica*, vol. 6, no. 9, pp. 1211–1219, 2019.
- [87] G. E. Karniadakis, I. G. Kevrekidis, L. Lu, P. Perdikaris, S. Wang, and L. Yang, "Physics-informed machine learning," *Nature Reviews Physics*, vol. 3, no. 6, pp. 422–440, 2021.
- [88] S. Cai, Z. Mao, Z. Wang, M. Yin, and G. E. Karniadakis, "Physics-informed neural networks (pinns) for fluid mechanics: a review," *Acta Mechanica Sinica*, pp. 1–12, 2022.

- [89] Y. Rivenson, Z. Göröcs, H. Günaydin, Y. Zhang, H. Wang, and A. Ozcan, “Deep learning microscopy,” *Optica*, vol. 4, no. 11, pp. 1437–1443, 2017.
- [90] N. Borhani, E. Kakkava, C. Moser, and D. Psaltis, “Learning to see through multimode fibers,” *Optica*, vol. 5, no. 8, pp. 960–966, 2018.
- [91] B. Rahmani, D. Loterie, G. Konstantinou, D. Psaltis, and C. Moser, “Multimode optical fiber transmission with a deep learning network,” *Light: science & applications*, vol. 7, no. 1, pp. 1–11, 2018.
- [92] Y. Rivenson, Y. Zhang, H. Günaydin, D. Teng, and A. Ozcan, “Phase recovery and holographic image reconstruction using deep learning in neural networks,” *Light: Science & Applications*, vol. 7, no. 2, pp. 17 141–17 141, 2018.
- [93] Z. Ren, Z. Xu, and E. Y. Lam, “End-to-end deep learning framework for digital holographic reconstruction,” *Advanced Photonics*, vol. 1, no. 1, p. 016 004, 2019.
- [94] D. Pirone, D. Sirico, L. Miccio, *et al.*, “Speeding up reconstruction of 3d tomograms in holographic flow cytometry via deep learning,” *Lab on a Chip*, vol. 22, no. 4, pp. 793–804, 2022.
- [95] I. E. Lagaris, A. Likas, and D. I. Fotiadis, “Artificial neural networks for solving ordinary and partial differential equations,” *IEEE transactions on neural networks*, vol. 9, no. 5, pp. 987–1000, 1998.
- [96] L. Lu, X. Meng, Z. Mao, and G. E. Karniadakis, “DeepXDE: A deep learning library for solving differential equations,” *SIAM Review*, vol. 63, no. 1, pp. 208–228, 2021, ISSN: 00361445. DOI: 10.1137/19M1274067. arXiv: 1907.04502.
- [97] M. Raissi, P. Perdikaris, and G. E. Karniadakis, “Physics-informed neural networks: a deep learning framework for solving forward and inverse problems involving nonlinear partial differential equations,” *Journal of Computational physics*, vol. 378, pp. 686–707, 2019.
- [98] S. M. H. Hashemi and D. Psaltis, “Deep-learning pdes with unlabeled data and hard-wiring physics laws,” *arXiv preprint arXiv:1904.06578*, 2019.
- [99] Z. Mao, A. D. Jagtap, and G. E. Karniadakis, “Physics-informed neural networks for high-speed flows,” *Computer Methods in Applied Mechanics and Engineering*, vol. 360, p. 112 789, 2020.
- [100] X. Jin, S. Cai, H. Li, and G. E. Karniadakis, “Nsfnets (navier-stokes flow nets): physics-informed neural networks for the incompressible navier-stokes equations,” *Journal of Computational Physics*, vol. 426, p. 109 951, 2021.
- [101] Y. Chen, L. Lu, G. E. Karniadakis, and L. Dal Negro, “Physics-informed neural networks for inverse problems in nano-optics and metamaterials,” *Optics express*, vol. 28, no. 8, pp. 11 618–11 633, 2020.

- [102] Y. Chen and L. Dal Negro, "Physics-informed neural networks for imaging and parameter retrieval of photonic nanostructures from near-field data," *APL Photonics*, vol. 7, no. 1, p. 010 802, 2022. DOI: 10.1063/5.0072969. [Online]. Available: <https://doi.org/10.1063/5.0072969>.
- [103] J. Lim and D. Psaltis, "Maxwellnet: physics-driven deep neural network training based on maxwell's equations," *APL Photonics*, vol. 7, no. 1, p. 011 301, 2022.
- [104] O. Ronneberger, P. Fischer, and T. Brox, "U-net: convolutional networks for biomedical image segmentation," in *International Conference on Medical image computing and computer-assisted intervention*, Springer, 2015, pp. 234–241.
- [105] K. Yee, "Numerical solution of initial boundary value problems involving maxwell's equations in isotropic media," *IEEE Transactions on antennas and propagation*, vol. 14, no. 3, pp. 302–307, 1966.
- [106] W. C. Chew and W. H. Weedon, "A 3d perfectly matched medium from modified maxwell's equations with stretched coordinates," *Microwave and optical technology letters*, vol. 7, no. 13, pp. 599–604, 1994.
- [107] A. Ishimaru, *Wave propagation and scattering in random media*. Academic press New York, 1978, vol. 2.
- [108] C. Tan, F. Sun, T. Kong, W. Zhang, C. Yang, and C. Liu, "A survey on deep transfer learning," in *International conference on artificial neural networks*, Springer, 2018, pp. 270–279.
- [109] C. Gigli, A. Saba, A. B. Ayoub, and D. Psaltis, "Predicting nonlinear optical scattering with physics-driven neural networks," *APL Photonics*, 2022.
- [110] A. Ciattoni, P. Di Porto, B. Crosignani, and A. Yariv, "Vectorial nonparaxial propagation equation in the presence of a tensorial refractive-index perturbation," *JOSA B*, vol. 17, no. 5, pp. 809–819, 2000.
- [111] Z. Tong and O. Korotkova, "Theory of weak scattering of stochastic electromagnetic fields from deterministic and random media," *Physical Review A*, vol. 82, no. 3, p. 033 836, 2010.
- [112] R. Gilmore, "Baker-campbell-hausdorff formulas," *Journal of Mathematical Physics*, vol. 15, no. 12, pp. 2090–2092, 1974.
- [113] M. Feit and J. Fleck, "Beam nonparaxiality, filament formation, and beam breakup in the self-focusing of optical beams," *JOSA B*, vol. 5, no. 3, pp. 633–640, 1988.
- [114] C. D. Meyer, *Matrix analysis and applied linear algebra*. Siam, 2000, vol. 71, pp. 525–526.
- [115] Y. Bao and T. K. Gaylord, "Clarification and unification of the obliquity factor in diffraction and scattering theories: discussion," *JOSA A*, vol. 34, no. 10, pp. 1738–1745, 2017.
- [116] Y. Fainman and J. Shamir, "Polarization of nonplanar wave fronts," *Applied optics*, vol. 23, no. 18, pp. 3188–3195, 1984.

-
- [117] A. Beck and M. Teboulle, “Fast gradient-based algorithms for constrained total variation image denoising and deblurring problems,” *IEEE transactions on image processing*, vol. 18, no. 11, pp. 2419–2434, 2009.
- [118] A. Fathy, C. Wang, J. Wilson, and S. Yang, “A fourth order difference scheme for the Maxwell equations on yee grid,” *Journal of Hyperbolic Differential Equations*, vol. 5, no. 3, pp. 613–642, 2008, ISSN: 02198916. DOI: 10.1142/S0219891608001623.

Amirhossein Saba

Birthday: 15.06.1995 (27 years-old)

Email: amirhosseinsabas@gmail.com

Phone: (+41) 78 252 61 69

Address: EPFL, STI, IMT, LO, BM4117,
Station 17, CH1015, Lausanne, Switzerland

 [Google Scholar](#)  [LinkedIn](#)  [Webpage](#)

KEY COMPETENCIES

- Expert in **optical imaging and microscopy**; computational and optimization techniques for optical imaging; machine learning of physical simulation; theoretical, numerical, and experimental knowledge in optics.
- Doctoral researcher in Laboratory of Optics, *EPFL*, working on **3D optical imaging**.
- Several projects on nonlinear optical imaging, polarization-sensitive holography, machine learning, and computational imaging.

EDUCATION

PhD in Photonics, École Polytechnique Fédérale de Lausanne (EPFL), Lausanne, Switzerland 2018-Now
Thesis title: Optical diffraction tomography in complex media, Supervisor: Prof. Demetri Psaltis

BSc in Electrical Engineering, Sharif University of Technology, Tehran (GPA: 3.86/4) 2013-2018
Thesis title: Analysis of geometrical dispersion in nonlinear metasurfaces, Supervisor: Prof. Mehrany

Minor in Physics, Sharif University of Technology, Tehran 2014-2018

PROFESSIONAL EXPERIENCES

Doctoral Research Assistant, Laboratory of Optics, EPFL, Lausanne, Switzerland Sep 2018-Now
Research projects on computational and deep learning techniques for optical imaging

Undergrad Research Assistant, Integrated Photonics Lab, SUT, Tehran Feb 2017-Jun 2018
Research projects on analog optical computing, and nonlinear metasurfaces

Research Intern, Optical Communication group, National Telecommunication Research center Jun 2017-Sep 2017

SKILLS

Optics:

Optical system design and analysis
Building **experimental** optical setups
Optical imaging, holography, and microscopy
Optimization of optical systems (Zemax, ray tracing)
Optical **simulation** (COMSOL, Beam Propagation, Lumerical, FDTD, RCWA)

Machine Learning and Computer Vision:

ML Packages: TensorFlow, Pytorch, Keras, Scikit-learn
Computer Vision Packages: OpenCV, Scikit-Image, PIL

Computer Software:

Programming: Python, MatLab, C++
Optics and Physics: COMSOL, Zemax, Lumerical
Windows Software: Microsoft Office, Solidworks, LaTeX

SELECTED PROJECTS

Physics-informed deep learning for optical diffraction tomography 2020-2022

Prediction of optical scattering with a neural network (4 orders of magnitude faster than FEM) by minimizing Maxwell's equations as a physics-informed loss and use this network as a forward model for iterative 3D reconstruction in optical diffraction tomography (ODT).

☑ using TensorFlow 2.6.0, Python 3.9, COMSOL, and Beam Propagation Method (BPM).

Nonlinear optical diffraction tomography 2020-Now

In this project, biological samples which contain second-order susceptibility are illuminated with a high-power femtosecond beam, and using direct and iterative 3D reconstruction methods, we reconstruct the 3D distribution of the second-order susceptibility.

☑ using COMSOL for nonlinear FEM simulation, MatLab for coding, Split-Bregman compressed sensing reconstruction.

Modal domain optical tomography 2020-2021

In this project, I generalized ODT for non-free-space propagation where we illuminate the sample with the modes of the fiber, measure the coupling between different modes and reconstruct the 3D refractive index of the perturbation in the modal domain.

☑ using MatLab for coding, modal domain holography setup for Transmission Matrix measurements.

Deep learning for optical phase retrieval from depolarization of light Spring 2019

Optical phase retrieval from intensity of the cross-polarized light using an U-Net deep neural network.

☑ using TensorFlow and Keras to implement DNN, MatLab to generate synthetic dataset with BPM.

Polarization-sensitive 3D optical imaging 2019-2021

Generalization of diffraction tomography for polarization-sensitive cases for 3D reconstruction of refractive index tensor. All the experimental, theoretical, and numerical aspects of the project were done by me under the supervision of *Prof. D. Psaltis*.

☑ using MatLab for coding, vectorial BPM for optical simulation, compressed sensing for iterative 3D reconstruction.

Two-dimensional edge detection with guided mode resonant metasurfaces 2017-2018

I exploited guided mode resonance in 2D gratings and designed them for achieving transmission resonances and using them for analog computing as Laplace operator and optical edge detection. ☑ using RCWA and COMSOL for optical simulation, and MatLab for coding.

HONORS AND AWARDS

- Journal Cover for paper. Advanced Photonics December 2022
- Direct PhD admission from EPFL right after BSc. April 2018
- **Silver Medal** in National Physics Olympiad. Sep 2012
- Ranked 32th among almost 270,000 participants in Nationwide University Entrance Exam for B.Sc. degree ("Konkooor"). July 2013
- Member of National Elite Foundation. Iran National Elites Foundation (INEF) is an organization and composed of members with significant scientific and executive background. 2013-2018

TEACHING, EXECUTIVE, AND VOLUNTEER EXPERIENCES

- **Principal Teaching Assistant**, Deep Learning for Optical Imaging, EPFL, for two years. Jan 2021-June 2022
 - Teaching Assistant, COMSOL Tutorial for Electromagnetics, Sharif University of Technology. Fall 2017
 - Student Member, Institute of Electrical and Electronics Engineering (IEEE) 2013-2016
 - **Technical Committee Organizer**, Sharif Event on Water and Energy Nexus 2015-2016
 - Executive Member, Sharif Startup Trigger 4 Fall 2015
-

SELECTED PUBLICATIONS ([Google Scholar Link](#))

- **Amirhossein Saba**, Carlo Gigli, Ahmed B. Ayoub, and Demetri Psaltis. "Physics-informed neural networks for diffraction tomography." *Advanced Photonics*. 4.6 (2022): 066001. [\[Link\]](#)
 - Ulas N. Dinc, **Amirhossein Saba**, Jorge Madrid-Wolff, Carlo Gigli, Antoine Boniface, C. Moser, and Demetri Psaltis. "From 3D to 2D and back again." *Nanophotonics*. (2023). [\[Link\]](#)
 - Carlo Gigli, **Amirhossein Saba**, Ahmed Bassam Ayoub, and Demetri Psaltis. "Predicting nonlinear optical scattering with physics-driven neural networks." *APL Photonics* (2022). [\[Link\]](#)
 - Ahmed B. Ayoub, **Amirhossein Saba**, Carlo Gigli, and Demetri Psaltis. "Optical Diffraction Tomography based on 3D Physics-Inspired Neural Network (PINN)." arXiv preprint arXiv:2206.05236 (2022). [\[Link\]](#)
 - **Amirhossein Saba**, Joowon Lim, Ahmed B. Ayoub, Elizabeth E. Antoine, and Demetri Psaltis. "Polarization-sensitive optical diffraction tomography." *Optica* 8, no. 3 (2021): 402-408. [\[Link\]](#)
 - **Amirhossein Saba**, Joowon Lim, Ahmed B. Ayoub, Elizabeth E. Antoine, and Demetri Psaltis, Tomographic Diffraction Microscopy of Birefringence, *Conference presentation*, Digital Holography and Three-Dimensional Imaging. OSA, (2021). [\[Link\]](#)
 - **Amirhossein Saba**, Mohammad Memarian, and Khashayar Mehrany. "Wideband and Narrowband Circuit Models for Fano-Shape Guided-Mode Resonance." *IEEE Journal of Quantum Electronics* 55, no. 3 (2019): 1-8. [\[Link\]](#)
 - Mohammad Reza Tavakol, **Amirhossein Saba**, Kamalodin Arik, and Amin Khavasi. "Tunable leaky-wave radiation by graphene-covered corrugated surfaces." *Applied optics* 57, no. 30 (2018): 8971-8977. [\[Link\]](#)
 - **Amirhossein Saba**, Mohammad Reza Tavakol, Parisa Karimi-Khoozani, and Amin Khavasi. "Two-dimensional edge detection by guided mode resonant metasurface." *IEEE Photonics Technology Letters* 30, no. 9 (2018): 853-856. [\[Link\]](#)
 - Mohammad Reza Tavakol, **Amirhossein Saba**, Amir Jafargholi, and Amin Khavasi. "Terahertz spectrum splitting by a graphene-covered array of rectangular grooves." *Optics letters* 42, no. 23 (2017): 4808-4811. [\[Link\]](#)
-

LANGUAGES

English (Fluent), French (Intermediate: B1 level), Farsi (Native)

HOBBIES

Astronomy, Astrophotography, Hiking

REFERENCE

Prof. Demetri Psaltis, Professor, EPFL, demetri.psaltis@epfl.ch

Prof. Amin Khavasi, Professor, Sharif University of Technology, khavasi@sharif.edu
